Lithographic fabrication, electrical characterization and proof-of-concept demonstration of sensor circuits comprising organic electrochemical transistors for in vitro and in vivo diagnostics

Marcel Braendlein

Nº d'ordre NNT : 2017LYSEM007

THESE de DOCTORAT DE L'UNIVERSITE DE LYON

opérée au sein de

l'Ecole des Mines de Saint-Etienne

Ecole Doctorale Nº 488
Sciences, Ingénierie, Santé

Spécialité de doctorat : Microélectronique
Discipline : Bioélectronique Organique

Soutenue publiquement le 24/03/2017, par :

Marcel BRAENDLEIN

Lithographic Fabrication, Electrical Characterization and Proof-of-Concept Demonstration of Sensor Circuits Comprising Organic Electrochemical Transistors for In Vitro and In Vivo Diagnostics

---

Devant le jury composé de :

Président:	Alberto SALLEO	Professor, Stanford University, Stanford
Rapporteurs:	Robert FORCHHEIMER	Professor, Linköping Universitet, Linköping
	Jose A. GARRIDO	Professor, Institut Català de Nanociència i Nanotecnologia, Barcelona
Examinateurs:	Róisín M. OWENS	Professor, Ecole des Mines de Saint-Etienne, Gardanne
	Jean-Michel BADIER	Technical Director, Aix-Marseille Université, Marseille
Directeur de thèse:	George G. MALLIARAS	Professor, Ecole des Mines de Saint-Etienne, Gardanne

Spécialités doctorales	Responsables :	Spécialités doctorales	Responsables
SCIENCES ET GENIE DES MATERIAUX	K. Wolski Directeur de recherche	MATHEMATIQUES APPLIQUEES	O. Roustant, Maître-assistant
MECANIQUE ET INGENIERIE	S. Drapier, professeur	INFORMATIQUE	O. Boissier, Professeur
GENIE DES PROCEDES	F. Gruy, Maître de recherche	SCIENCES DES IMAGES ET DES FORMES	JC. Pinoli, Professeur
SCIENCES DE LA TERRE	B. Guy, Directeur de recherche	GENIE INDUSTRIEL	X. Delorme, Maître assistant
SCIENCES ET GENIE DE L'ENVIRONNEMENT	D. Graillot, Directeur de recherche	MICROELECTRONIQUE	Ph. Lalevée, Professeur

EMSE : Enseignants-chercheurs et chercheurs autorisés à diriger des thèses de doctorat (titulaires d'un doctorat d'État ou d'une HDR)

ABSI	Nabil	CR	Génie industriel	CMP
AUGUSTO	Vincent	CR	Image, Vision, Signal	CIS
AVRIL	Stéphane	PR2	Mécanique et ingénierie	CIS
BADEL	Pierre	MA(MDC)	Mécanique et ingénierie	CIS
BALBO	Flavien	PR2	Informatique	FAYOL
BASSEREAU	Jean-François	PR	Sciences et génie des matériaux	SMS
BATTON-HUBERT	Mireille	PR2	Sciences et génie de l'environnement	FAYOL
BEIGBEDER	Michel	MA(MDC)	Informatique	FAYOL
BLAYAC	Sylvain	MA(MDC)	Microélectronique	CMP
BOISSIER	Olivier	PR1	Informatique	FAYOL
BONNEFOY	Olivier	MA(MDC)	Génie des Procédés	SPIN
BORBELY	Andras	MR(DR2)	Sciences et génie des matériaux	SMS
BOUCHER	Xavier	PR2	Génie Industriel	FAYOL
BRODHAG	Christian	DR	Sciences et génie de l'environnement	FAYOL
BRUCHON	Julien	MA(MDC)	Mécanique et ingénierie	SMS
CAMEIRAO	Ana	MA(MDC)	Génie des Procédés	SPIN
CHRISTIEN	Frédéric	PR	Science et génie des matériaux	SMS
DAUZERE-PERES	Stéphane	PR1	Génie Industriel	CMP
DEBAYLE	Johan	CR	Sciences des Images et des Formes	SPIN
DEGEORGE	Jean-Michel	MA(MDC)	Génie industriel	Fayol
DELAFOSSE	David	PR0	Sciences et génie des matériaux	SMS
DELORME	Xavier	MA(MDC)	Génie industriel	FAYOL
DESRAYAUD	Christophe	PR1	Mécanique et ingénierie	SMS
DJENIZIAN	Thierry	PR	Science et génie des matériaux	CMP
DOUCE	Sandrine	PR2	Sciences de gestion	FAYOL
DRAPIER	Sylvain	PR1	Mécanique et ingénierie	SMS
FAUCHEU	Jenny	MA(MDC)	Sciences et génie des matériaux	SMS
FAVERGEON	Loïc	CR	Génie des Procédés	SPIN
FEILLET	Dominique	PR1	Génie Industriel	CMP
FOREST	Valérie	MA(MDC)	Génie des Procédés	CIS
FOURNIER	Jacques	Ingénieur chercheur CEA	Microélectronique	CMP
FRACZKIEWICZ	Anna	DR	Sciences et génie des matériaux	SMS
GARCIA	Daniel	MR(DR2)	Sciences de la Terre	SPIN
GAVET	Yann	MA(MDC)	Sciences des Images et des Formes	SPIN
GERINGER	Jean	MA(MDC)	Sciences et génie des matériaux	CIS
GOEURIOT	Dominique	DR	Sciences et génie des matériaux	SMS
GONDRAN	Natacha	MA(MDC)	Sciences et génie de l'environnement	FAYOL
GRAILLOT	Didier	DR	Sciences et génie de l'environnement	SPIN
GROSSEAU	Philippe	DR	Génie des Procédés	SPIN
GRUY	Frédéric	PR1	Génie des Procédés	SPIN
GUY	Bernard	DR	Sciences de la Terre	SPIN
HAN	Woo-Suck	MR	Mécanique et ingénierie	SMS
HERRI	Jean Michel	PR1	Génie des Procédés	SPIN
KERMOUCHE	Guillaume	PR2	Mécanique et Ingénierie	SMS
KLOCKER	Helmut	DR	Sciences et génie des matériaux	SMS
LAFOREST	Valérie	MR(DR2)	Sciences et génie de l'environnement	FAYOL
LERICHE	Rodolphe	CR	Mécanique et ingénierie	FAYOL
MALLIARAS	Georges	PR1	Microélectronique	CMP
MOLIMARD	Jérôme	PR2	Mécanique et ingénierie	CIS
MOUTTE	Jacques	CR	Génie des Procédés	SPIN
NIKOLOVSKI	Jean-Pierre	Ingénieur de recherche	Mécanique et ingénierie	CMP
NORTIER	Patrice	PR1	Génie des Procédés	SPIN
O CONNOR	Rodney Philip	MA(MDC)	Microélectronique	CMP
OWENS	Rosin	MA(MDC)	Microélectronique	CMP
PERES	Véronique	MR	Génie des Procédés	SPIN
PICARD	Gauthier	MA(MDC)	Informatique	FAYOL
PIJOLAT	Christophe	PR0	Génie des Procédés	SPIN
PINOLI	Jean Charles	PR0	Sciences des Images et des Formes	SPIN
POURCHEZ	Jérémy	MR	Génie des Procédés	CIS
ROBISSON	Bruno	Ingénieur de recherche	Microélectronique	CMP
ROUSSY	Agnès	MA(MDC)	Microélectronique	CMP
ROUSTANT	Olivier	MA(MDC)	Mathématiques appliquées	FAYOL
SANAUR	Sébastien	MA(MDC)	Microélectronique	CMP
STOLARZ	Jacques	CR	Sciences et génie des matériaux	SMS
TRIA	Assia	Ingénieur de recherche	Microélectronique	CMP
VALDIVIESO	François	PR2	Sciences et génie des matériaux	SMS
VIRICELLE	Jean Paul	DR	Génie des Procédés	SPIN
WOLSKI	Krzystof	DR	Sciences et génie des matériaux	SMS
XIE	Xiaolan	PR1	Génie industriel	CIS
YUGMA	Gallian	CR	Génie industriel	CMP

Mise à jour : 12/12/2016

Contents

Chapter 1

State-of-the-Art in Bioelectronics

This chapter provides a general background in the field of bioelectronics. It shall serve as a basis for the remaining chapters that are comprised of more condensed journal articles. In a first part, the fundamentals of conducting polymers are explained and their impact on the field of bioelectronics is demonstrated. In particular, the conducting polymer poly(3,4-ethylenedioxythiophene) doped with polystyrene sulfonate (PEDOT:PSS) is introduced as it shall be the focus material of the present manuscript. In a second part, the organic electrochemical transistor is presented and the fundamental operation principle as well as the specific transistor characteristics for PEDOT:PSS are explained in detail. This is followed by a short introduction to two different lithographic fabrication approaches. The third part deals with the core topic of the present manuscript, i.e. sensor circuits based on the organic electrochemical transistor. In particular, the so called *voltage amplifier* circuit and the *Wheatstone bridge* circuit are introduced and their working principles are explained. The chapter finishes with a demonstration of a particular sensor circuit, sensitive to pressure changes in fluidic channels.

1.1 Conducting Polymers and Their Applications

Since the discovery and development of conducting polymers in 1977 by H. Shirakawa, A. Heeger and A. MacDiarmid [Chiang, 1977], for which they received the Nobel prize in chemistry in the year 2000, the field of organic electronics has been steadily growing with an expected market value of more than $ 75 billion by 2020, according to market research companies [Chavan, 2014; Singh, 2014]. In comparison, the global semiconductor industry reached a value of $ 335 billion in 2015, but the silicon based transistor technology has more than 20 years of advance [Tanenbaum, 1956; Riordan, 2004]. A

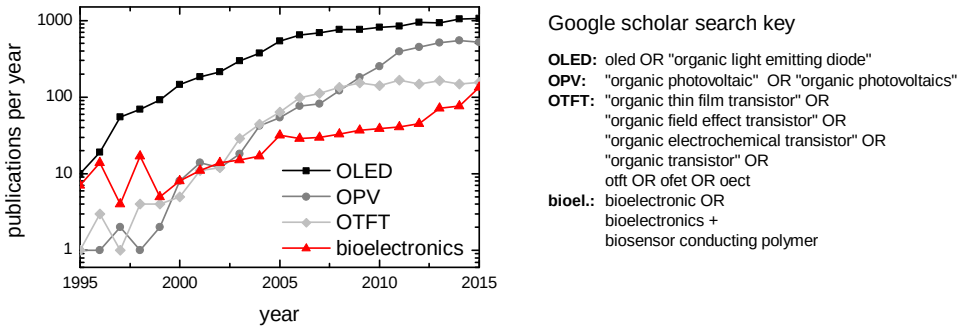

Figure 1.1: *Publications per year for selected topics in the field of organic electronics. The data has been acquired with Google Scholar's search engine using the search keys indicated on the right. Patents and citations have been excluded.*

literature search for the term "organic electronics" yields about 35 000 publications until now, of which more than 75 % have been published since 2010. This indicates an increased attention to the field that can be explained by steady improvement of the material stability, as well as maturation of key technologies already entering the market, such as flexible displays, organic solar cells and sensors [Jin Jang, 2002; Wiel, 2014; Mori, 2013]. In Figure 1.1 are shown the scientific publications per year over the last 20 years for these key technologies. It can be seen that the scientific output is steadily increasing with the most advanced field of organic light emitting diodes (OLED) reaching a value of over 1000 publications per year. Most interestingly, a saturation can be noted starting from the year 2005 for almost all fields expect for bioelectronics, where the field is still blooming and gaining increased momentum over the last few years.

Bioelectronics, dating back to the early days of Galvani's experiments on frog limbs [Galvani, 1791; Piccolino, 1997], is the study of biology by electronic means, through both sensing, in order to understand and interpret biological signals and pathways, as well as actuation, to actively control biological activity. Galvani demonstrated, that muscle tissue is responding to electrical signals, by connecting an electrode to the exposed crural nerves of a prepared frog leg and hanging this electrode out on his balcony on a stormy day. The atmospheric electric fields, generated by lightning, were sufficient to stimulate muscle contraction in the frog's leg. In a later experiment, that is considered to be the birth of electrophysiology, Galvani could demonstrate that such muscle contraction could even be achieved by directly connecting a section of the sciatic nerve of one frog leg to the healthy nerve of another frog leg, without the need of any external voltage source [Galvani, 1797]. Due to political reasons, however, this work on the so called *animal electricity* has not received the attention it deserved and it took about three decades until other scientists picked up Galvani's work [Matteucci, 1838].

Today we have advanced bioelectronic stimulation devices that rely on the work of these pioneers. One popular example would be the artificial cardiac pacemaker (see

Figure 1.2a), an implant that can be as small as $0.8\,cm^3$ [Ritter, 2015] (see Figure 1.2b), which allows for regulation of the heartbeat by stimulating the heart's muscle with defined electrical pulses. Another bioelectronic application, that can be found in every hospital, is the use of electrodes to record the electrical activity of the heart, electrocardiogram (ECG), or the brain, electroencephalogram (EEG). Here, the cutaneous contact of metal electrodes with the skin is sufficient to record a local field potential of the order of a few mV, generated by a large population of nerve or muscle cells. With this method, abnormalities in the corresponding organ can be detected to allow for an efficient diagnosis of the underlying condition. Recently, a trend towards monitoring of fitness parameters in sports activity has introduced such technologies to non-medical applications, and beat rate monitors can be purchased in any sports shop (see Figure 1.2d). But not only electrical activity is of interest in the field of bioelectronics, also metabolite levels [Wang, 2011], antibodies [Tan, 1989], DNA detection [Shin, 2013] can lead to improved health care monitoring and appropriate sensor devices have been developed over the past few decades.

However, most bioelectronic devices to date are based on rigid materials. The advantages of mechanical robustness, device stability and advanced signal processing with integrated circuit technology are often outweighed by the poor implementation of such devices within the biological environment. For example, deep brain stimulation electrodes currently used as FDA approved treatment for essential tremor in Parkinson's disease or for obsessive-compulsive disorder [Kringelbach, 2007] are comprised of metallic wires embedded in semiflexible polyurethane insulation (see Figure 1.2e), that upon implantation can cause injuries, inflammation and tissue scaring around the implantation site [Polikov, 2005; McConnell, 2009].

This is where a significant progress can be achieved by implementing conducting polymers into such devices. Due to the chemical tunability of their mechanical, optical and electrical properties [Patil, 1988; McCullough, 1993], such materials can have an immediate impact on the coupling of electronic devices to biological environments [Rivnay, 2014]. For instance, it has been found that platinum-iridium microelectrodes show superior performance for *in vivo* deep brain stimulation applications with a charge injection limit 15 times higher when coated with a popular conducting polymer, poly(3,4-ethylenedioxythiophene) or PEDOT [Venkatraman, 2011]. In the same year, the research group of Prof. David Martin has successfully demonstrated an *in vivo* polymerisation of PEDOT inside the brain (see Figure 1.2f) [Ouyang, 2011], eliminating the need for electrode implantation with possible glial scar encapsulation. The flexible nature of thin film processed conducting polymer devices have led to ultra-conformable sensor arrays for electrocorticography (ECoG) recordings, where the sensor array is placed on the surface of the brain [Khodagholy, 2013a]. The conducting polymer devices have outperformed standard iridium penetrating electrodes, demonstrating their enhanced signal recording capabilities with less invasive approaches. Most recently, a device capable of both chemical stimulation and electrical sensing at the same site has

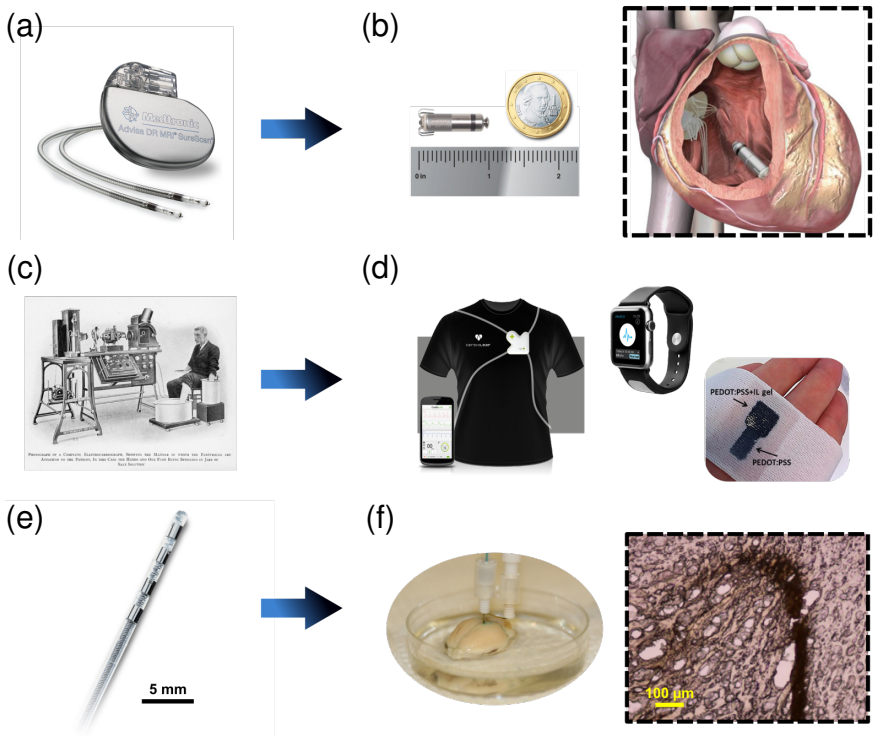

Figure 1.2: *Advances in bioelectronic devices. (a) Traditional artificial cardiac pacemaker from* Medtronic Inc. *The generator is placed under the skin in the chest region and the leads are implanted through the subclavian vein into the heart. (b) Micra Transcatheter Pacing system from* Medtronic Inc. *This miniaturized device is implanted directly into the right ventricle of the heart muscle without the need for leads, substantially lowering the risk for dislodgement, breakage, venous occlusion, and infection. Images taken from [Ritter, 2015]. (c) First commercially available electrocardiograph developed by Willem Einthoven and manufactured by the Cambridge Scientific Instrument Company of London in 1911. Image taken from [Zywietz, 2003]. (d) Various modern ECG recording systems. Cardioleaf FIT Shirt from Clearbridge VitalSigns (left), Kardia Band for the Apple Watch from AliveCor (middle) and a simple electrode for longterm ECG recordings comprised of a conducting polymer on textile (right, image taken from [Takamatsu, 2015]). (e) Commercially available deep brain stimulation electrode lead from* Medtronic Inc. *The four electrodes of about* 1.5 mm *size are implanted in the brain to allow for neural stimulation through electric pulses. (f) Conducting polymer electrode locally polymerized in a living rat cortex. In the optical micrograph, a defined cloud of PEDOT:PSS can be seen (black) and no inflammation or scaring reaction can be observed around the material. Such an in vivo deployment of highly conductive electrodes could be the next step towards more biocompatible deep brain stimulation devices. Images taken from [Ouyang, 2011].*

been demonstrated by Jonsson et al., again using a conducting polymer as essential part of the device [Jonsson, 2016]. Using a rat brain slice, they were able to locally

deliver an inhibitory neurotransmitter, γ-aminobutyric acid (GABA), via an organic electronic ionpump and observe the correlating decrease in induced epileptiform activity with an organic electrode. Such devices, when designed in an implantable form, could be very useful for feedback loop controlled local drug delivery, bypassing the blood-brain barrier that is the main limiting factor for drug efficiency in neurodegenerative diseases such as Alzheimer's, Parkinson's or Huntington's disease, to name only a few [Pardridge, 2005].

However, there are reasons, why such futuristic devices have not been successfully commercialized yet. One key issue with conducting polymers is the long-term stability of the material. For example, most *in vivo* animal experiments are done in an acute setup, meaning the device will be implanted and immediately measured to show the desired functionality. At most, long-term experiments are conducted over a period of several days or weeks [Ludwig, 2006]. But, in order to compete with existing inorganic technologies, implantable devices would have to last inside the body and function properly for several years [SaremAslani, 2011]. For example, Cui et al. showed that PEDOT coatings of platinum electrodes delaminate after only eight days [Cui, 2007]. Similar findings have been reported by Venkatraman et al. and an improved stability could be achieved for PEDOT coatings of platinum iridium electrodes [Venkatraman, 2011]. This means, that mechanical stability of the conducting polymer is substrate dependant and needs to be explored in more detail [Green, 2012]. Another limiting factor for long-term stability is biofilm formation at the sensor site, leading to an encapsulation of the device reducing its effectiveness towards the targeted tissue. For active devices, such as the electrolyte gated organic electrochemical transistor (see Section 1.2), electrochemical stability is a parameter that still needs to be improved, as the current output of the device is not stable and temperature drift, electrolyte evaporation or particular oxidizable compounds present in the electrolyte can lead to a significant drift of the signal. To this end, the scientific community has advertised organic electronics as a disposable, one-time use technology, focussing on short-term biosensing applications.

Nonetheless, a stable improvement of the device stability and capability can be observed over the years. For example, the addition of a chemical cross-linker, 3-glycidoxypropyltrimethoxysilane (GOPS), to a PEDOT solution leads to an increased mechanical stability for thin-film applications with less delamination problems occurring [Zhang, 2015]. Also, the implementation of such devices into more sophisticated differential sensor circuit layouts can reduce device failure and enhance signal quality [Svensson, 2008]. Many questions remain unsolved in the field of organic bioelectronics, which makes it very interesting to dig deeper into the matter and try to understand the complex interplay between the electronic devices and the biological environment.

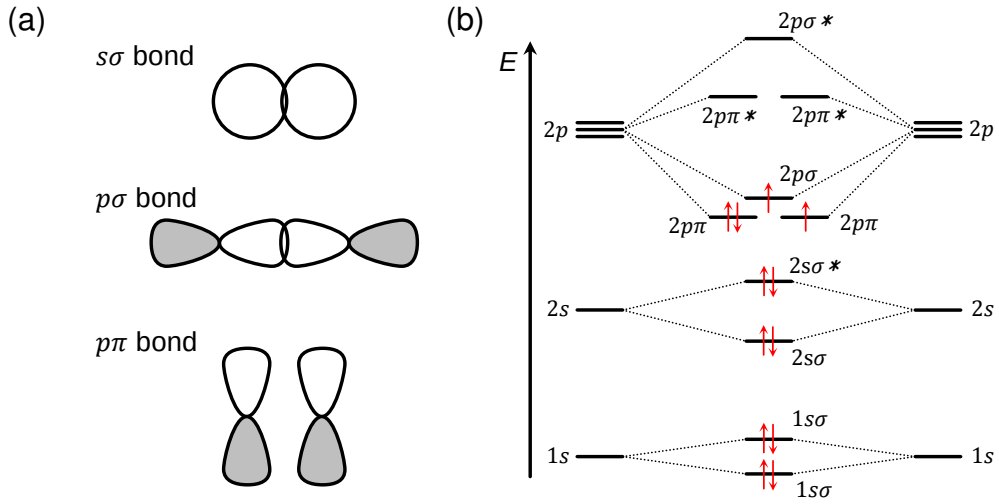

Figure 1.3: *(a) Schematic depiction of different bond types for s and p orbitals. (b) Molecular orbital diagram of dicarbon. The 2pσ bonding MO is filled with one electron even though the corresponding energy level lies above the 2pπ bonding MO. The energy gain due to electron delocalisation favours this configuration as it is bigger than the energy difference of the two molecular orbitals.*

1.1.1 Charge Transport in Conducting Polymers

Organic chemistry, as one of the two main branches of chemistry, deals with a vast variety of chemical compounds, all of which are based on carbon atoms. Carbon is the basic building block of our organic life and its chemical and physical properties are essential for our existence. The atomic number of carbon is 6 and its ground state electron configuration is $1s^2 2s^2 2p^2$. When two carbon atoms are brought into close vicinity the valence electrons will start to interact and form a chemical bond. The resulting molecule, dicarbon, can be described by the method of *linear combination of atomic orbitals* (LCAO).

The LCAO method uses the superposition principle to obtain the molecular orbital (MO) from the quantum mechanically derived atomic orbitals (see Figure 1.3). For instance, the two spherical s orbitals will form two molecular orbitals which maintain the rotational symmetry with respect to the internuclear axis. They are denoted $s\sigma$ MO. For the directional dumbbell-shaped $2p$ orbitals one can distinguish between two types of bonds. The first one, the $p\sigma$ molecular orbital again keeps the rotational symmetry with respect to the internuclear axis and occurs when the two $2p$ atomic orbitals are aligned. The second type, the so called $p\pi$ molecular orbital breaks the rotational symmetry and forms when the $2p$ atomic orbitals are parallel to each other. Generally, the σ bonds are stronger than π bonds, as there is an overlap of the atomic

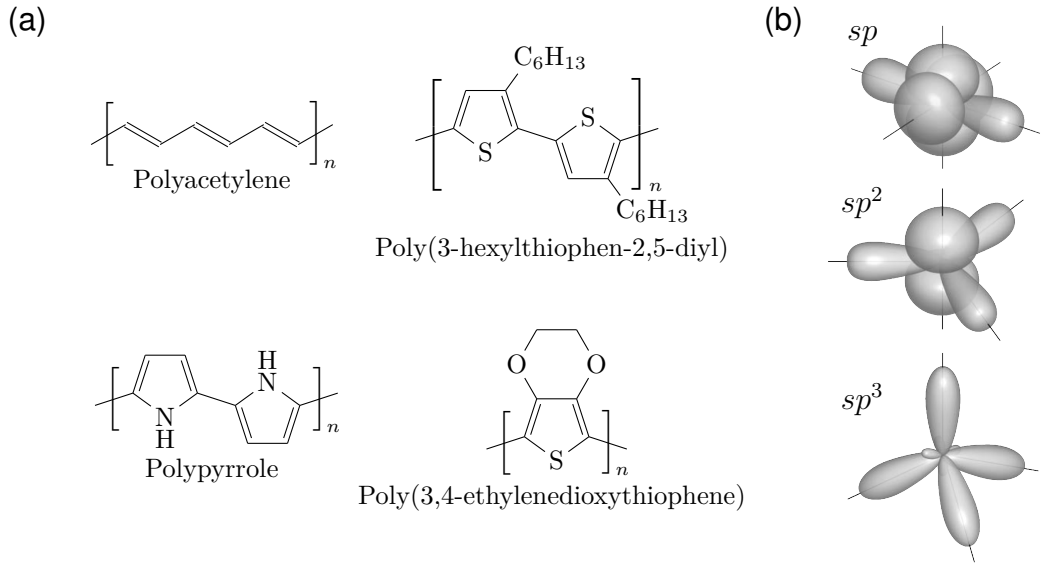

Figure 1.4: *(a) Structural formulas of some common organic semiconductors. (b) Geometric shape of sp, sp^2 and sp^3 hybrid orbitals.*

orbitals involved in the σ bond. The corresponding energy diagram of the molecular orbital of a dicarbon molecule is shown in Figure 1.3b. One can see that the molecular orbitals split up into a bonding, i.e. an energetically lower, and an anti bonding, i.e. an energetically higher level with respect to the original atomic orbitals. The anti bonding MOs are asterisked. The energy levels are then filled with the valence electrons of the single atoms, where the *highest occupied molecular orbital* (HOMO) and the *lowest unoccupied molecular orbital* (LUMO) are of special interest. In the case of dicarbon, the HOMO is, contrary to what one would expect from Hund's rules, the $2p\sigma$ bonding MO, that lies energetically slightly higher than the $2p\pi$ bonding MO. This can be explained with the fact that the energy that is required to pair electrons is higher than the actual difference of the energy levels of the two MOs, due to the repulsive nature of the electrostatic force between the two electrons.

However, the organic materials that are interesting for electronic applications consist of far more than just two carbon atoms. Some of the most common conducting polymers are shown in Figure 1.4a. In such materials carbon will most likely be found in a hybridised state, which means that one of the $2s$ electrons is promoted to the remaining free $2p$ orbital and new hybrid orbitals are formed to obtain a configuration with four unpaired valence electrons. This way, the octet rule, that is essential for stable molecules, can be satisfied more easily. Depending on the specific binding site in a molecule, the carbon atoms can be found in three different hybridised states: *sp*, sp^2 and sp^3 (see Figure 1.4b). In *sp* hybridised atoms the $2s$ and one of the $2p$ orbitals will form two orbitals that are aligned on one axis, whereas the remaining two $2p$ orbitals

are oriented orthogonal to this axis. In a molecule, this leads to the formation of a triple bond with one σ bond and two π bonds on the one side and a single σ bond on the other side of the atom. In contrast, sp^2 hybridised atoms will form planar structures, as the three hybrid orbitals are aligned in a plane with an angle of 120° and the remaining $2p$ orbital is oriented perpendicular to this plane. In such structures, one will find alternating single and double bonds, where the single bond is of σ type and the double bond consists of one σ and one π bond. Finally, the sp^3 hybridised atoms show a tetrahedral structure and they can only form single σ bonds with their surrounding neighbours.

For the field of organic semiconductors, the most important case is actually the sp^2 hybridisation. As one can see in Figure 1.4a, the structures all consist of alternating single and double bonds. On the one hand, the basic structure is formed by rigid and stable σ bonds between the sp^2 hybrid orbitals, holding the atoms at a fixed position. On the other hand, the $2p$ orbitals allow for a delocalisation of the remaining electrons across the whole structure. Such a system is called a *conjugated system*. One of the most exciting representatives of this group is *graphene*, an infinitely long hexagonal grid of sp^2 hybridised carbon atoms. The outstanding physical properties of graphene, in which charge carriers can travel practically undisturbed with a mobility of up to $15\,000\,\mathrm{cm^2\,V^{-1}\,s^{-1}}$ at charge carrier densities of the order of $10^{13}\,\mathrm{cm^{-2}}$ [Novoselov, 2005] have led to one of the quickest attributions of the Nobel prize to A. Geim and K. Novoselov, "for groundbreaking experiments regarding the two-dimensional material graphene" in the year 2010. As an immediate response, first applications of this material to the field of bioelectronics have been introduced quickly after [Hess, 2011; Park, 2012; Hess, 2013], showing its great potential for biosensing devices.

Going back to "traditional" organic semiconductors, one can distinguish between two types, namely *semiconducting small molecules*, such as for example pentacene or rubrene, and *polymeric organic semiconductors*, like poly(3-hexylthiophene-2,5-dyil) (P3HT) or poly(3,4-ethylenedioxythiophene) (PEDOT). Due to a poor solubility, semiconducting small molecules generally have to be processed via thermal sublimation techniques or organic vapour phase deposition, in order to obtain functional devices. These rather harsh processing techniques require high temperatures which makes such materials unsuitable for e.g. applications based on flexible substrates. However, semiconducting small molecules are still the best performing organic semiconductors to date. They exhibit a high crystallinity, which in turn results in high carrier mobilities of the order of $6\,\mathrm{cm^2\,V^{-1}\,s^{-1}}$ in the case of pentacene for example [Tan, 2009]. However, the great advantage of organic semiconductors over their inorganic counterparts, such as silicon with easily achievable electron mobilities of $1500\,\mathrm{cm^2\,V^{-1}\,s^{-1}}$, is their applicability to new fields, such as flexible devices [Werkmeister, 2013; Khodagholy, 2013b]. Therefore, conducting polymers have gained much interest in the past few decades. Conducting polymers stand out due to a rather easy processability. Their high solubility enable low temperature processing techniques, such as spin coating

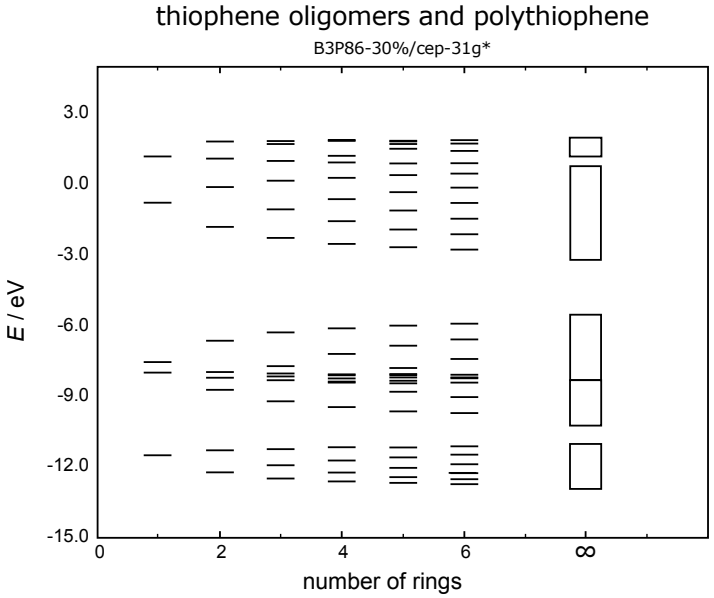

Figure 1.5: *Development of the band structure of polythiophene from energy levels of monomer through hexamer of thiophene. The number of energy levels doubles with each additional thiophene-ring until they form continuous bands. The bandgap of polythiophene is* 2 eV*. This figure is copied from [Salzner, 1998].*

[Janssen, 2007], spray deposition [Abdellah, 2010], embossing [Kafka, 2010], inkjet printing [Sirringhaus, 2000] and roll-to-roll processing [Krebs, 2009]. This potential for large scale manufacturing has led researchers to optimize the properties of such materials and mobilities of up to $1.7\,\mathrm{cm^2\,V^{-1}\,s^{-1}}$ could be achieved in a transistor device based on polythiophenes [Wei, 2013].

Polythiophenes are comprised of a long polymer chain with a sufficiently large number of aromatic pentagon rings. Experiments have shown a band gap of about 2 eV in such materials [Bundgaard, 2007]. The semiconducting properties arise again from the conjugated π electron system. If one looks at monomer thiophene, i.e. a single pentagon ring, one would detect five energy levels for the five π electrons. For dimer thiophene, the number of energy levels has doubled. Similar to the description of dicarbon (see Figure 1.3) the energy levels split into a level above and a level below the original one of monomer thiophene. With increasing number of aromatic rings, the discrete energy levels develop into a continuous band like spectrum. This can be seen in Figure 1.5, where the evolution of the energy spectrum is shown with respect to the number of aromatic rings in polythiophene. Naively, one would expect a metallic behaviour for an infinitely long polymer, as there are as many electrons as atomic sites leading to half filled bands. For example, in a simple one dimensional chain with equal distances a between the atomic sites and one electron per atomic site, the dispersion relation reveals band gaps in the reciprocal space at π/a due to the periodicity of the system.

The Fermi level in this system lies in the middle of the band and a perfect metallic conductor is to be expected. However, a simple thought experiment of Peierls shows that, if every other atom in the chain is displaced by a small distance, the effective periodicity would double to $2a$ and the band gaps in reciprocal space appear at $\pi/2a$. Hence, a new band gap occurs around the Fermi level and the system is now an insulator or semiconductor, depending on the size of the band gap. This is called the Peierls distortion [Waser, 2012, p. 141]. Exactly the same happens in the polymeric chains. Due to the alternation of single and double bonds in the conjugated system, which can be seen as a quasi one dimensional system, the distance between the atoms is not equal throughout the molecule. Thus the effective periodicity is larger and more gaps appear in the energy spectrum. The HOMO-LUMO gap in most polymers is typically only a few eV, which makes them perfect for semiconducting applications.

Unfortunately, this is as far as one can go with the analogies between organic and inorganic semiconductors. In contrast to inorganic semiconductors, with their almost perfect crystallinity over the whole structure, organic semiconductors are made of finitely long one dimensional chains. Due to weak van-der-Waals interaction, the molecules align more or less ordered, to form a film. This, inevitably, leads to the introduction of traps and defects at the intermolecular boundaries. The charge carrier transport can be described by two processes, the intramolecular crystal-like transport, which is generally very fast [Northrup, 2007], versus the intermolecular transport, governed by quantum tunnelling and thermally assisted hopping processes. The second transport mechanism is, in fact, the limiting factor in such materials and leads to considerably lower mobilities. The charge carriers need to efficiently overcome the energetic barriers that are generated at the boundaries of two adjacent molecules. This leads to a totally different behaviour of the mobility with temperature compared to inorganic semiconductors [Bässler, 1993]. In inorganic semiconductors, a higher temperature leads to more vibrational modes in the crystal and hence more potential scatterers for the charge carriers. As a result, the mobility decreases with increasing temperature. In organic semiconductors, on the other hand, the charge carriers need a certain amount of energy to overcome the transboundary barriers. This is favoured by the thermal energy at higher temperatures. Thus, the mobility increases with increasing temperature. As such a hopping transport mechanism is strongly influenced by the microscopic structure of the specific material at hand, i.e. the orientation of the molecules, the intermolecular spacing, as well as the defects and trap states, a complete model to describe the general behaviour of organic semiconductors is still missing. Instead, several different models have been developed, all of which aim to account for the low mobilities [Coropceanu, 2007].

The first category of transport theories are the *polaron* models, in which the coupling of charge carriers to the lattice vibrational degrees of freedom is considered to be the main contribution. This combination of electrons, respectively holes and phonons gives rise to quasiparticles called polarons, which act as charge carriers in the molecular system.

The hopping rate of these polarons then determines the mobility. Silinsh et al. have successfully implemented a polaron effective mass approach [Silinsh, 1995] in which they used quantum chemical calculations to evaluate the polaron formation energies and charge transfer (i.e. hopping) integrals. A more direct approach is based on the first principle one dimensional Holstein molecular model [Holstein, 1959] which starts from the basic Hamiltonian of the system. In a classical case, where the phonon energy is much less than the thermal energy, the mobility is of the form

$$\mu \propto \frac{ea^2}{k_\mathrm{B}T\hbar}\left[\frac{\pi}{2E_\mathrm{pol}k_\mathrm{B}T}\right]^{\frac{1}{2}} \exp\left(-\frac{E_\mathrm{pol}}{2k_\mathrm{B}T}\right) \quad , \tag{1.1}$$

where a is the spacing between adjacent sites and E_pol is the polaron binding energy. This represents the experimentally observed behaviour of increasing mobility with increasing temperature. However, such models neglect the presence of chemical and physical defects.

Specific *disorder* models have been developed to account for defects and trap states in particular. They all phenomenologically introduce localized energy states in the delocalized bands to account for trapping of charge carriers. H. Bässler considered a Gaussian distribution of localized states and Miller-Abrahams type hopping rates for a Monte Carlo simulation [Bässler, 1993]. He found a temperature dependence of the mobility of the form

$$\mu \propto \exp\left[-\left(\frac{2\sigma}{3k_\mathrm{B}T}\right)\right] \quad , \tag{1.2}$$

where σ is the Gaussian width of the distribution of localized states. Additionally he could account for a field dependence that obeys a Poole-Frenkel behaviour [Hill, 1971]

$$\mu \propto \exp\left(\sqrt{\frac{E}{E_0}}\right) \quad , \tag{1.3}$$

where E is the electrical field and E_0 is a characteristic parameter. This Poole-Frenkel behaviour is generally observed in experiments for fields lower than $2 \times 10^6\,\mathrm{V\,cm^{-1}}$ [Bolognesi, 2002]. However, the model of Bässler could only validate this behaviour for fields above $10^4\,\mathrm{V\,cm^{-1}}$ to $10^5\,\mathrm{V\,cm^{-1}}$.

For highly ordered organic semiconductors, such as small molecules like pentacene, the *multiple trapping and release* model has been successfully applied by G. Horowitz [Horowitz, 1998]. Initially developed for hydrogenated amorphous silicon [Le Comber, 1970], this model assumes a high concentration of localized trap levels in a narrow delocalized band. Charge carriers in the vicinity of such traps are instantaneously captured upon their arrival. This leads to a situation where almost all charge carriers are trapped. They are only released by thermal activation. The resulting mobility is then of the form

$$\mu \propto \alpha \exp\left(-\frac{E_\mathrm{t}}{k_\mathrm{B}T}\right) \quad , \tag{1.4}$$

where α is the ratio of the effective density of states at the delocalized band edge to the concentration of traps and E_t is the difference between trap level and delocalized band edge. With this model, Horowitz could explain the transport behaviour of field effect transistors based on sexithiophene by assuming an exponential distribution of trap states. A continuation of this model is given by the so called *mobility edge* model [Salleo, 2004], where one defines an energy which separates delocalized states from localized states. By thermal activation, charge carriers trapped in a localized state can access a delocalized state and become temporarily mobile. This combines the hopping process with the intermolecular drift process.

For polymeric semiconductors, such as P3HT or PEDOT, a hole transport model has been developed that correlates the mobility to the charge carrier density

$$\mu = \frac{\sigma_0}{e}\left(\frac{\left(T_0/T\right)^4 \sin\left(\pi T/T_0\right)}{\left(2\alpha\right)^3 B_\mathrm{c}}\right)^{T_0/T} \cdot p^{T_0/T-1} \quad , \tag{1.5}$$

where σ_0 is a prefactor for the conductivity, α^{-1} is the effective overlap parameter between localized states, T_0 reflects the width of the exponential density of states and B_c is a critical number for the onset of percolation. This so called *hopping percolation model* depends again on a Gaussian distribution of localized states and could accurately describe the difference between experimentally derived mobilities of field effect transistors and light-emitting diodes [Tanase, 2003] and has recently been applied to PEDOT:PSS based organic electrochemical transistors to improve the transconductance by 120 % [Friedlein, 2015].

All of these models aim to explain the behaviour of the mobility in organic semiconductors, that is so different compared to mono crystalline materials. The lack of periodicity, the complex microstructure, the interaction between charge carriers and molecules – all of these are factors that make it difficult to accurately describe such systems. Of course, this is only a small excerpt and there are many more transport theories that are more or less sophisticated. This is just to show that the charge transport mechanism in organic semiconductors is to date still open for debate.

1.1.2 PEDOT:PSS

PEDOT:PSS, short for poly(3,4-ethylenedioxythiophene) doped with polystyrene sulfonate, is one of the most commonly used organic semiconductors in the scientific community due to its outstanding properties. An optical absorbance in the visible spectrum with a peak absorption at around 650 nm makes the polymer appear bluish. When deposited sufficiently thin, the material is transparent and the opacity can be tuned electricochemically via oxidation or reduction. Organic electrochromic windows are based on this operation principle [Heuer, 2002; Andersson, 2007] and could be used

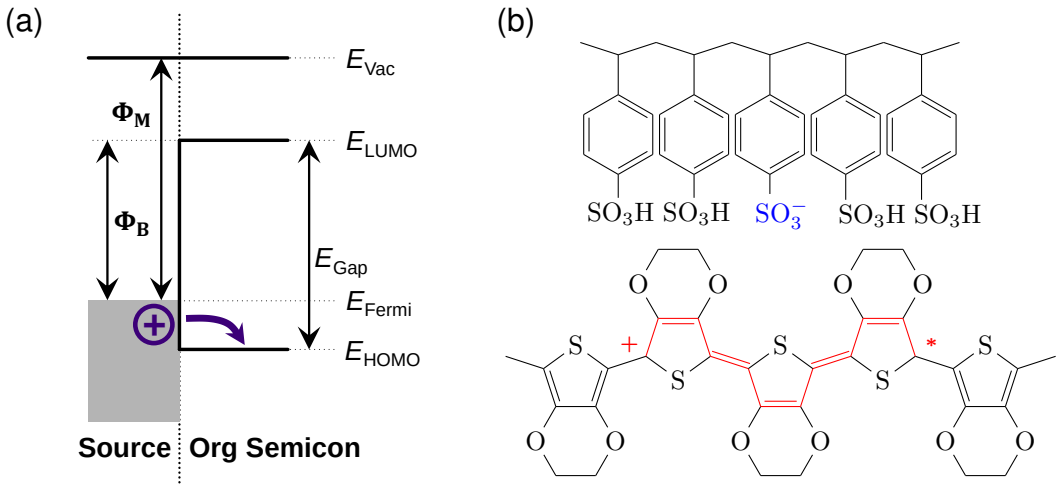

Figure 1.6: *(a) Schematic illustration of charge carrier injection in organic semiconductors. The metal work function Φ_M lies suffeciently close to the HOMO band edge E_{HOMO} such that holes can easily be injected into the HOMO but electrons cannot overcome the energetic barrier Φ_B to the LUMO. (b) Doping mechanism in PEDOT:PSS. The negative sulfonate group of the PSS chain induces a chemical change in the bond structure of the PEDOT molecule, which in turn leads to a mobile positive charge carrier along the backbone of the polymer.*

as self-darkening rear-view mirrors in automobiles. The electrical conductivity of PEDOT:PSS can be boosted up to 1400 S cm^{-1}, rendering it very attractive as electrode in organic solar cells [Kim, 2011]. With an intrinscally high work function, PEDOT:PSS is used as an efficient hole injection layer in organic light emitting diodes [Kok, 2004].

All of these capabilities combined in one material has led to some outstanding all-organic sensor systems. For example, Berggren et al. demonstrated a full system printed on a regular paper sheet, incorporating a push-button input device with three buttons that upon pressing would lead to correct output on an adjacent display on the sheet based on transistor logic powered by built-in batteries. All of these components are comprised of PEDOT:PSS and such a system could be useful as authentication sticker or packaging security sensor [Berggren, 2007a].

As already stated, PEDOT:PSS is a hole conducting conjugated polymer. In principle, organic semiconductors can intrinsically conduct both holes and electrons due to the delocalized π orbitals. However, the Fermi level of such systems is set by the work function Φ_M of the metal that is used to electrically contact the polymer (see Figure 1.6a). And it is a caprice of nature that the metals traditionally used for such applications (for example gold) have a work function that is energetically close to the HOMO level of most organic semiconductors, therefore allowing facile injection of positive charge

carriers [Coropceanu, 2007]. This makes that practically all conducting polymers are used as p-type semiconductors. However, effort is expended to improve materials that allow for effective electron conduction to render them useful for p-n junctions or complementary circuits for high-performance or ultralow-power applications [Sakamoto, 2004; Klauk, 2007].

But for the purpose of the present dissertation, PEDOT:PSS as a p-type organic semiconductor is sufficient. In close analogy to the inorganic counterpart silicon, where impurities with an extra vacancy, such as boron or aluminium, are introduced into the perfect crystal structure to bind one free electron from the surrounding silicon atoms and therefore "generating" a positive charge carrier, the PSS chain with negatively charged sulfonate groups introduces lattice distortions along the PEDOT backbone that upon oxidation lead to the formation of a positive polaron (see Figure 1.6b). This polaron, as an effective positive charge carrier can thus contribute to the overall charge transport. In general, the content of the dopant is of the order of 1:2 to 1:3 (PEDOT to PSS) which leads to a highly oxidized and degenerately doped material [Rivnay, 2016]. The lattice distortions lead to additional energy splitting according to Peierl's theorem and at such elevated doping levels new energy bands appear inside the band gap of the polymer due to the overlap of several polaron states. These additionally available small energy gaps lead to an increased absorption of light in the visible or near infrared range and therefore the polymer appears darker when doped.

Additionally, the high PSS content stabilizes the material in an aqueous environment and leads to the formation of colloidal gel particles with PEDOT-rich domains incorporated in a PSS-rich matrix [Rivnay, 2016]. Whereas the PEDOT-rich domains are essential for the electronoic charge transport, the PSS-rich matrix facilitates ionic charge transport with ion mobilities as high as in bulk water [Stavrinidou, 2013]. It is this unique feature of mixed ionic and electronic conductivity that renders PEDOT:PSS so useful for bioelectronic applications. Since biological signals are mostly expressed in ionic currents (depolarization and repolarization in neurons, signal transduction in cells, pacemaking in cardiomyocytes), this material can directly "communicate" through an uptake of ions leading to oxidation/reduction of the polymer and therefore to a measurable change in both optical and electrical properties.

Electrochemical polymerization has been the initial method of choice for scientists synthesizing PEDOT:PSS. Here, either a constant current (galvanostatic) or constant voltage (potentiostatic) is applied to an EDOT monomer solution in a PSS electrolyte. The electrostatic energy is sufficient to oxidize the monomer and produce a radical cation. The free electron is then likely to pair with another free electron of a second radical to form a dimer. Upon continuation a long polymer chain can be formed. The PSS acts then as counterion to balance the oxidative reaction and stabilizes as well as dopes the PEDOT polymer:

$$PEDOT + PSS^{-} : Na^{+} \leftrightarrow PEDOT^{+} : PSS^{-} + Na^{+} + e^{-} \tag{1.6}$$

With this method, very pure films of PEDOT:PSS can be deposited on virtually any electrode surface. The surface morphology can be tuned by the electrostatic parameters (i.e. deposition speed, current amplitude or voltage amplitude) [Cui, 2003] and the film thickness is roughly proportional to the total charge transferred to the film, where the exact empirical relationship is subject of ongoing research by Martin et al.

Nowadays, there exist commercially available aqueous dispersions of PEDOT:PSS (Baytron P from Bayer or Clevios PH1000 from Heraeus) for solution processable low-temperature fabrication techniques such as spin-casting or inkjet printing. For all projects that are presented in this dissertation, we chose to work with Clevios PH1000 with an off-the-shelf specific conductivity of $850\,\mathrm{S\,cm^{-1}}$ after addition of a co-solvent (5 % v/v dimethyl sulfoxide or 5 % v/v ethylene glycol) and a viscosity of 15 mPa s to 60 mPa s (for reference, the viscosity of water at 20 °C is about 1 mPa s and that of honey is about 10 000 mPa s). The addition of the co-solvent rearranges and enlarges the PEDOT-rich domains allowing for a better pathway for electronic charge transport [Pathak, 2015]. In the same way, it diminishes the ion charge transport as the PSS-rich matrix gets partially washed out and for example a reduction of the ion mobility from $2.2\,\mathrm{cm^2\,V^{-1}\,s^{-1}}$ to $1.7\,\mathrm{cm^2\,V^{-1}\,s^{-1}}$ for 5 % v/v of ethylene glycol (EG) and $1.3\,\mathrm{cm^2\,V^{-1}\,s^{-1}}$ for 50 % v/v can be observed [Rivnay, 2016]. The best compromise between ionic and electronic conductivity has been evaluated to 5 % v/v addition of ethylene glycol.

To allow for a better film formation, a surfactant such as dodecylbenzenesulfonic acid (DBSA) is widely used. This also affects the conductivity in a positive way but induces a phase separation in the mixture for concentrations higher than 0.5 % v/v [Zhang, 2015]. As already stated above, the addition of a silane, 3-glycidoxypropyltrimethoxysilane (GOPS), can reduce film delamination as it acts as a cross-linker to oxygen plasma induced hydroxyl groups at the substrate surface. The chemical reaction happening is twofold: (1) during hydrolysis, the alkoxylsilane groups are converted to reactive silanols and (2) during condensation, the silanols form siloxane bonds with hydroxyl groups from neighbouring molecules as well as the substrate:

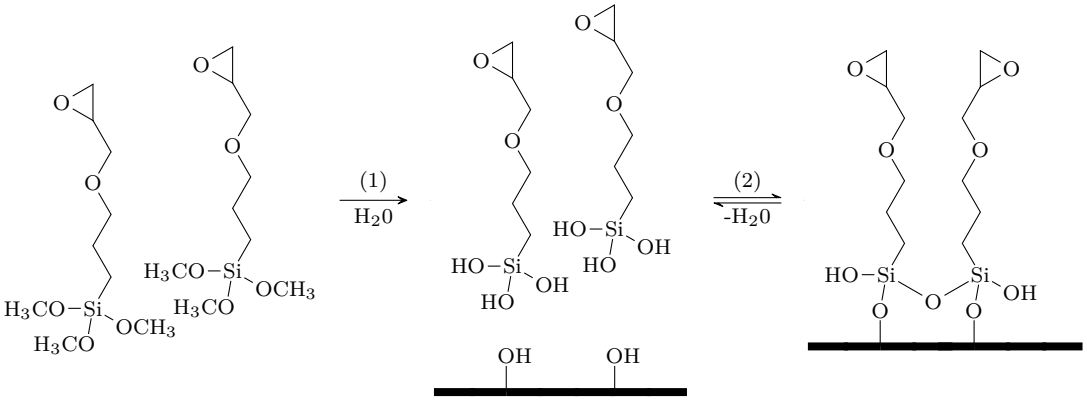

PEDOT:PSS (Clevios PH1000)	19 mL	(19 g)
EG (Sigma Aldrich)	1 mL	(1.11 g)
DBSA (Acros Organics)	50 µL	(0.053 g)
sonicate for roughly 20 min		
GOPS (Sigma Aldrich)	188 µL	(0.2011 g)
sonicate for another 5 min		

Table 1.1: *Formula for about* 20 mL *of spincast processable PEDOT:PSS with good film formation and best compromise between ionic and electronic conductivity used at the department of bioelectronics in Gardanne.*

The hydrolysis step is very quick and already starts at room temperature [Xue, 1987]. Therefore, it is best practise to add this component at the very last step. The condensation step highly depends on the curing temperature and has been reported to be reversible in the presence of water [Pavlovic, 2011]. For thin films, curing temperatures from 90 °C to 250 °C provide a stable cross-linked film.

A general solution preparation is shown in Table 1.1. The PEDOT:PSS together with co-solvent and surfactant is sonicated for about 20 min to break up PEDOT:PSS aggregates and thoroughly mix the components. After an exchange of the sonication bath to make sure that the temperature in the bath is kept low, the silane is added and the solution sonicated for another 5 min. Meanwhile, the substrate is treated with a mild oxygen plasma (50 sccm O_2, 100 W, 2 min). The ready solution is then filtered and spincast onto the substrate where the thickness is proportional to the spin speed. After, the film is cured at 125 °C for about 1 h to cross-link the silane and evaporate all solvents. In order to achieve a stable and highly conductive film, the PEDOT:PSS needs to swell in DI water. This also removes potential low-molecular weight particles that may remain from the solution and purifies the polymer.

1.1.3 Electrodes

The word "electrode" is a composition of *electron* and *hodos* (ὁδός greek for *path, way, road*) and could be translated with *the path of the electron*. It is the most essential medical device when it comes to interfacing with electrical signals of biological origin and in essence is comprised of an electron conductor in contact with an electrolyte (see Figure 1.7). This can be modelled as an equivalent electronic circuit, where the electrolyte is represented as a resistance in series with the electrodes. The resistivity of the electrolyte is a function of the concentration of ions present in the solution (i.e. the ionic strength). The more ions there are, the more conductive the electrolyte will be. Moreover, the resistance in the equivalent circuit is also depending on the area of the electrode. One can distinguish between two types of electrodes, namely ideally

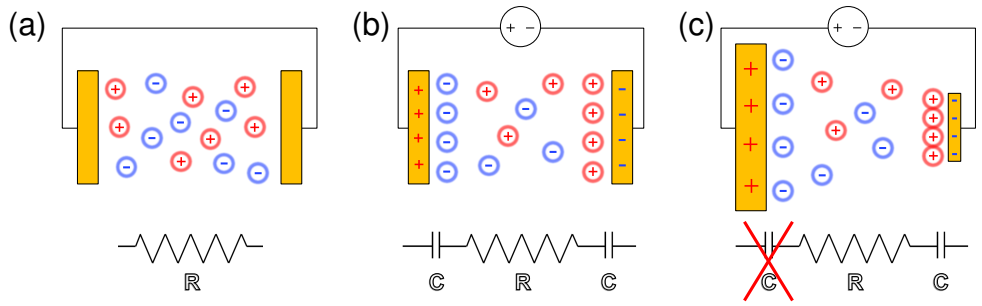

Figure 1.7: *Schematic representation of an electrode circuit with ideally polarizable electrodes. The electrodes are depicted as yellow squares, the electrolyte as ionic spheres with positive and negative charge. (a) Ionic distribution in the absence of an external voltage. The charge distribution inside the electrolyte is neutral and the resistivity is given by the ionic strength. (b) When applying a voltage, the electrodes are getting charged and ions of opposite charge are accumulating at the electrode-electrolyte interface, leading to two capacitances in series with the electrolyte resistance. (c) If one electrode of the circuit is much bigger than the other electrode, the contribution of that capacitance to the electronic circuit can be neglected.*

polarizable and ideally non-polarizable electrodes that are defined by their property to allow electronic current across the electrode-electrolyte interface (non-polarizable) or not (polarizable).

For ideally polarizable electrodes, electrons that accumulate at the electrode-electrolyte interface will affect the ionic distribution inside the electrolyte through electrostatic forces (see Figure 1.7b). The charge accumulation leads to a capacitive contribution of the electrodes to the electronic circuit, due to the formation of a so called *electrical double layer* (EDL). Any voltage that is applied to the circuit will partially drop across the EDL and across the electrolyte:

$$V_{\text{applied}} = 2 \times V_{\text{C}} + V_{\text{R}} = 2 \times \frac{I}{i\omega C} + I \cdot R \quad , \tag{1.7}$$

where I is the current, C the electrode capacitance, R the electrolyte resistance and ω the angular frequency of the applied voltage signal V_{applied}. Note the imaginary unit i in the equation, meaning that the capacitance shows a transient behaviour. To get the amplitude, one would need to calculate the absolute value ($\text{abs}(z) = \sqrt{\text{Re}(z)^2 + \text{Im}(z)^2}$). It can be seen that the voltage drop across the electrodes is inversely proportional to the capacitance. As the capacitance scales with area, medical devices are usually comprised of one big so called *reference electrode* that does not contribute and is merely there to close the electronic circuit, and one *sensing electrode* where all the interface effects are taking place (see Figure 1.7c). A perturbation inside the electrolyte that might be at the origin of a biological signal of interest, will then only be picked up

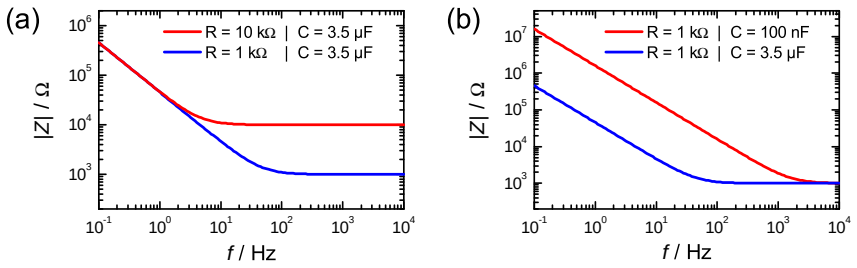

Figure 1.8: *Impedance spectra for different resistance and capacitance values. (a) A lower electrolyte resistance leads to an improved impedance at high frequencies. The resistance values are typical for a sodium chloride solution of* 1 mM *(*10 kΩ*) and* 100 mM *(*1 kΩ*). (b) A higher capacitance leads to an improved impedance at low frequencies. The capacitance values are typical for a gold electrode of* 500 µm *by* 500 µm *(*100 nF*) and a PEDOT:PSS electrode* 500 µm *by* 500 µm *by* 350 nm *(*3.5 µF*).*

by the sensing electrode and the resulting measurable current is dominated by that interface capacitance. One figure of merit, as to how good an electrode can pick up a signal, is the impedance Z defined as

$$Z = \frac{\partial V}{\partial I} = R - \frac{i\omega}{C} \quad \rightarrow \quad |Z| = \sqrt{R^2 + \frac{1}{\omega^2 C^2}} \quad . \tag{1.8}$$

In Figure 1.8 are shown typical impedance spectra for varying parameters. It can be seen, that a change in the electrolyte resistance does merely affect the high frequency domain, whereas a change in the electrode capacitance affects the low frequency range. As biological signals originate in rather low frequencies (one of the fastest signals in the human body, a neural firing event, has a typical width of 1 ms, i.e. 1 kHz [Buzsáki, 2012]), it can be seen how a lower electrode capacitance can immediately improve the signal quality.

There are several ways to obtain a lower capacitance, all of which aim to increase the effective surface area of the electrode. One simple way is to increase the electrode size [Abdurrahman, 2007]. However, this is not often applicable due to the demand for high spatial resolution for example in EEG recordings. Another way is to use annealing and etching techniques to increase the surface roughness [Kerner, 1998]. With the advances in microstructuring techniques, an increase in surface area can be achieved by using three dimensional micro-shapes on the electrode surface [Meng, 2015].

Most recently, it has been shown that a PEDOT:PSS coating of electrodes can greatly improve the impedance and specific EEG patterns could be captured that cannot be well resolved with metal electrodes [Leleux, 2014]. In Figure 1.8b is shown a theoretical comparison of a gold electrode in contact with a 100 mM NaCl solution and a PEDOT:PSS electrode of same size with a coating thickness of only 350 nm. The impedance is improved by almost two orders of magnitude. Recent studies have at-

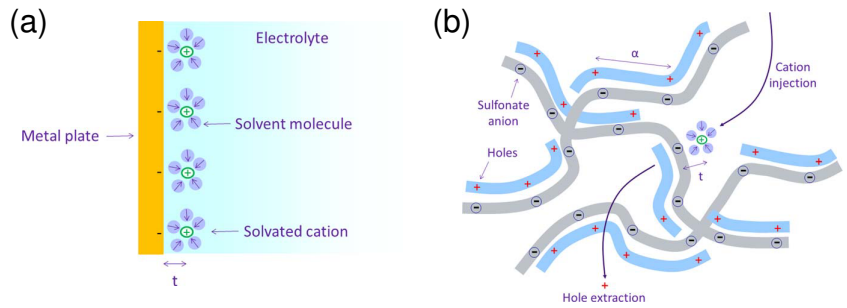

Figure 1.9: *(a) EDL formation in a planar metal electrode. The ions accumulate along the planar surface. (b) EDL formation in PEDOT:PSS. The ions can penetrate into the material and accumulate along the PSS polymer chains. Images taken from [Proctor, 2016].*

tributed this effect to a so called volumetric capacitance of the polymer [Proctor, 2016]. Unlike for metal electrodes, ions can penetrate into the conducting polymer. They will accumulate along the PSS backbone and compensate the negative charge of the sulfonate ion. This, in turn, extracts holes from the PEDOT, one for each cation, which contribute to a net electric current. Proctor et al. have modelled this as a stack of parallel plate capacitors spaced by a distance α that is proportional to the number of sulfonate anion/hole pairs present in the polymer. With reasonable assumptions, they could calculate a volumetric capacitance of $6\,\mathrm{F\,cm^{-3}}$ to $57\,\mathrm{F\,cm^{-3}}$ that is in accordance with experimentally measured values. When comparing these values of the typical EDL capacitance of about $1\,\mu\mathrm{F\,cm^{-2}}$ to $10\,\mu\mathrm{F\,cm^{-2}}$, one can immediately see that thin film coatings of PEDOT:PSS can increase the electrode capacitance by several orders of magnitude.

However, a PEDOT:PSS electrode cannot be fully described by only using a resistance and a capacitance in series as an equivalent circuit model. Earlier, we made the assumption that the electrode would be ideally polarizable, meaning that in equilibrium ions will perfectly compensate for the accumulated charge at the electrode-electrolyte interface. In real life, however, there is always a non-negligible Faradaic current due to redox reactions happening at the electrode. A good example of an almost ideally non-polarizable electrode would be a Ag/AgCl electrode. The chemical reaction happening at the interface with the electrolyte in the presence of an external voltage,

$$\mathrm{AgCl}(s) + e^- \rightleftharpoons \mathrm{Ag}(s) + \mathrm{Cl}^- \quad , \tag{1.9}$$

leads to a net charge flow from the electrode into the electrolyte. Such a system is widely used as reference electrode, where one wants to eliminate an additional potential drop due to the interface capacitance, as for example important in pH meters or ECG and EEG recording systems. In PEDOT:PSS electrodes, only a fraction of total current can be attributed to Faradaic currents. To take this effect into consideration, the simple RC

equivalent circuit model is modified into an R(RC) model, with an additional resistance in parallel to the interface capacitance. This will affect the impedance spectrum only in the very low frequency range, below 1 Hz.

1.2 Organic Electrochemical Transistor

Electrodes as medical recording device of electrical signals originating from the body are to date still state-of-the-art. For example, the most pure recording of a neural firing event can be achieved with the so called *patch clamp* technique in a whole cell configuration. Here, a single neuron cell is approached with a micron sized glass capillary filled with electrolyte and a tiny suction leads to a rupture in the cell membrane to make a physical contact with the intracellular medium. An electrode inside the glass capillary allows then for measuring the microscopic currents upon a firing event [Kodandaramaiah, 2012]. A GΩ seal between the capillary and the cell membrane ensures that no ions can reach the electrode other than from the inside of the cell and thus the intracellular potential can be extracted. The ionic currents are small, in the range of nA and need to be amplified through differential amplifier systems. This inevitably leads to noise pick-up that also gets amplified together with the signal. Electrical noise is by definition any signal that is not part of the biological event. A common example would be the 50 Hz noise generated from our electricity grid. The energy generated in power plants is distributed to the end-user with an AC frequency of 50 Hz and electromagnetic radiation from nearby devices plugged into the general electricity grid will be picked up by the electrode and superimpose with the biological signal. If the signal of interest is of much smaller amplitude than the noise, i.e. a small signal-to-noise ratio (SNR), it becomes hard to analyze the data. Post-processing the data with particular filters can help improve the signal quality, but it is always better to record with a high signal-to-noise ratio. For instance, there are noise sources that span over the whole frequency range, such as thermal noise or shot noise. The SNR for electrodes can be written as

$$SNR_{\text{electrode}} = \frac{\alpha \cdot S}{\alpha \cdot N + \alpha \cdot N_{\text{line}}} \quad , \tag{1.10}$$

where α is the amplification factor, S is the signal amplitude N is the noise at the recording site and N_{line} is the noise along the electrical leads to the amplifier. For practical reasons, usually the *root mean square* (RMS) is taken as a measure of the amplitude of the signal.

Since the recording in patch-clamp measurements takes place directly at the biological origin, the signal can be well resolved and high signal-to-noise ratios can be achieved with this technique. However, it is not always possible to get as close as needed to the biological event and the further away one has to record, the more the signal will be altered and attenuated. The signal needs to pass through different layers of tissue

with different conductivity. For example, the brain-to-skull conductivity ratio has been estimated to 18.7, meaning that the skull is almost 19 times less conductive than the brain tissue [Zhang, 2006]. With such numbers, it becomes evident that a high signal-to-noise ratio is essential.

Therefore, in the past few years effort has been expended to improve the signal-to-noise ratio (SNR) and one solution is the use of active transducing amplifiers as recording element. In that case, the SNR will be increased due to the preamplification β of the signal

$$SNR_{\text{transistor}} = \frac{\alpha\beta \cdot S}{\alpha\beta \cdot N + \alpha \cdot N_{\text{line}}} \quad . \tag{1.11}$$

When comparing this with the SNR of an electrode, one can see that the SNR of a transistor recording device will in theory always be higher for as long as the preamplification factor β is greater than one. This has been demonstrated by Khodagholy et al., where they compared brain activity recordings with electrodes and transistors on the surface of a rat brain [Khodagholy, 2013a]. Both devices were comprised of PEDOT:PSS, and in direct comparison, the transistor device showed a SNR of 26 dB to 32 dB more than the electrode. Given the logarithmic nature of the dB unit, this corresponds to an amplitude ratio of 20 to 40 and utterly shows the superior recording capabilities when amplifying the signal close to their biological origin.

1.2.1 Operation Principle

But how exactly does an organic transistor for biological applications work? Just like a standard metal-oxide field-effect transistor (MOSFET) (see Figure 1.10a) it is a three terminal device, with a source, drain and gate electrode. The source and drain contacts are connected through an active material (the semiconductor) which provides a constant current flow from the source to the drain electrode upon the application of a source-drain bias V_{DS}. This current is denoted the *drain current* I_{D}. The charge carriers depend on the nature of the material (n-type for electron conductors and p-type for hole conductors). The gate contact is physically separated from the semiconductor by a dielectric and is used to modulate the current flow inside the semiconductor via application of a gate bias V_{GS}. Depending on the operation mode of the transistor, charge carriers are either accumulated or depleted with the application of a gate bias. In traditional MOSFET structures one talks about inversion layer when the conducting channel is created at the semiconductor-dielectric interface, as the energy levels of the semiconductor are deformed up until the conduction band for p-type semiconductors (valence band for n-type semiconductors) lies below (above) the Fermi level and the energy states can thus be filled with minority charge carriers that can then be extracted at the source-drain contacts.

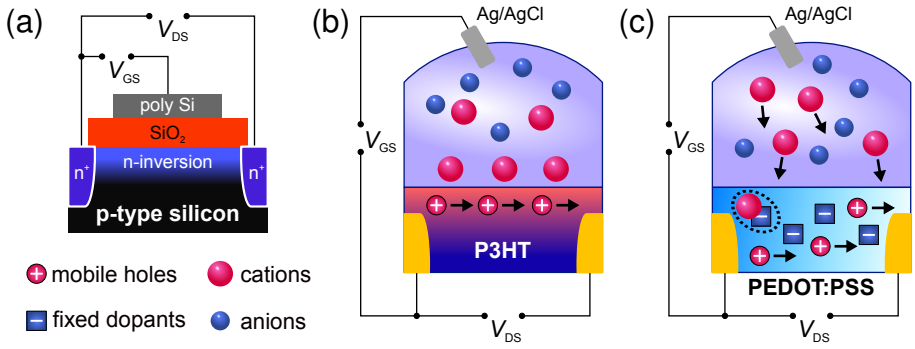

Figure 1.10: *(a) Silicon MOSFET. Upon application of a gate-voltage the energy bands are getting deformed until the conduction band lies below the Fermi level and an inversion layer is created. (b) Electrolyte gated organic field effect transistor with organic semiconductor not permeable to ions. The ions accumulated at the electrolyte-semiconductor interface facilitate charge transport of holes in the organic semiconductor. (c) Organic electrochemical transistor with organic semiconductor permeable to ions. The intrinsically doped material gets dedoped upon application of a gate voltage, where positive ions penetrate into the semiconductor and compensate for one dopant anion, effectively reducing the number of mobile holes.*

There is one fundamental difference between transistors used for biological applications and silicon MOSFETs used in CMOS technology and this is the use of an electrolyte as dielectric (see Figure 1.10). As the effectiveness of the gate, defined as transconductance

$$g_{\mathrm{m}} = \frac{\partial I_{\mathrm{D}}}{\partial V_{\mathrm{GS}}} \quad , \tag{1.12}$$

is limited by the capacitance of the dielectric, hence the thickness of the dielectric layer, an electrolyte gated transistor can achieve a much higher transconductance at lower operation voltages due to the formation of electrical double layers with a high capacitance. In electrolyte gated transistors, the operation voltages are typically of less than 1 V which is beneficial for biological applications in order to avoid electrocution of living tissue.

Another aspect that is important for biological applications is the biocompatibility of the device. Often, medical devices need to be implanted to allow for proper function and the body must not reject the foreign object. But also for less invasive approaches, such as epidermal applications, skin irritation and inflammation may be an issue. There have been recent demonstrations as to make silicon based devices biocompatible or even bioresorbable, meaning the device will physically degrade inside the living body after having done its purpose, without leaving a trace [Hwang, 2012]. This can be achieved by grinding the materials down to a thickness of less than 100 nm, turning the once brittle silicon single crystal into a flexible membrane that dissolves in deionized water. With such a technique, sophisticated wireless sensor devices based on CMOS

technology can be used as transient bioelectronic devices for example for post-surgical monitoring. On the other hand, the intrinsic organic nature of conducting polymers makes them ideal candidates for biological applications and many such materials have been tested for their biocompatibility [Berggren, 2007b; Scarpa, 2010a; Bhatt, 2016]. Some people even go as far as to eat their transistors, built with perylene dimide as semiconductor, adenine and guanine as gate dielectric, and gelatine as substrate, all of which are natural or nature-inspired materials [IrimiaVladu, 2010]. Straight forward and facile processability together with low cost fabrication methods renders conducting polymers an alternative route to silicon based devices.

As far as organic transistor devices are concerned, one can distinguish between two types depending on the permeability of the conducting polymer to cations and anions. In electrolyte gate organic field effect transistors (EGOFET), ions cannot penetrate into the active material and will thus accumulate at the electrolyte-semiconductor interface upon application of a gate bias (see Figure 1.10b). Due to the electric field generated at the dielectric, in that case the electrical double layer, the electrical current inside the conducting polymer can be modulated. The operation principle is in close analogy to MOSFET devices but one does not speak of inversion layer since the charge carriers in the active material are set by the injection barrier of the source and drain contacts (see Figure 1.6). Common organic semiconductors for OFET applications are P3HT or pentacene [Cramer, 2012; Magliulo, 2013]. While these kind of devices are useful in various sensing applications that rely on interface reactions such as ion selectivity or DNA recognition [Scarpa, 2010b; Kergoat, 2012] they generally have a rather low transconductance (around 50 µS for a P3HT EGOFET) compared to organic electrochemical transistors (OECT) [Khodagholy, 2013b].

In an OECT, the active material is permeable to ions (see Figure 1.10c), and as already stated above (see Figure 1.9) this leads to a significant increase in the effective capacitance of the device. The presence of dopant ions inside the conducting polymer leads to a chemical redox reaction upon application of a gate bias, which in turn modulates the available charge carriers and thus the drain current. Put in a simple picture, one dopant anion in the conducting polymer "generates" a mobile hole in order to ensure charge neutrality. If a cation from the electrolyte is pushed into the conducting polymer by application of a positive gate bias, this cation will neutralize the dopant anion, which is thus no longer able to "generate" the mobile hole. This one-to-one ratio of hole versus cation together with the bulk effect of the volumetric capacitance makes for large transconductance values in the range of mS. The first OECT has been demonstrated by the group of Mark Wrighton in the 80s, for which they used polypyrrole as conducting polymer [Kittlesen, 1984]. However, intensive research over the past few decades have employed other materials such as PEDOT:PSS for depletion mode transistors or more exotically triethylene glycol chains grafted onto 2,2'-bithiophene and copolymerized with thiophene (simply g2T-T) for accumulation mode transistors [Nielsen, 2016]. As far as stability and performance are concerned, however, PEDOT:PSS is still the

champion material and is thus the most studied conducting polymer for these kind of applications.

1.2.2 Transistor Characteristics of PEDOT:PSS based OECTs

Typical electrical characteristics of a PEDOT:PSS OECT are shown in Figure 1.11. The *output curve* shows how the transistor behaves when keeping the gate voltage constant and sweeping the drain voltage. In this graph, one can distinguish between two operation regimes of the device. The *linear regime* is specified for lower drain voltages, where the drain currents scales linearly with the drain voltage. The *saturation regime* is at the other end of the scale, at high drain voltages, and denotes the part where the drain current is independent of the drain voltage. The derivative of the output curve, the so called *drain conductance* g_{d} can give a quick overview of the two operation regimes and is of more importance when the drain voltage cannot be kept at a fixed value (see Section 1.3).

But usually, for sensing applications the drain voltage is held constant and the gate voltage is swept from negative to positive values as seen in the *transfer curve*. Here, one can immediately see how the drain current gets modulated upon the application of a gate bias, that leads to an almost complete dedoping of the PEDOT:PSS channel at high positive gate voltages. The derivative of the transfer curve gives the transconductance, the figure of merit of any transistor and a measure of the sensitivity of the device to changes in the gate voltage. In contrast to the transconductance of silicon MOSFETs, that is monotonically increasing, in OECTs the transconductance has a bell-shape characteristic with a peak transconductance at one particular gate voltage. This particularity can be explained with the disordered nature of the charge carrier mobility in conducting polymers [Friedlein, 2015]. The mobility is expected to be depending on the density of states, which in such materials shows a Gaussian distribution. When the energy levels are filled up with charge carriers up to the tail in the density of states, the states at the Fermi level are physically or energetically to far apart to allow for an effective displacement and thus the charge carriers get trapped. Therefore, the drain current at high negative gate voltages tends to saturate and the transconductance diminishes.

It can be seen that both output and transfer curves are depending on the geometry of the device. As theory predicts, the drain current scales linearly with the aspect ratio of the channel

$$I_{\mathrm{D}} \propto \frac{W}{L} \quad . \tag{1.13}$$

Furthermore, the peak transconductance is also increasing, but at the same time shifting towards more positive gate voltages for higher $^{W}/_{L}$. Therefore, the design of the OECT can be a useful means to optimize the operation point of the device [Rivnay,

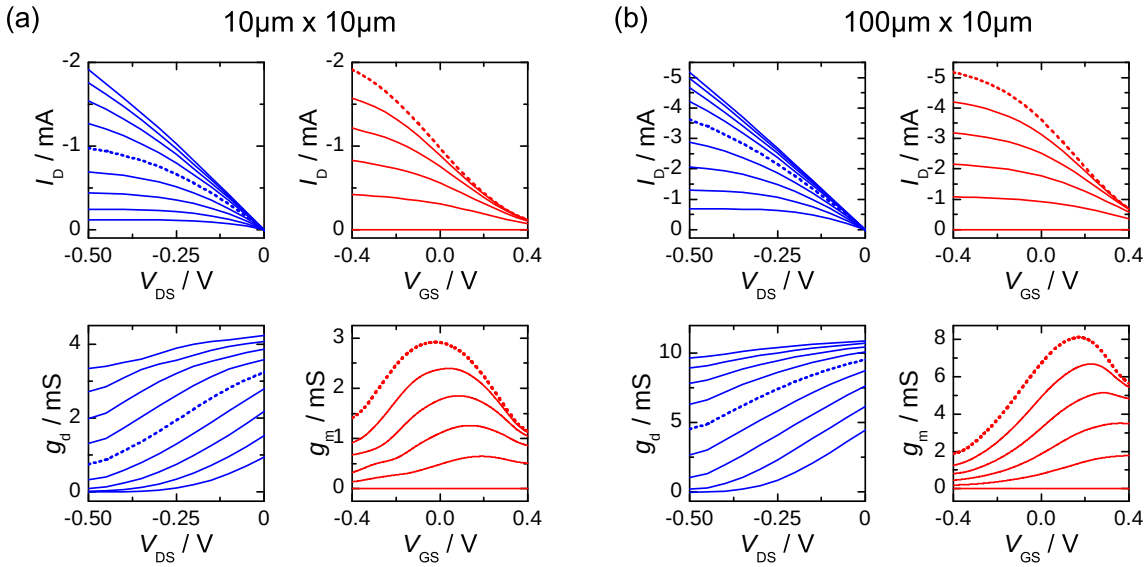

Figure 1.11: *Typical characteristic curves for PEDOT:PSS OECTs with different aspect ratio of the channel - (a)* $W = 10\,\mu m$, $L = 10\,\mu m$ *and (b)* $W = 100\,\mu m$, $L = 10\,\mu m$. *The output curve and corresponding derivative are shown in blue, the gate voltages from top to bottom are* $V_{GS} = -0.4\,V$ *to* $V_{GS} = 0.4\,V$ *in steps of* $\Delta V_{GS} = 100\,mV$. *The curve at* $V_{GS} = 0\,V$ *is highlighted as dashed bold line. The transfer curve and corresponding derivative are shown in red, the drain voltages from top to bottom are* $V_{DS} = -0.5\,V$ *to* $V_{DS} = 0\,V$ *in steps of* $\Delta V_{DS} = 100\,mV$. *The curve at* $V_{DS} = -0.5\,V$ *is highlighted as dashed bold line. The channel thickness for both devices is around* 70 nm.

2013]. For instance, enzymatic reactions of glucose oxidase on platinum nanoparticles, used in current glucose sensors, are typically happening at voltages of above $V_{GS} > 0.3\,V$ and an optimized device geometry of the OECT can be used as an effective transducer for such a sensor [Strakosas, 2017].

Whereas the steady state behaviour is important for the selection of a proper operation point and useful for sensing applications where the drain current shows a permanent shift through the biorecognition event (as for example metabolite detection shown in Chapter 2), for some sensing and actuation applications, especially in electrophysiology, the transient behaviour of the device is of uttermost importance. During the depolarization and repolarization of a neuron during a firing event, the electrical field on a local scale first increases, then decreases below its initial level and then regenerates to the initial level, and this on a time scale of a few ms. In order to capture this event with an OECT, the device has to be fast enough so that the local gate voltage modulation can be translated into a drain current change. In order to characterize the transient behaviour of a transistor, both the current from source to drain (drain current) as well as from source to gate (gate current) are monitored upon the application of a sinusodial

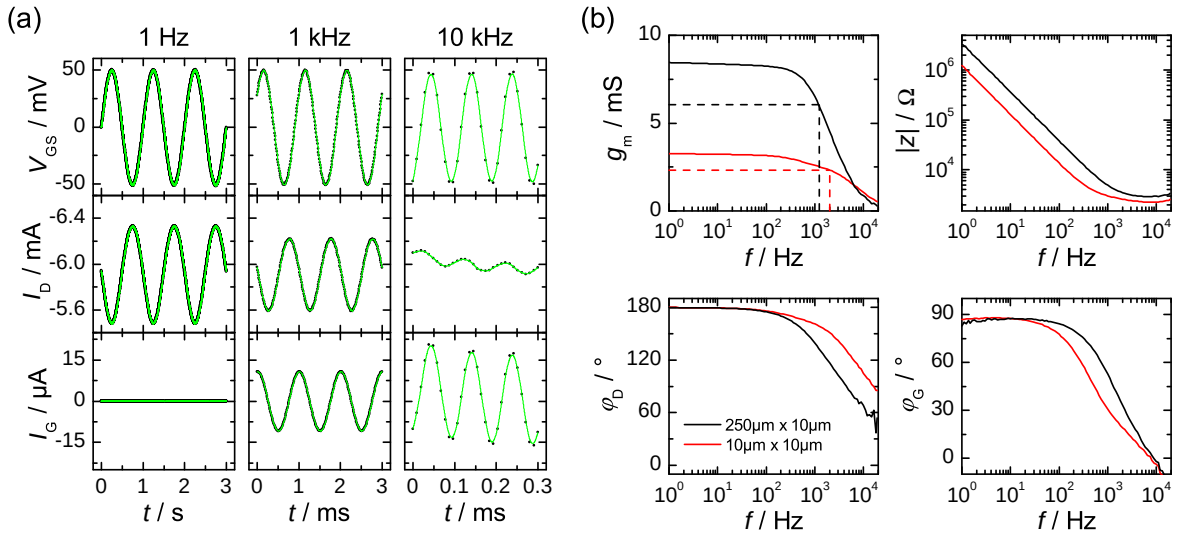

Figure 1.12: *(a) Transient behaviour of drain current and gate current upon application of a sinusodial gate voltage. The drain current modulation is high at low frequencies and low at high frequencies. For the gate current the opposite behaviour can be observed. The device geometry is $W = 250\,\mu m$, $L = 10\,\mu m$ and $d = 70\,nm$. (b) Calculated transconductance, absolute value of impedance and phase shift from the transient curves in (a) for two different device geometries. The volumetric capacitance of PEDOT:PSS allows for a higher transconductance at higher channel volumes. On the other hand, the cutoff frequency decreases with volume (dashed lines) and at the same time, the magnitude impedance scales with the area of the device channel. The channel thickness is $d = 70\,nm$.*

low voltage gate signal (see Figure 1.12a). While the drain current gives information about the frequency dependant transconductance of the device (Equation (1.12)), the gate current can be used to extract the impedance (Equation (1.8)). It can be seen that the drain current modulation is high at low frequencies, with practically no modulation at the gate current. In this regime, the ions have enough time equilibrate and form an EDL inside the polymer at each step of the voltage sweep. At higher frequencies, the drain current modulation starts to diminish while at the same time the gate current modulation starts to increase. The ions can no longer follow the applied voltage signal to a full extend and thus a transient current can be observed at the gate electrode. At very high frequencies, the drain current modulation is barely noticeable and only the transient gate current due to the permanent ionic flow in and out of the polymer can be detected. In this regime, the OECT is basically used as an electrode, much like as if one would short the source and drain contact. This means that both the transconductance, as well as the impedance decrease with increasing frequency. Whereas the impedance decreases linearly on a double logarithmic scale and allows for a better coupling of the gate electrode to the biological event at high frequencies, the transconductance is stable up until a certain *cutoff frequency*, after which it decreases rapidly, resulting in a poor

sensitivity of the OECT at high frequencies (see Figure 1.12b). The cutoff frequency is defined as a 3 dB decrease of the steady state transconductance value

$$f_{\text{cutoff}} = f\left(g_{\text{m}} = -3\,\text{dB}\right) = f\left(g_{\text{m}} \cdot \sqrt{1/2}\right) \quad . \tag{1.14}$$

In order to use the OECT for electrophysiological applications, the cutoff frequency needs to be above the expected bandwidth of the signal of interest. One can also think of using this behaviour as a first order low pass filter. The cutoff frequency depends on the device geometry and the design of the OECT can thus be used to tune the transient characteristics [Rivnay, 2015a]. However, a compromise has to be found between a high steady state transconductance and a high cutoff frequency, as the transconductance is directly proportional to the volume of the PEDOT:PSS channel and the cutoff frequency inversely scales with the volume. Additionally, the impedance scales with the area of the device. This becomes important for impedance based measurements, such as barrier integrity, and needs to be considered in the device design as well [Rivnay, 2015b].

1.2.3 Fabrication with Parylene-C Peel-Off Method

There are several ways to pattern conducting polymers and amongst the most interesting on an industrial scale are probably inkjet printing, screen printing or spray coating, due to their compatibility with roll-to-roll processing [Søndergaard, 2013]. Whereas these techniques pose their own challenges regarding ink formulation, stability or miniaturization, for academic purposes focussing on device physics a lithographic approach is more relevant due to an implementation with existing processing steps and the possibility for small feature sizes currently not possible with printing techniques. Any small clean room facility with a decent mask aligner can easily achieve feature sizes in the 10 µm range and depending on the equipment, this can go down to 10 nm as is the current standard in silicon MOSFET devices according to the "International Technology Roadmap for Semiconductors". A clean room is an environment with controlled humidity, temperature and with a defined maximum number of particles of a certain size. The clean room facility available for the work presented in this manuscript had a minimum level of 100 particles of 0.5 µm per cubic feet (i.e. no more than 3520 particles of 0.5 µm per cubic metre). The fabrication of an OECT can be broken down into two stages: first, the source, drain and gate contact as well as lead lines have to be defined, patterning a highly conductive material (see Figure 1.13). For PEDOT:PSS based devices, gold is the material of choice due to its low resistivity and a work function that lies slightly above the HOMO level of the conducting polymer. In a second stage, the conducting polymer will be patterned to bridge the source and drain contact and form the transistor channel. This can be done either directly (see Section 1.2.4) or

indirectly with a so called *peel-off technique* [DeFranco, 2006]. The various processing steps are as follows:

A first photolithography step is used to define the outline of the lead lines (see Figure 1.13a). After cleaning the substrate (in this case standard microscope glass slides) in an ultrasonic bath of an acetone:isopropanol solution (80:20), a photosensitive resist is spun cast onto the substrate at a certain angular velocity that defines the thickness of the resist coating (in the order of a few µm). A photoresist is comprised of three parts, the *resin* that is solid in an undiluted state, a *solvent* that allows for processability of the resin in a liquid state and a *photoactive compound* (PAC) that inhibits or promotes the dissolution of the resin in the developer. In order to achieve a homogeneous coating of photoresist on the substrate, the spin coater chamber is usually saturated with a solvent that will reduce the evaporation speed of the solvent in the photoresist during the spin coating step. During a subsequent soft bake (e.g. 1 min at 110 °C) the solvent can fully evaporate to leave only the solid resin/PAC mixture on the substrate. Depending on the exact chemical structure of the PAC one can distinguish between a *positive* and a *negative* photoresist. In a positive photoresist, the PAC decreases its intrinsic alkaline solubility by up to two orders of magnitude, meaning it inhibits the dissolution of the resin in a basic developer. Upon light exposure, the PAC gets converted into an acid and the exposed parts of the resin can then be dissolved in the developer. In a negative photoresist, the PAC will induce a cross-linking of the resin upon light exposure which renders the exposed parts insoluble in the developer. The photoresist used for the devices presented in this manuscript is called S1813, a positive photoresist with a basic developer called MF26A. In order to "engrave" the desired pattern into the photoresist, one uses a so called *mask aligner*, a tool that allows for a micrometer precise positioning of a photomask over the substrate. The photomask can be made out of anything that sufficiently absorbs light in the ultraviolet part of the spectrum. The industrial standard uses thin film chromium evaporated onto amorphous silica substrates, that allow for sub-µm resolution. However, such masks are rather expensive (typically 500 €) and for prototyping efforts where resolutions of down to 10 µm are sufficient, flexible masks with photographic emulsions are a suitable and affordable alternative. Here, a sub-mm thin polymeric film is coated with a photographic emulsion that after exposure and development becomes the contrast medium of the mask. After successful alignment of the mask with the substrate, the photoresist gets exposed to UV light at precisely the parts that are transparent in the photomask. The exposure dose, defined by the intensity of the UV lamp and the exposure time expressed in $\mathrm{mJ\,cm^{-2}}$, drives the chemical reaction in the PAC molecules and depends on the nature of the resist and its thickness. If the dose is too low, the near-substrate part of the photoresist is underexposed and will dissolve less, or not at all, in the developer. If it is too high, UV light will be scattered underneath the regions covered by the photomask, therefore enlarging the defined patterns. In order to find the optimal parameters for both expo-

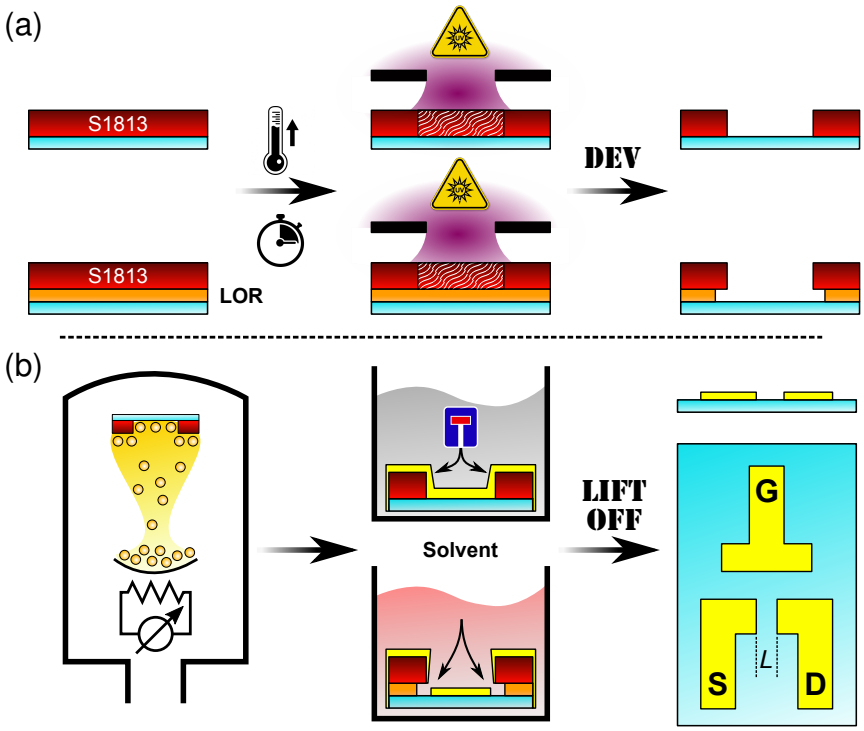

Figure 1.13: *(a) Photolithography steps with spincoating of positive photoresist, softbaking, exposure and development (from left to right). On the top is shown the procedure with simply the photoresist and on the bottom with an additional undercut layer (LOR). The exposure to UV light alters the chemical structure of the photoresist in a way that the resist gets soluble in the developer. A photomask defines the pattern. The undercut layer helps in the subsequent metal evaporation step. (b) Metal evaporation steps with the evaporation chamber, a lift-off bath in solvent and the final pattern (from left to right). In the evaporation chamber, the metal will be heated up through a resistive circuit until it reaches gaseous phase and subsequently condense on the substrate to form a uniform coating. The thickness is adjusted by the evaporation time. A solvent bath will dissolve the unexposed photoresist and remove the metal that has been evaporated on top. Without the undercut layer, the solvent has more difficulties to attack the resist. The undercut layer creates a gap in between the metal on the resist and on the substrate. The final pattern defines source, drain and gate contact, as well as the channel length L.*

sure dose and development time it is recommended to start with an exposure series, varying those parameters in a controlled manner, at the beginning of the process step. Once the photoresist has been developed, the substrate can be placed in the metal evaporation chamber.

The metal evaporation takes place in a high vacuum chamber (see Figure 1.13b). This will ensure that the metal particles can travel unhindered from the crucible to the substrate. With a high current running through the tungsten crucible, the metal is heated above it's melting temperature and starts evaporating. Following the second law of thermodynamics, the gaseous metal will make it's way to the substrate that is mounted upside down above the crucible. Due to the "colder" surface of the substrate, the metal will immediately condense and form a homogeneous layer. With low evaporation rates of the order of $0.1\,\text{Å}\,\text{s}^{-1}$ to $2\,\text{Å}\,\text{s}^{-1}$, the metal can be deposited atomic layer by atomic layer. It has been found that noble metals, such as pure gold, have a weak adhesion towards glass substrates, whereas metals with a high affinity towards oxygen can adhere much better due to the formation of an intermediate oxide layer [Benjamin, 1961]. Therefore, the first 10 nm deposited onto the glass substrate are made of chromium that shows very good adhesion properties and the remaining thickness of the film is made of gold (up to 150 nm). The metal alloy is coating the whole substrate, i.e. the photoresist as well as the exposed parts. To remove the excess metal after the evaporation, the photoresist needs to be dissolved in a solvent bath. Due to the step-like profile of the photoresist, the metal alloy will uniformly coat the whole structure making it difficult for the solvent to reach the "encapsulated" photoresist pattern. While with time and mechanical force (ultrasonic bath) it is still possible to get rid of the photoresist, a much easier solution is the addition of a so called *undercut layer* prior to the photoresist spin coating step. This undercut layer is insensitive to light and will be protected by the photoresist on top. As the photoresist is exposed and developed, also the undercut layer gets dissolved and with exact timing, a small undercut in the structure can be achieved (see Figure 1.13a). This µm thick gap between the photoresist and the substrate will ensure that the metal layer on the photoresist is disjoined from the one directly on the substrate. Therefore, the solvent can remove the bilayer resist more efficiently in a matter of less than an hour, instead of half a day when no undercut layer is used. As the metal that has been deposited onto the photoresist will be lifted off with the dissolution of the latter, one uses the term *lift-off* for this step. After the lift-off has been successful, one is left with the substrate and the patterned source, drain and gate contacts. The channel length of the transistor is being defined in this step as the distance between the source and the drain contact.

A vapor phase deposition of parylene-C is used to encapsulate and electrically isolate the lead lines and to pattern the conducting polymer (see Figure 1.14). Parylene-C (PaC), or poly(monochloro-para-xylylene), is a polymer that is traditionally used as hydrophobic diffusion barrier. With a low dielectric constant of around $\epsilon_\text{r} \approx 3$ this material exhibits low leakage currents, rendering it a good electrical insulator. The mechanical properties (tensile strength of about 70 MPa and yield strength of about 3 GPa) allow for the use of PaC as ultraflexible substrate and various applications are based on that approach [Sessolo, 2013; Fukuda, 2014; Williamson, 2015]. PaC

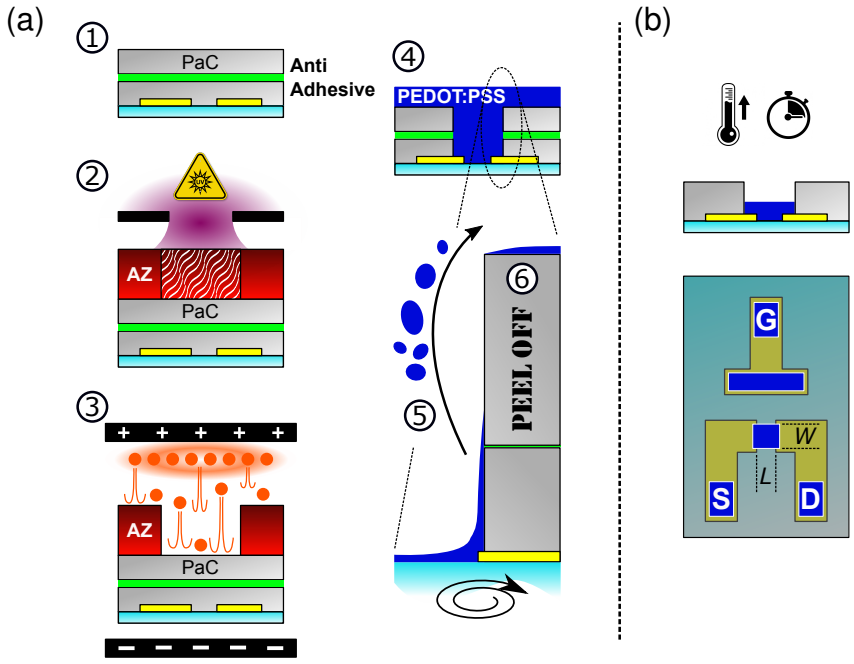

Figure 1.14: *(a) Patterning of conducting polymer with sacrificial layer peel-off technique. From top to bottom: parylene-C deposition of two layers with anti-adhesive layer in between (1), photolithography with positive thick resist AZ9620 (2), reactive ion etching to create an opening (well) in the PaC layers (3). A subsequent spin coating step with PEDOT:PSS will coat the PaC and fill the well (4). A zoom-in emphasizes the scale of the* 4 µm *thick double layer PaC versus* 100 nm *PEDOT:PSS. Upon spinning, most of the PEDOT:PSS solution will be hurled out of the PaC well (5). Peeling off the outermost sacrificial PaC layer will remove the excess PEDOT:PSS (6). (b) Final structure of the peeled-off device. The gold lines are isolated with the remaining PaC layer. After hard baking, the PEDOT:PSS will form a rigid stable layer. It bridges the source and drain contact to form the transistor channel. Due to the peel-off technique, also the gate and the contact pads will be coated with the polymer.*

is deposited in a high vacuum chamber at about 10 Pa to 100 Pa. A granular dimer raw material is heated to about 175 °C, upon which the dimer is vaporized. Running through a pyrolysis tube at about 690 °C, the dimer gets cleaved into a monomeric form. In the deposition chamber, kept at room temperature, the monomer gas deposits on the substrate as a thin, transparent polymer film.

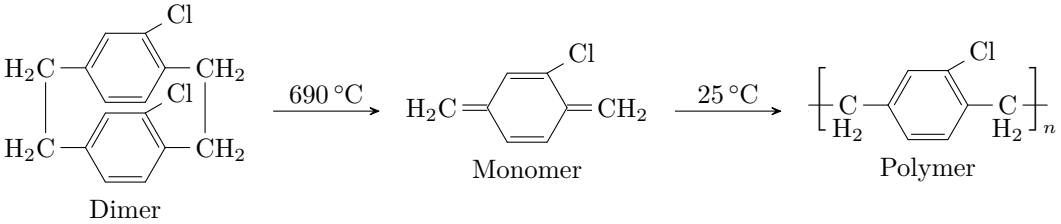

The thickness of the film is controlled by the amount of raw dimer material loaded into the deposition machine. To achieve a better stability of the PaC layer, a small amount of silane A-174 (3-(trimethoxysilyl)propyl methacrylate) is added to the deposition chamber and will chemically attach to the surface which facilitates the adhesion of PaC on the glass substrate and the gold contact lines. A first layer of about 1.5 µm will serve as an isolation layer. A second layer of about 2.5 µm is used as a sacrificial layer, i.e. the layer will be patterned to create openings, coated with PEDOT:PSS and mechanically removed to peel off the PEDOT:PSS in the unpatterned parts. On a standard glass substrate, the PaC layer would detach upon soaking in DI water without any additional treatment. But PaC on PaC is more likely to adhere and therefore an anti-adhesive layer needs to be used in between the two PaC layers. The material used as anti-adhesive layer is a detergent (Micro90 soap) and can be spin coated onto the PaC coated substrate in a 1 % to 2 % dilution. After a quick soft bake to evaporate the water, it will form a thin uniform coating and the sacrificial layer will adhere well enough to allow for further processing steps, but can be removed mechanically or by soaking in DI water.

A second lithography step and subsequent dry etching will pattern the PaC double layer. The idea is to create openings in the PaC double layer so that a coating with PEDOT:PSS will allow the conducting polymer to reach the substrate surface and the gold contacts. Every part, that needs to be accessible in the final device (i.e. contact pads, gate electrode and transistor channel) needs to be defined during this step. For this, a thick photoresist is needed in order to protect the PaC double layer in the subsequent dry etching step at the parts that need to stay. AZ9260 is a positive photoresist suitable for film thicknesses from 5 µm to 20 µm and allows for high resolution patterning. The patterning procedure is the same as for the first lithography step with much longer exposure and development times due to the increased thickness. After the desired features are successfully transferred to the photoresist, the whole structure (substrate, gold, double layer PaC, AZ photoresist) is placed into a *reactive ion etching* chamber. In a high vacuum environment, a plasma is generated by ionizing a gas mixture of in this case O_2 and CHF_3 through magnetic induction. This chemically reactive plasma is then accelerated towards the substrate through an electric field, where it will physically and chemically remove atomic particles layer by layer. The plasma will attack both, the photoresist as well as the PaC double layer. As soon as the PaC is fully removed and the glass substrate and gold contacts are exposed to the plasma beam, the etching process has to be stopped as an over-etching would also remove the gold from the substrate. After the etching step, the unexposed photoresist can be removed in an acetone bath. This step is optional, as the photoresist will also be removed when peeling off the sacrificial layer, but generally, there is also photoresist on the edge of the glass substrate that might have an impact on the biocompatibility of the final device.

The PEDOT:PSS coating step is done using a spin-coater. For this, a solution is produced according to the formula presented in Table 1.1. If PEDOT:PSS is coated directly after the dry etching step, no additional steps need to be considered, as there will be already hydroxyl group present on the surface due to the plasma treatment. The hydroxyl groups will form a chemical bond with the GOPS present in the PEDOT:PSS solution and therefore improve the adhesion of the conducting polymer layer. Additionally, the hydroxyl groups alter the surface energy and render the substrate more hydrophilic which increases the wettability of the substrate and facilitates the spin coating. If the substrate has been exposed to ambient air conditions for a longer time (more than 30 min to 1 h), water will adsorb on the surface removing the hydroxyl groups. Therefore, a quick oxygen plasma with low power is needed to re-induce those hydroxyl groups. The thickness of the conducting polymer layer can be controlled to some extend by adjusting the rotational speed of the spin coating process. However, this is not comparable with coating a bare substrate, such as a glass slide or silicon wafer. The PEDOT:PSS solution needs to enter the opening in the PaC double layer, which can be seen as a well (see Figure 1.14). When the substrate is coated with PEDOT:PSS, this well will be filled fully. During the spincoating (step 1), part of the solution will be projected out of the well due to centripetal forces and the remaining solution will be smeared out inside the well and partly cover also the walls of the well, resulting in a thin film coating. A quick soft baking step ensures that the PEDOT:PSS solution is stable enough for the peel-off process, but not yet fully cross-linked as this would rupture the film during the peel-off. It has been found that an initial thin film of PEDOT:PSS (3500 rpm for about 70 nm) and several additional slower spin coatings (650 rpm) provide a more homogeneous film than one spin coating step at very slow rotational speeds, when thick PEDOT:PSS coatings are needed. With a scotch tape, the sacrificial PaC layer can be carefully peeled off (step 2), taking with it the excess PEDOT:PSS and leaving a thin film of the conducting polymer only on the exposed parts of the substrate and gold contacts. The final structure needs to be cured at about 120 °C for about 1 h to ensure a full cross-linking of the GOPS in the PEDOT:PSS solution and the device is ready to use.

1.2.4 Direct Lithographic Patterning of Conducting Polymers

The peel-off process described above has been developed because regular photolithographic patterning would necessitate exposure of the conducting polymer to harsh chemicals such as photoresists or developers during the process. Instead of first spin coating the conducting polymer and then performing all necessary steps (subtractive patterning), the PaC peel-off process allows the implementation of the conducting polymer at the very last processing step (additive patterning), ensuring that the delicate material remains functional (see Figure 1.15a). However, despite the ease and utility of PaC peel-off patterning, this process lacks one fundamental demand for industrial

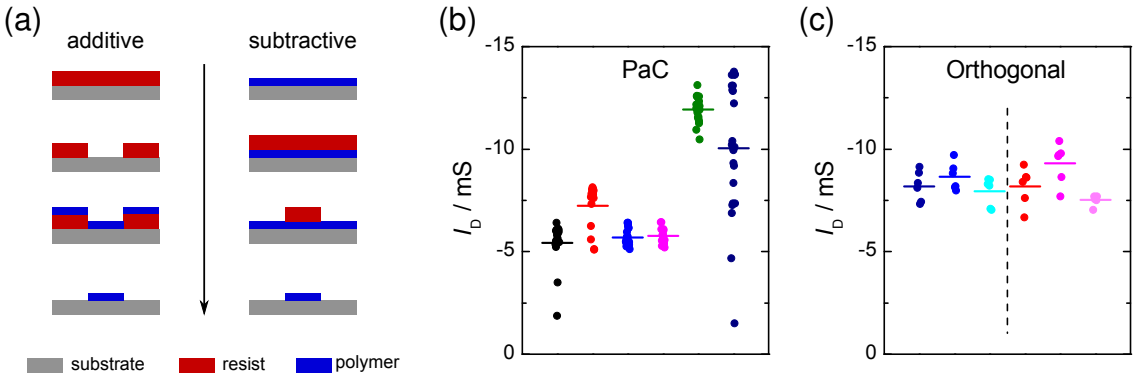

Figure 1.15: *(a) Difference between additive and subtractive patterning. For additive patterning, the conducting polymer is spuncast only at the very last step. For subtractive patterning, the conducting polymer is spincast first and exposed to both resist, developer and eventually stripper. (b) Drain current at* $V_{DS} = -0.6\,\mathrm{V}$ *and* $V_{GS} = 0\,\mathrm{V}$ *as an indicator for device homogeneity of OECTs fabricated with PaC peel-off technique. The device geometry is* $W = 100\,\mu\mathrm{m}$, $L = 10\,\mu\mathrm{m}$ *and* $d \approx 100\,\mathrm{nm}$. *24 devices per glass slide, 6 glass slides, all fabricated during the same batch. (c) Similar data at same bias point for 6 devices per glass slide, 3 glass slides per batch, two different batches, fabricated with Orthogonal Inc. resist. The device geometry is kept the same. The mean value is indicate as horizontal bar.*

application and this is device homogeneity. The very nature of this process, where the conducting polymer solution has to enter a micron sized opening in the PaC double layer and be thinned down to about 100 nm with spincoating, is not well defined. Depending on the position of the opening with respect to the spin center, the centripetal forces vary. The conducting polymer solution gets smeared out on the walls of the opening and during peel-off might get ruptured as there may not be a separation between the layer on top of PaC and the layer inside the opening. Depending on how far the conducting polymer gets smeared out, the device geometry changes.

In Figure 1.15b, one can see a statistical study of the device homogeneity for OECTs fabricated with the PaC peel-off technique. Here, the drain current at a defined bias point is plotted for several devices on the same glass slide and for several glass slides within the same batch. Even though, this bias point reflects only a tiny portion of the whole output characteristics of the devices, it can give an estimate about the homogeneity. For absolutely identical transistors, the drain current should be equal at equal bias points. It can be seen that even though a good device homogeneity can be achieved occasionally throughout the same glass slide, the majority of times the devices show a huge discrepancy in their output characteristics. Furthermore, the mean values vary from glass slide to glass slide even within the same batch. This can be probably attributed to different channel thickness, as the thickness depends on how much of the conducting polymer remains inside the openings of the double PaC layer during the

spincoating step.

This shows the need for a more reliable patterning approach. In Figure 1.15c, one can see a similar set of data for OECTs fabricated with a subtractive method using photoresist from Orthogonal Inc. especially designed not to harm organic materials. Even though this study contains less devices per glass slide and also a different photomask layout has been used, it is evident that the slide to slide and batch to batch homogeneity is much higher. A more comparative study with equal fabrication layout for both processes can be found in Chapter 4 and shows similar findings. As with this method, the conducting polymer is spuncast onto the full glass slide, very homogeneous coatings can be achieved, only limited by edge effects. This allows for devices with the same channel thickness throughout the whole batch.

The Orthogonal Inc. materials are based on hydrofluoroether (HFE) solvents that are "orthogonal" to nonfluorinated organic materials. Here, orthogonal means that the organic material is insoluable and does not swell in HFEs. In addition, most HFEs have been evaluated as non-toxic and environmentally friendly [Tsai, 2005]. A HFE compatible photoresist has been designed by copolymerizing a highly fluorinated monomer with a photolabile monomer, that upon UV irradiation would switch solubility in HFE solvents [Taylor, 2009]:

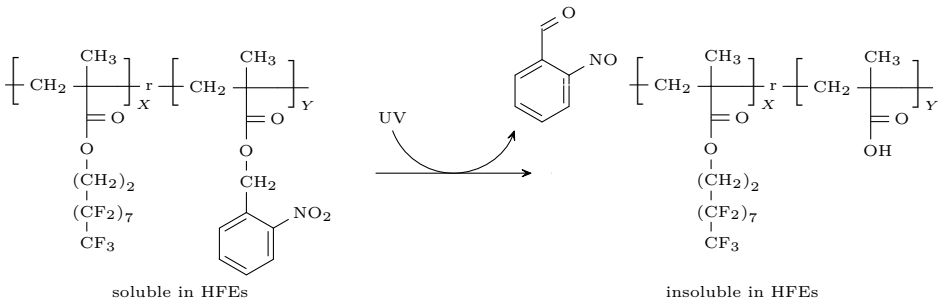

Such a material, especially designed for acidic organic materials, such as PEDOT:PSS, has been successfully used for submicron feature sized patterning of various organic semiconductors. The processing steps are as follows:

The definition of metal lead lines is identical to the PaC peel-off method described above, up until after the metal lift-off. Again, about 10 nm chromium and 150 nm gold are deposited via thermal evaporation.

For the coating of the conducting polymer, the same formula of PEDOT:PSS solution is used as for the PaC peel-off process. The material is again spuncast onto the substrate and immediately cured at 125 °C for about one hour. This ensure a homogeneous coating of the film over the whole substrate. As here, the thickness of the coating is directly set by the spin speed and not indirectly by the amount of solution

that remains in the openings, as is the case for the PaC peel-off method, less spin speed is needed to obtain similar thicknesses. It has been found that a spin speed of 1500 rpm yields a film thickness of about 100 nm on standard microscope glass slides as substrate (compared to 3500 rpm with PaC peel-off method).

The orthogonal photoresist, used for the second photolithography step, is called "OSCoR 5001" provided by Orthogonal Inc. and has an etch rate of 700 nm min^{-1} to 900 nm min^{-1} under standard RIE conditions. Due to the GOPS crosslinking of the PEDOT:PSS film, the etch rate of the later is much lower than the etch rate of the photoresist. Even though a detailed study for this is missing, a personal estimate would be that about 90 s are needed to fully remove the 100 nm PEDOT:PSS film, yielding an etch rate of about 70 nm min^{-1}. Therefore, in order to protect the organic layer in the subsequent etching step, a thickness of the photoresist of about 1200 nm should be sufficient. This can be achieved with a spinspeed of 1200 rpm for 35 s. A soft-baking step at 65 °C for 60 s and subsequent exposure to UV light at 365 nm with a dose of about 65 mJ cm^2 defines the patterns that one wants to transfer to the conducting polymer. As the OSCoR 5001 is a negative photoresist, a post-exposure bake is necessary to fully drive the acid-initiated chemical reaction that induces the solubility switching. Without this post-exposure bake (90 °C for 60 s), all the photoresist coating would be dissolved in the basic developer. After the post-exposure bake, the developer (simply called "Developer 100" by Orthogonal Inc.) can be applied either by dipping the substrate in a bath or, more economically, via a *double-puddle* method. Here, the substrate is place on a spin coater and fully coated with the developer. After a wait time of in this case 25 s, the developer is spun off the surface at high spin speed. This step is repeated once to ensure the proper dissolution of the unexposed photoresist. An image of the developed PEDOT:PSS channel of an OECT can be seen in Figure 1.16a.

The etching process is similar to the PaC peel-off method described above, the difference being that in this case the conducting polymer is directly removed at the unexposed parts. As stated above, an etching time of 90 s with an oxygen plasma at 150 W with $O_2 = 50$ sccm and $CHF_3 = 5$ sccm has been found optimal for the removal of the PEDOT:PSS coating. After the etching, the remaining photoresist at the exposed parts needs to be removed. This is called "stripping" and the latest iteration of Orthogonal Inc. for the solvent used in this process is called "Stripper 903". It certainly contains HFEs but the exact formulation is corporate secret. The stripping is done again with a double-puddle method with a dissolution time of 2×60 s. Even though this step seems trivial, it has been found that residues of photoresist can remain on the conducting polymer, particularly at the center of the glass slide (see Figure 1.16b). The reason for this is unclear as the stripper should in principle dissolve all the remaining photoresist. However, it looks like the stripper only partially dissolves the resist and the centripetal

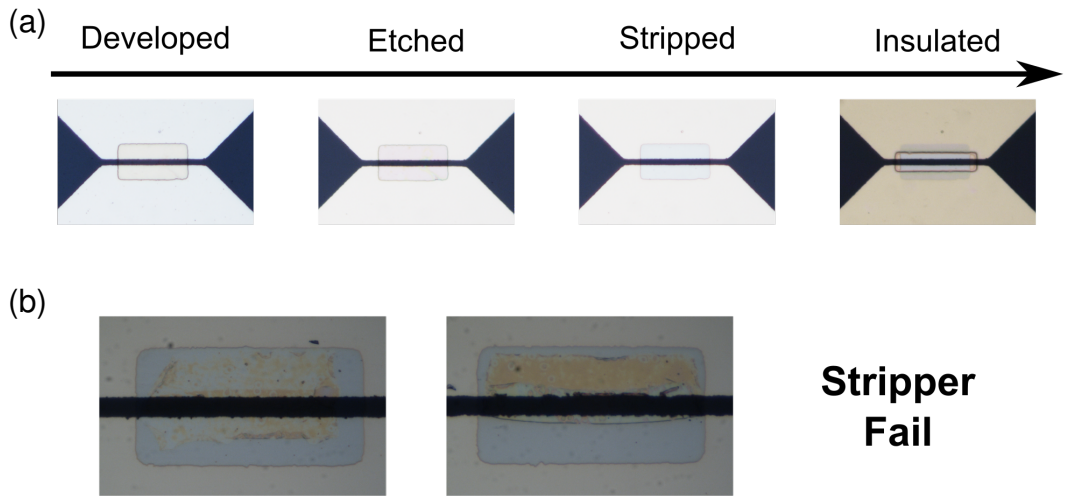

Figure 1.16: *(a) Microscope images of a PEDOT:PSS channel (square at the center) on source and drain contacts (bright trapezoids) at different processing steps. After the development, a rectangular pattern of photoresist can be seen on a homogeneous PEDOT:PSS layer. After etching, PEDOT:PSS remains only underneath the photoresist and the gold contacts are exposed to air. A clear outline of the PEDOT:PSS channel can still be seen. After stripping, the PEDOT:PSS channel is barely visible. The insulation layer protects the gold contacts from exposure to water and only the PEDOT:PSS channel can be accessed by the ions. (b) Zoomed microscope images of PEDOT:PSS channel with photoresist residues after stripping. This happens mainly at the center of the substrate. The channel size is* $W = 100\,\text{nm}$ *and* $L = 10\,\text{nm}$.

forces during spin coating of the puddle method mechanically remove the residues. As the centripetal forces are very small at the center of the glass slide, the photoresist residues cannot be hurled away at that part of the substrate. Furthermore, this suggested explanation is supported by the fact that a prolonged stripper bath does not help in getting rid of the residues. It can be, that the resist gets partially altered during the etching process. Maybe it is thinned down too much. But it may as well be any other processing step that is not yet optimized. Due to lack of time, this issue could not be fully resolved. There were even batches, where this problem would not occur at all. But if it happened, the concerned devices could not be used, as the residues would act as a barrier for the ions during the gating of the OECT.

For the passivation of the metallic lead lines, another negative orthogonal resist is used, called "OSCoR DE1" (for dielectric). This particular resist allows for low defect coatings over a range of film thickness, has been tested for its biocompatibility and provides an excellent electrical insulation. The resist is patterned in the same way as OSCoR 5001, i.e. spincasting (2000 rpm for 60 s), softbake (90 °C for 60 s), exposure

(365 nm at 149 mJ cm^{-2}), post-exposure bake (90 °C for 60 s) and development (Developer 100, double puddle 2 × 45 s). An image of the channel with the passivation layer can be seen in Figure 1.16a. In order to ensure a proper alignment of the opening in the passivation layer and the PEDOT:PSS channel, an overlap of about 10 µm is used in the mask design. Whereas this increases the volume of the PEDOT:PSS channel exposed to an ion uptake, the effective channel length is still given by the distance between source and drain contact.

1.3 Sensor Circuits Using OECTs

A Wheatstone bridge is a basic electrical circuit that has been invented by Samuel H. Christie in 1833. However, it was Sir Charles Wheatstone, who could fully understand and accurately describe the circuit using Ohms law and therefore, the credit goes to him and the bridge bares his name [Ekelof, 2001]. This simple and elegant circuit is comprised of four resistive elements, arranged in a loop with a voltage or current source between the upper and lower connection points and a voltage probe between the remaining two points.

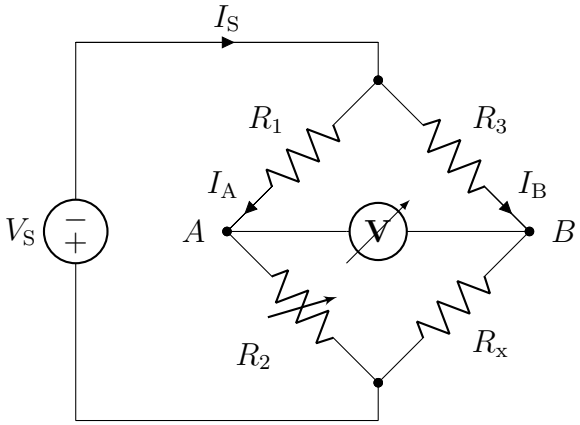

When a voltage V_S is applied to the system, a current I_S gets divided into the two branches of the bridge depending on the ratio between the total resistance of each branch. The voltage building up between the floating voltage points A and B of each branch can be calculated using Kirchhoff's circuit laws

$$(i) \quad V_S = I_A \cdot (R_1 + R_2) \quad (ii) \quad A = I_A \cdot R_1 \quad \rightarrow \quad A = V_S \cdot \frac{R_1}{R_1 + R_2} \tag{1.15}$$

$$(i) \quad V_S = I_B \cdot (R_3 + R_x) \quad (ii) \quad B = I_B \cdot R_3 \quad \rightarrow \quad B = V_S \cdot \frac{R_3}{R_3 + R_x} \tag{1.16}$$

By adjusting one resistive element (for example R_2), one could tune the floating voltage points A and B to be identical. At this so called *balance point* a clear relationship

between the resistive elements of the bridge can be obtained

$$\frac{R_1}{R_1 + R_2} = \frac{R_3}{R_3 + R_\mathrm{x}} \quad \rightarrow \quad \frac{R_2}{R_1} = \frac{R_\mathrm{x}}{R_3} \tag{1.17}$$

Therefore, by knowing the values of R_1 and R_3 and adjusting R_2 to balance the bridge, one can calculate the value of R_x with great precision. The advantage of this so called *null method* is that one does not need to know the mode of the source (current or voltage), the magnitude of the source, the mode of the probe (current or voltage) or the impedance of the probe. In fact, this method even works with highly unstable power sources. The only thing one needs to do is accurately detect a zero current in between the two branches. Therefore, this method has been widely used as calibration method for resistors.

Basically, the bridge is a reference based circuit, that compares the resistance ratio of each branch with one another. In many cases, the accurate detection of an unknown resistance can be used to measure a physical phenomenon. For example, it is known that the resistivity ρ of a metal conductor depends on temperature. At higher temperatures the atoms inside the conductor material tend to vibrate more and therefore, electrons running through the conductor get scattered more often. This leads to a reduction of the electron mobility and therefore and increase in the resistivity. For small temperature changes ΔT, this behaviour is linear

$$\rho = \rho_0 \left(1 + \alpha \left(T - T_0\right)\right) \quad , \tag{1.18}$$

where ρ_0 is the resistivity at a defined temperature T_0 and α is the temperature coefficient. Therefore, by accurately measuring the resistance, the Wheatstone bridge circuit can be used as temperature sensor. Many other physical parameters induce a change in resistivity of a given material, such as strain, pressure, light or humidity and therefore many different sensors can be build with a Wheatstone bridge circuit.

However, with the null method one would need to constantly readjust one of the resistive elements in order to balance the bridge and be able to calculate the unknown resistance. This is not only tedious but also very impracticable. In most sensing applications, one would actually measure the output voltage between the two floating points and calculate the change in resistance accordingly. Typical sensor layouts are shown in Figure 1.17. In case one there is only one varying resistive element and it can be seen that the output voltage depends non-linearly on the change in resistance ΔR. This non-linearity can be calculated and gives an end-point linearity error of approximately $0.5\,\%\,\%^{-1}$. For example, for a change in resistance of $\Delta R = 0.1\,\% \cdot R$ the output voltage would be $0.05\,\%$ less than if a linear dependency would be assumed

$$V_\mathrm{out} \approx \underbrace{\left[\frac{V_\mathrm{S}}{4} \cdot 0.1\,\%\right]}_{\text{linear part}} \cdot \underbrace{(1 - 0.05\,\%)}_{\text{non-linear error}} \quad . \tag{1.19}$$

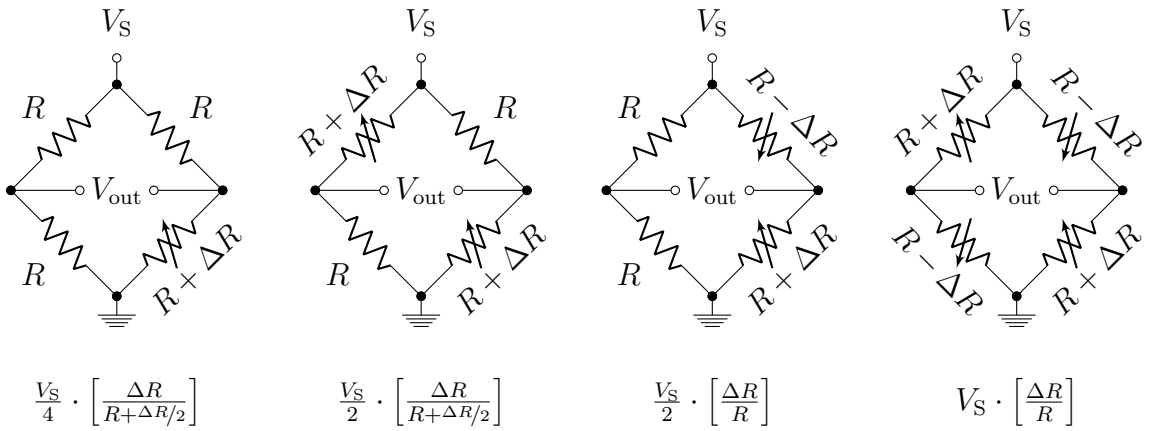

Figure 1.17: *Output voltage for Wheatstone bridge circuit with different varying elements and corresponding output voltage.*

It can be seen that the output voltage is proportional to one quarter of the supply voltage. This can be further enhanced by implementing a second identical varying resistive element at the opposite side of the bridge, as shown in the second case. Here, the output voltage is twice as sensitive as for a single varying element bridge circuit. Such a layout is often used for pressure sensors, where two identical strain gages are mounted with their axes in parallel. However, the end-point linearity error remains the same. This is obvious as in both cases, the single varying element bridge and the two-element varying bridge the change in resistivity goes only in one direction. In order to balance this non-linearity, a resistive element with a change in the opposite direction is needed, such as shown in the third case. Such an element could be for example a thermistor with a negative temperature coefficient that actually increases conductivity with increasing temperature. Also inorganic semiconductors exhibit such a behaviour where the conductivity depends exponentially on the temperature as more and more charge carriers get excited into the conduction band. For such a two-element varying bridge, the output voltage is proportional to one half of the supply voltage, due to the resistivity change of two of the resistive elements. Moreover, the dependency is linear with the change in resistivity. Therefore, such sensors can be easily calibrated and show a high reliability. To increase the sensitivity even further, the branch that contains the varying elements can be mirrored, as can be seen in the fourth case. The calculation shows that here the output voltage is directly proportional to the supply voltage multiplied with a percentage-wise change in resistivity. Such a layout is an industrial standard for load cells, where four identical strain gages are used to provide a signal that is directly proportional to the applied force. Recently, also a flexible, inkjet-printed temperature sensor based on organic materials has been demonstrated using exactly this bridge layout. The sensor showed very good linearity and little hysteresis within a temperature range of 20 °C to 70 °C [Bali, 2016].

1.3.1 Series circuit of OECT and resistor

Up until now, only purely resistive elements have been discussed in their various bridge configurations. However, the aim of this thesis is to implement the OECT into such simple circuit layouts. In a simple picture, a transistor can be viewed as a conductor for which the conductivity can be controlled through a gate voltage. Therefore, the OECT can also be implemented into a Wheatstone bridge circuit to provide a sensor element which is now sensitive to changes in the gate voltage, rather than temperature, pressure or other parameters. Other than a purely resistive element, the conductivity state of a transistor is not only controlled by a gate voltage but also determined by the source drain voltage. And here comes the difficulty when implementing an OECT (or any kind of transistor) with other circuit elements: the source drain bias is not fixed anymore but floating. For the simple case of a resistor in series with an OECT, one can immediately see that effect.

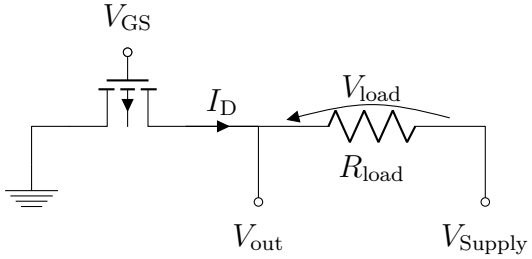

Here, the floating voltage point V_{out}, is both the probe point as well as the effective source drain bias of the transistor. This floating voltage depends on the current I_D that is running through both the transistor and the resistor (here called drain load)

$$V_{out} = V_{Supply} - V_{load} = V_{Supply} - I_D \cdot R_{load} \quad . \tag{1.20}$$

And here comes the sensing mechanism: the drain current can be modulated via the gate voltage and V_{out} will change accordingly. For example, if a negative voltage is applied to a PEDOT:PSS based OECT, the conducting polymer gets reduced and the drain current gets smaller in amplitude. Therefore, the output voltage will increase, as the voltage drop across the drain load will decrease. This, in turn, will increase the drain current, as the transistor experiences a higher effective source drain bias and therefore, the two counterbalancing effects will lead to an equilibrium output voltage, the so called *operation point*, that for a given gate voltage is determined by the supply voltage, the drain load and the geometry of the transistor.

If an analytical model exists for the transistor, the gate dependency of the output voltage can be calculated. This will be shown in Chapter 3 in more detail. Otherwise, the operation point can be extracted graphically (or numerically) by plotting both the output curve of the transistor and the so called *load line* that can be obtained by solving

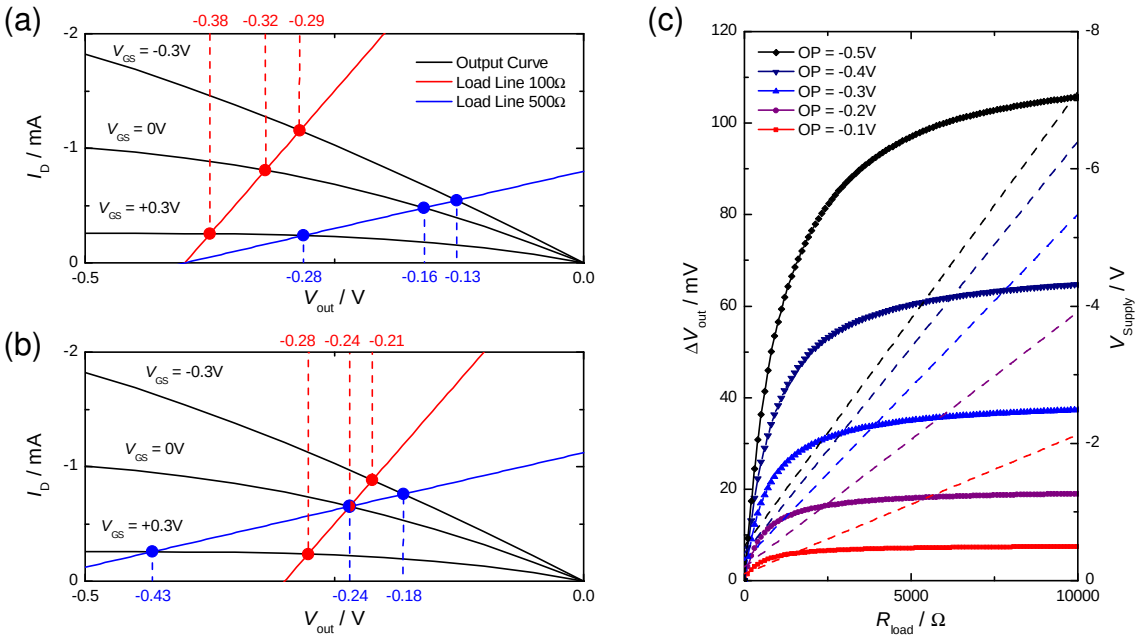

Figure 1.18: *(a) Load line diagram for two different drain load values. The OECT geometry is* $W = 50\,\mu m$, $L = 25\,\mu m$ *and* $d = 90\,nm$. *The supply voltage is for both cases set to* $V_{Supply} = -0.4\,V$. *The gain of the system is larger for higher drain load values and positive gate voltages. For negative gate voltages, the gain remains the same. (b) Same graph but for different supply voltages in order to achieve an operation point of* $V_{out} = -0.24\,V$ *at* $V_{GS} = 0\,V$ *for both drain load values (*$V_{Supply} = -0.3\,V$, $R_{load} = 100\,\Omega$ *and* $V_{Supply} = -0.56\,V$, $R_{load} = 500\,\Omega$*). Even though the supply voltage has to be higher, the gain of the system is much higher at higher drain load values. (c) Output voltage change (left y-axis) for a small excitation signal of* $V_{GS} = -50\,mV$ *at different operation points for increasing drain load. Here, operation point means the point at* $V_{GS} = 0\,V$. *The dashed lines show the supply voltage that is needed to achieve the set operation point (right y-axis).*

Equation (1.20) for the current

$$I_D = \frac{V_{Supply} - V_{out}}{R_{load}} \quad , \tag{1.21}$$

into the same graph. The intersection of the two curves gives the operation point. This can be seen in Figure 1.18a. Note that here the source drain voltage of the transistor is denoted with V_{out}. It can be seen that the operation point depends on the magnitude of the drain load, the supply voltage and clearly also on the gate voltage. When the gate voltage is changed, the output curve of the transistor is altered and the operation point moves along the load line. For positive gate voltages, the operation point moves towards higher voltages and for negative gate voltages it moves to lower voltages. This means that a positive gate signal will increase the output voltage and

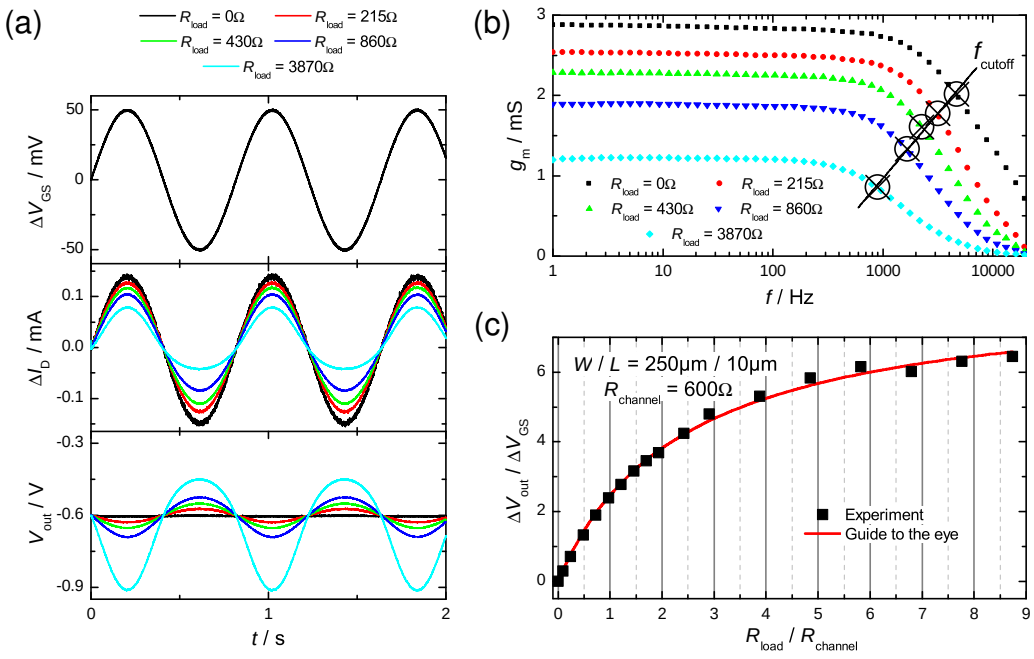

Figure 1.19: *(a) Raw data of frequency sweep with a* 50 mV *excitation signal at* 1.2 Hz *for different drain load resistors. The operation point at* $V_{GS} = 0\,\mathrm{V}$ *is set to* $-0.6\,\mathrm{V}$*. At higher drain load the output signal shows an asymmetric behaviour with a distorted sinus curve. (b) Frequency sweep for different drain load. Both the transconductance and the cutoff frequency get smaller with higher drain load. (c) Gain versus drain load extracted from the raw data. The same saturation can be seen at higher drain load as in Figure 1.18b.*

vice versa. Furthermore, the slope of the load line depends on the magnitude of the drain load. The higher the drain load, the weaker the slope. At the same time, the operation point gets shifted towards lower voltages for higher drain load if the supply voltage remains the same. It can be seen that the difference between operation points at different gate voltages, i.e. the gain of the system $\Delta V_{\mathrm{out}}/\Delta V_{\mathrm{GS}}$ (which is actually the sensing output) does not change significantly for positive gate voltages. However, the change at negative gate voltages is much bigger at higher drain load, even though the absolute value of the operation points are smaller.

The effect of changing the supply voltage is shown in Figure 1.18b. If the supply voltage is chosen to provide a particular operation point at $V_{\mathrm{GS}} = 0\,\mathrm{V}$, a direct comparison between the gate voltage dependency for different drain load resistors can be made. It is evident, that the gain is higher at higher drain load, where again the positive gate voltages show a more pronounced effect. The largest gain can be obtained in the saturation regime of the transistor. In this regime, the output curves at different gate voltages run parallel to each other and therefore, a weaker slope in the load line leads to operation points that get more and more separated on the x-axis. This however

comes at the cost of a higher supply voltage that increases linearly with the magnitude of the drain load resistor

$$\frac{\partial V_{\mathrm{Supply}}}{\partial R_{\mathrm{load}}} = I_{\mathrm{D}} \quad . \tag{1.22}$$

This can be seen in Figure 1.18c, where the change in output voltage for a small excitation signal of $V_{\mathrm{GS}} = -50\,\mathrm{mV}$ is plotted against the drain load. An actual amplification, where the output signal changes are bigger than the gate voltage excitation, can only be obtained for higher operation points. Note that the gain seems to saturate at higher drain load. This can be explained with the fact that the slope of the load line can at most be equal to zero and at that point the two adjacent output curves will have a defined distance in the linear regime. It can be shown, that in the saturation regime and for small excitation signals, the gain does not saturate but instead scales linearly with the drain load. This will be explained in more detail in Section 3.5.

From Figure 1.18a-b, one can already see that the output voltage deviates more and more from a linear behaviour at large gate voltages. This will become more clear by looking at the transient behaviour of the transistor plus resistor system (see Figure 1.19). Here, a sinusoidal excitation signal of 50 mV leads to a transient change in the drain current that can be read out at the output voltage. As can be seen, the amplitude of the drain current signal shows an asymmetric behaviour for a symmetric excitation signal. At negative gate voltages, the drain current flattens out more pronounced as for positive gate voltages where the drain current shows a regular sinusodial behaviour. This is again due to the effect that at negative gate voltage, the operation point of the transistor moves back into the linear regime whereas for positive gate voltages the operation point is moved further into the saturation regime. According to the load line method, this means that the change in drain current for a change in gate voltage is less pronounced at negative gate voltages than positive gate voltages. This behaviour gets translated into the output voltages, which is proportional to the drain current and the drain load resistor. The transconductance, defined as the change in amplitude $^{\Delta I_{\mathrm{D}}}/_{\Delta V_{\mathrm{GS}}}$, gets smaller with increasing drain load. Also the cutoff frequency shows the same trend. This shows that care needs to be taken when choosing the appropriate drain load and supply voltage. Since the source drain bias of the transistor is not fixed anymore, the system is not as straight forward. A more detailed description follows in Chapter 3.

1.3.2 OECT implemented in Wheatstone Bridge

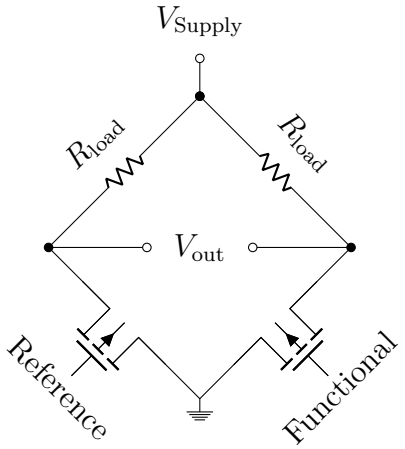

The above findings can be directly implemented to the Wheatstone bridge circuit, as this is merely a duplication of the single OECT plus resistor system. The advantage of using OECTs as the varying resistive elements in the bridge circuit is that a reference based sensor system can be achieved. This means that by having two identical OECTs in both branches of the bridge, the difference between the two transistors will be directly reflected in the output voltage. This difference can either be a simple gate voltage difference, or more relevant for biosensing applications, one of the OECTs can be functionalized and then the other OECT acts as a reference. To facilitate the readout, equal drain load resistors will be used for both branches. This ensures an equal amplification for both OECTs. In order to avoid electrical cross-talk between the two OECTs, separate electrolytes have to be used for each branch. Initially, when both transistors are gated equally, the output voltage will be zero as the current is split equally into both branches of the bridge. As soon as the functional transistor picks up a biological event and therefore changes its conductivity state, the output voltage will change accordingly. Due to the reference OECT, the baseline of the OECT, i.e. the drain current at zero gate bias, will be removed and changes in the output voltage can be directly correlated with changes in the drain current. Additionally, due to this reference based sensing mechanism, any drift in the drain current will be filtered, as it occurs at both OECTs. Such a drift is usually seen due to evaporation of the electrolyte or temperature fluctuations. But also changes in the electrolyte composition that do not involve the biorecognition element will be removed if one ensures that both OECTs are gated through an equal electrolyte. A detailed description of a biosensing application will be presented in Chapter 4.

Here, the focus lies on the general working principle. This can be demonstrated very easily by keeping the gate of one OECT stable and varying the gate of the second (see Figure 1.20). The gate voltage was modified stepwise from 0 mV to 100 mV in steps

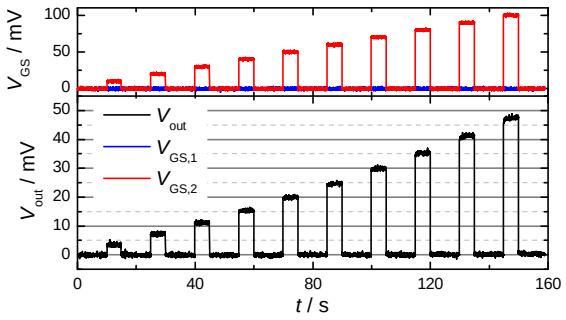

Figure 1.20: *Output voltage of the bridge upon varying the gate of only one OECT. The OECT channel was* $W = 100\,\mu m$, $L = 10\,\mu m$ *and* $d = 100\,nm$. *The resistance of the channel at* $V_{GS} = 0\,V$ *was* $100\,\Omega$ *and the drain load resistors where chosen to be also* $100\,\Omega$ *each. The supply voltage was* $V_{Supply} = -0.6\,V$ *to provide an operation point of each OECT at* $V_{GS} = 0\,V$ *of* $-0.3\,V$.

of 10 mV and it can be seen that the output voltage follows the input almost linearly up until gate voltages of 70 mV with a factor of $\Delta V_{out}/\Delta V_{GS} = 0.5$. The attenuation of the input signal, instead of an amplification, has to do with the low drain load that has been set to be as high as the channel resistance to ensure a linear behaviour. Nevertheless, it can be seen that the output voltage always jumps back to zero as soon as both transistors are gated equally. Furthermore, the baseline of the output signal is very stable due to the reference based measurement.

Such a Wheatstone bridge circuit, using two OECTs for reference based measurements has been demonstrated to measure salt concentrations in aqueous salt electrolytes [Svensson, 2008]. Here, the OECTs were also driven in the so called *resistive mode* with a supply voltage of only $-0.1\,V$. To be able to capture the different salt concentrations, Svensson et al. had to make use of the transient behaviour of the OECT. When operating the OECT with steady-state signals (such as shown in Figure 1.20), the drain current is independent of the salt concentration as long as there are enough ions to dope or dedope the channel. However, the complex impedance that reflects the transient behaviour, depends on the electrolyte resistance (see Equation (1.8)) which in turn is determined (amongst others) by the ionic strength. Therefore, when gating the OECT at high frequencies, where the electrolyte resistance dominates the impedance, but the OECT channel is not yet fully cut off, the Wheatstone bridge circuit gets sensitive to small changes in the electrolyte concentration. So when using two different electrolyte concentrations for both OECTs, the output voltage can be calibrated to a change in the ionic strength. This is due to the fact that one OECT exhibits a slower switching speed (the one with the lower electrolyte concentration) and therefore the floating voltage point of the corresponding branch in the bridge layout will show a lower amplitude as the other branch for the same excitation time.

A similar effect can be seen with the following experiment (see Figure 1.21a): two OECTs are connected into a Wheatstone bridge layout as shown above with two separate wells. The wells are connected with a small plastic tube and are filled up until the tube is fully filled. One single gate is immersed in one of the two wells and electrically connected to the ground. This means that one OECT is directly gated and the other OECT is gated through the tube. A sinusoidal signal at the gate with a specific frequency controls both OECTs at the same time. With the tube open, both OECTs exhibit the same switching speed. Upon applying pressure to the tube in the form of a crocodile clip, the diameter of the tube can be changed. This in turn will lead to a higher electrolyte resistance. Therefore, the OECT that is gated through the tube will exhibit a slower switching speed. This can be seen in Figure 1.21b, where a single square pulse is applied to the gate and the drain current of each OECT is monitored independently. The effect in this setup is only noticeable for small electrolyte concentrations, due to the rather big diameter of the tube and the not well defined pressure application using a crocodile clip. Nevertheless, for an electrolyte concentration of 3 mM the effect can be seen clearly.

In Figure 1.21c is shown a frequency sweep of the transconductance of the OECT that is gated through the tube for different tube diameters. Here, "fully closed" means that the clip is mounted to the whole tube but due to the plastic nature of the tube there will still be a small channel available for ionic transport. "Half closed" means that only one half of the tube is clipped and so on. The effective diameter of the tube is not directly correlated to the amount of "closure" but a clear trend can be seen. The more the tube is closed, the more the cutoff frequency is shifted towards smaller frequencies and the device act slower. It can be seen that for this particular setup, the dynamic range, i.e. the frequency band that shows the biggest change, lies between 10 Hz and 100 Hz.

A demonstration of the Wheatstone bridge sensor capability for this setup is shown in Figure 1.21d, where the output voltage of the bridge shows the peak-to-peak amplitude for a 20 Hz sinusoidal gate signal. Here, again the two extreme states (fully open tube until 10 s and fully closed tube until 20 s) show a different magnitude of the output signal. When the tube is closed, the peak-to-peak amplitude is bigger as the drain current of OECT 2 deviates more from the reference OECT 1 due to the smaller switching speed. The fact that an output signal can be seen already for a fully open tube, where the two OECTs are supposed to operate identically, is due to a fabrication mismatch between the OECTs. Even a small shift in the output characteristics of the two devices will lead to a different operation point at $V_{GS} = 0\,V$ for each branch. However, a clear change in the amplitude between unclipped and clipped tube can be seen. Note that the amplitude of the output voltage goes back to the initial value when the clip is released and tube is fully open again. The change, that basically reflects the "applied pressure" shows a frequency dependency as depicted in Figure 1.21f. It can be seen that the sensitivity exhibits a maximum, as can already be extracted from the

frequency dependency of the transconductance.

The idea was to bring this system into a miniaturized form to be able to implement it into microfluidic systems. For such systems, it is very difficult to measure the internal pressure of the microfluidic and commercial pressure sensors have to be applied at the tubing level, invalidating the idea of a lab-on-a-chip system. By fabricating the microfluidic channel across an OECT with a gate right next to it and a second OECT further down the microfluidic channel, one could basically use the Wheatstone bridge layout to calibrate the output voltage with the internal pressure of the microfluidic channel. However, the miniaturization proved more difficult and the project did not pass the stage of the rudimentary prototype shown in Figure 1.21a. Instead, it shall serve as a demonstration of the working principle of the bridge and more relevant biosensing approaches will be shown in Chapter 4.

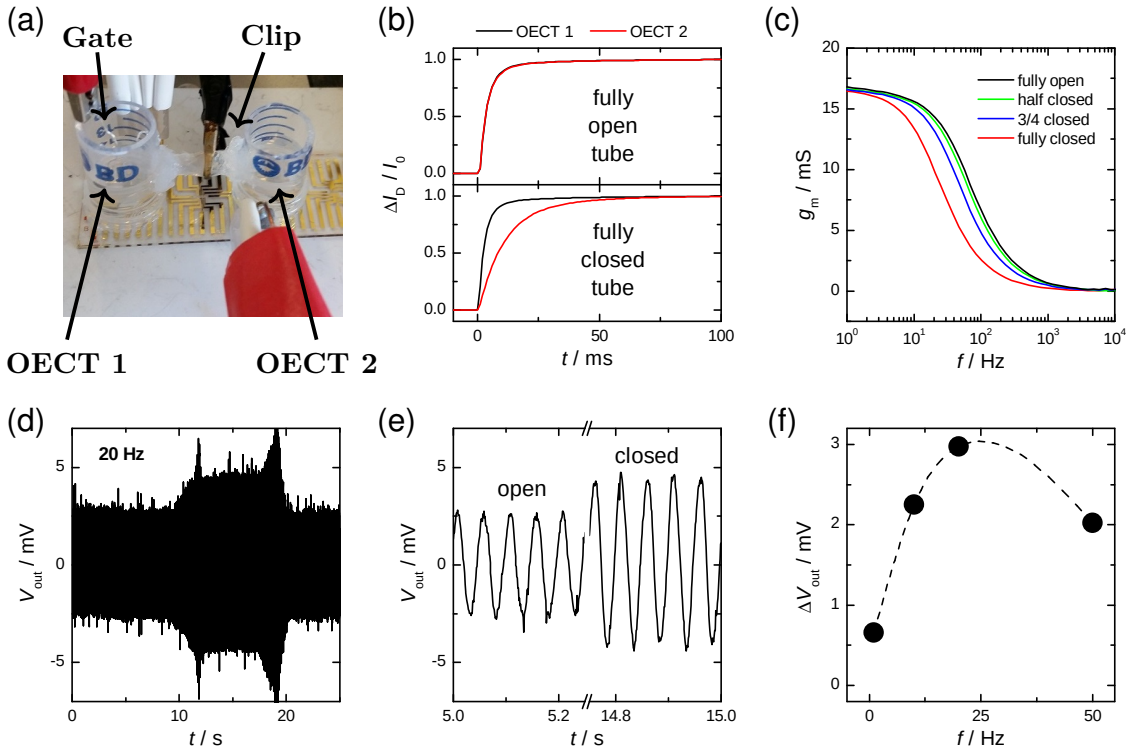

Figure 1.21: *(a) Picture of a rudimentary pressure sensitive Wheatstone bridge sensor with two PEDOT:PSS based OECTs. The OECTs are patterned on a microscope glass slide. The wells are made of a cut falcon tube glued to the substrate. The two wells are connected with a plastic tube used for microfluidic systems. One gate is immersed in one of the wells. The pressure is controlled with a crocodile clip. (b) Normalized drain current of the single OECTs to compare the switching speed when using a rectangular pulse. OECT 1 is not affected by the pressure applied to the tube. OECT 2 shows a slower switching speed when closing the tube. The device geometry was* $W = 100\,\mu m$, $L = 10\,\mu m$ *and* $d = 100\,nm$, *the source drain bias* $-0.6\,V$ *and the electrolyte concentration* $3\,mM$. *(c) Transconductance versus frequency of OECT 2 as an indicator of the switching speed. The dynamic range lies between* $10\,Hz$ *and* $100\,Hz$. *(d) Output voltage of the Wheatstone bridge sensor for a* $20\,Hz$ *sinusoidal gate signal with an amplitude of* $10\,mV$. *At around* $10\,s$, *the tube was clipped to be closed and at around* $20\,s$ *it was released again. The difference in the amplitude provides the sensor signal. The supply voltage was* $V_{Supply} = -2.5\,V$ *and the drain load* $R_{load} = 500\,\Omega$. *The data has been offset corrected by* $-4\,mV$. *(e) Zoom-in off the same data set. (f) Difference in output voltage between open and closed tube at different frequencies. The dashed line is a guide to the eye, more data points are needed to find the maximum sensitivity.*

References

[Abdellah, 2010] A. Abdellah, B. Fabel, P. Lugli, and G. Scarpa: "*Spray deposition of organic semiconducting thin-films: Towards the fabrication of arbitrary shaped organic electronic devices*", Organic Electronics **11** (2010), pp. 1031–1038.

[Abdurrahman, 2007] A. Abdurrahman, D. Price, and S. Bhansali: "*Effect of electrode geometry on the impedance evaluation of tissue and cell culture*", Sensors and Actuators B: Chemical **127** (20, 2007), pp. 89–96.

[Andersson, 2007] P. Andersson, R. Forchheimer, P. Tehrani, and M. Berggren: "*Printable All-Organic Electrochromic Active-Matrix Displays*", Advanced Functional Materials **17** (5, 2007), pp. 3074–3082.

[Bali, 2016] C. Bali, A. Brandlmaier, A. Ganster, O. Raab, J. Zapf, and A. Hübler: "*Fully Inkjet-Printed Flexible Temperature Sensors Based on Carbon and PEDOT:PSS1*", Materials Today: Proceedings **3** (2016), pp. 739–745.

[Bässler, 1993] H. Bässler: "*Charge Transport in Disordered Organic Photoconductors a Monte Carlo Simulation Study*", physica status solidi (b) **175** (1, 1993), pp. 15–56.

[Benjamin, 1961] P. Benjamin and C. Weaver: "*The Adhesion of Evaporated Metal Films on Glass*", Proceedings of the Royal Society A: Mathematical, Physical and Engineering Sciences **261** (23, 1961), pp. 516–531.

[Berggren, 2007a] M. Berggren, D. Nilsson, and N. D. Robinson: "*Organic materials for printed electronics*", Nature Materials **6** (2007), pp. 3–5.

[Berggren, 2007b] M. Berggren and A. Richter-Dahlfors: "*Organic Bioelectronics*", Advanced Materials **19** (25, 2007), pp. 3201–3213.

[Bhatt, 2016] V. D. Bhatt, S. Teymouri, K. Melzer, A. Abdellah, Z. Guttenberg, and P. Lugli: "*Biocompatibility Tests on Spray Coated Carbon Nanotube and PEDOT:PSS Thin Films*", IEEE Transactions on Nanotechnology **15** (2016), pp. 373–379.

[Bolognesi, 2002] A. Bolognesi, A. Di Carlo, and P. Lugli: "*Influence of carrier mobility and contact barrier height on the electrical characteristics of organic transistors*", Applied Physics Letters **81** (2002), p. 4646.

[Bundgaard, 2007] E. Bundgaard and F. Krebs: "*Low band gap polymers for organic photovoltaics*", Solar Energy Materials and Solar Cells **91** (6, 2007), pp. 954–985.

[Buzsáki, 2012] G. Buzsáki, C. A. Anastassiou, and C. Koch: "*The origin of extracellular fields and currents — EEG, ECoG, LFP and spikes*", Nature Reviews Neuroscience **13** (18, 2012), pp. 407–420.

[Chavan, 2014] P. Chavan: "*Organic Electronics Market by Material (Semiconductor, Conductive, Dielectric and Substrates), by Application (Battery, Conductive Ink, Display, Lighting, Logic Memory, Sensor, OPV, ORFID and Others), Geography - Global Analysis and Forecast (2014 - 2020)*", SE 2678, Markets and Markets, 2014.

[Chiang, 1977] C. K. Chiang, C. R. Fincher, Y. W. Park, A. J. Heeger, H. Shirakawa, E. J. Louis, S. C. Gau, and A. G. MacDiarmid: "*Electrical Conductivity in Doped Polyacetylene*", Physical Review Letters **39** (24, 1977), pp. 1098–1101.

[Coropceanu, 2007] V. Coropceanu, J. Cornil, D. A. da Silva Filho, Y. Olivier, R. Silbey, and J.-L. Brédas: "*Charge Transport in Organic Semiconductors*", Chemical Reviews **107** (2007), pp. 926–952.

[Cramer, 2012] T. Cramer, A. Kyndiah, M. Murgia, F. Leonardi, S. Casalini, and F. Biscarini: "*Double layer capacitance measured by organic field effect transistor operated in water*", Applied Physics Letters **100** (2, 2012), p. 143302.

[Cui, 2003] X. Cui and D. C. Martin: "*Electrochemical deposition and characterization of poly(3,4-ethylenedioxythiophene) on neural microelectrode arrays*", Sensors and Actuators B: Chemical **89** (2003), pp. 92–102.

[Cui, 2007] X. Cui and D. Zhou: "*Poly (3,4-Ethylenedioxythiophene) for Chronic Neural Stimulation*", IEEE Transactions on Neural Systems and Rehabilitation Engineering **15** (2007), pp. 502–508.

[DeFranco, 2006] J. A. DeFranco, B. S. Schmidt, M. Lipson, and G. G. Malliaras: "*Photolithographic patterning of organic electronic materials*", Organic Electronics **7** (2006), pp. 22–28.

[Ekelof, 2001] S. Ekelof: "*The genesis of the Wheatstone bridge*", Engineering Science & Education Journal **10** (1, 2001), pp. 37–40.

[Friedlein, 2015] J. T. Friedlein, S. E. Shaheen, G. G. Malliaras, and R. R. McLeod: "*Optical Measurements Revealing Nonuniform*

Hole Mobility in Organic Electrochemical Transistors", Advanced Electronic Materials **1** (2015), p. 1500189.

[Fukuda, 2014] K. Fukuda, Y. Takeda, Y. Yoshimura, R. Shiwaku, L. T. Tran, T. Sekine, M. Mizukami, D. Kumaki, and S. Tokito: "*Fully-printed high-performance organic thin-film transistors and circuitry on one-micron-thick polymer films*", Nature Communications **5** (20, 2014).

[Galvani, 1791] L. A. Galvani: "*De viribus electricitatis in motu musculari*", Ex Typographia Instituti Scientarium (1791).

[Galvani, 1797] L. A. Galvani: "*Memorie sulla elettricità animale di Luigi Galvani P. Professore di Notomia nella Università di Bologna al celebre Abate Lazzaro Spallanzani Pubblico professore nella Università di Pavia*", Bologna Sassi (1797).

[Green, 2012] R. A. Green, R. T. Hassarati, L. Bouchinet, C. S. Lee, G. L. Cheong, J. F. Yu, C. W. Dodds, G. J. Suaning, L. A. Poole-Warren, and N. H. Lovell: "*Substrate dependent stability of conducting polymer coatings on medical electrodes*", Biomaterials **33** (2012), pp. 5875–5886.

[Hess, 2011] L. H. Hess, M. Jansen, V. Maybeck, M. V. Hauf, M. Seifert, M. Stutzmann, I. D. Sharp, A. Offenhäusser, and J. A. Garrido: "*Graphene Transistor Arrays for Recording Action Potentials from Electrogenic Cells*", Advanced Materials **23** (16, 2011), pp. 5045–5049.

[Hess, 2013] L. H. Hess, M. Seifert, and J. A. Garrido: "*Graphene Transistors for Bioelectronics*", Proceedings of the IEEE **101** (2013), pp. 1780–1792.

[Heuer, 2002] H. Heuer, R. Wehrmann, and S. Kirchmeyer: "*Electrochromic Window Based on Conducting Poly(3,4-ethylenedioxythiophene)-Poly(styrene sulfonate)*", Advanced Functional Materials **12** (1, 2002), pp. 89–94.

[Hill, 1971] R. M. Hill: "*Poole-Frenkel conduction in amorphous solids*", Philosophical Magazine **23** (1971), pp. 59–86.

[Holstein, 1959] T. Holstein: "*Studies of polaron motion*", Annals of Physics **8** (1959), pp. 325–342.

[Horowitz, 1998] G. Horowitz: "*Organic Field-Effect Transistors*", Advanced Materials **10** (1998), pp. 365–377.

[Hwang, 2012] S.-W. Hwang, H. Tao, D.-H. Kim, H. Cheng, J.-K. Song, E. Rill, M. A. Brenckle, B. Panilaitis, S. M. Won, Y.-S. Kim, Y. M. Song, K. J. Yu, A. Ameen, R. Li, Y. Su, M. Yang, D. L. Kaplan, M. R. Zakin, M. J. Slepian, Y. Huang, F. G. Omenetto, and J. A. Rogers: "*A Physically Transient Form*

of Silicon Electronics", Science **337** (28, 2012), pp. 1640–1644.

[IrimiaVladu, 2010] M. Irimia-Vladu, P. A. Troshin, M. Reisinger, L. Shmygleva, Y. Kanbur, G. Schwabegger, M. Bodea, R. Schwödiauer, A. Mumyatov, J. W. Fergus, V. F. Razumov, H. Sitter, N. S. Sariciftci, and S. Bauer: "*Biocompatible and Biodegradable Materials for Organic Field-Effect Transistors*", Advanced Functional Materials **20** (8, 2010), pp. 4069–4076.

[Janssen, 2007] G. Janssen, A. Aguirre, E. Goovaerts, P. Vanlaeke, J. Poortmans, and J. Manca: "*Optimization of morphology of P3HT/PCBM films for organic solar cells: effects of thermal treatments and spin coating solvents*", The European Physical Journal Applied Physics **37** (2007), pp. 287–290.

[Jin Jang, 2002] Jin Jang, Sungkyoo Lim, and Myunghwan Oh: "*Technology development and production of flat panel displays in Korea*", Proceedings of the IEEE **90** (2002), pp. 501–513.

[Jonsson, 2016] A. Jonsson, S. Inal, l. Uguz, A. J. Williamson, L. Kergoat, J. Rivnay, D. Khodagholy, M. Berggren, C. Bernard, G. G. Malliaras, and D. T. Simon: "*Bioelectronic neural pixel: Chemical stimulation and electrical sensing at the same site*", Proceedings of the National Academy of Sciences **113** (23, 2016), pp. 9440–9445.

[Kafka, 2010] J. Kafka, N. B. Larsen, S. Skaarup, and O. Geschke: "*Fabrication of an all-polymer electrochemical sensor by using a one-step hot embossing procedure*", Microelectronic Engineering **87** (2010), pp. 1239–1241.

[Kergoat, 2012] L. Kergoat, B. Piro, M. Berggren, M.-C. Pham, A. Yassar, and G. Horowitz: "*DNA detection with a water-gated organic field-effect transistor*", Organic Electronics **13** (2012), pp. 1–6.

[Kerner, 1998] Z. Kerner and T. Pajkossy: "*Impedance of rough capacitive electrodes: the role of surface disorder*", Journal of Electroanalytical Chemistry **448** (1998), pp. 139–142.

[Khodagholy, 2013a] D. Khodagholy, T. Doublet, P. Quilichini, M. Gurfinkel, P. Leleux, A. Ghestem, E. Ismailova, T. Hervé, S. Sanaur, C. Bernard, and G. G. Malliaras: "*In vivo recordings of brain activity using organic transistors*", Nature Communications **4** (2013), p. 1575.

[Khodagholy, 2013b] D. Khodagholy, J. Rivnay, M. Sessolo, M. Gurfinkel, P. Leleux, L. H. Jimison, E. Stavrinidou, T. Herve, S. Sanaur, R. M. Owens, and G. G. Malliaras: "*High transconductance*

organic electrochemical transistors", Nature Communications **4** (12, 2013), p. 2133.

[Kim, 2011] Y. H. Kim, C. Sachse, M. L. Machala, C. May, L. Müller-Meskamp, and K. Leo: "*Highly Conductive PEDOT:PSS Electrode with Optimized Solvent and Thermal Post-Treatment for ITO-Free Organic Solar Cells*", Advanced Functional Materials **21** (22, 2011), pp. 1076–1081.

[Kittlesen, 1984] G. P. Kittlesen, H. S. White, and M. S. Wrighton: "*Chemical derivatization of microelectrode arrays by oxidation of pyrrole and N-methylpyrrole: fabrication of molecule-based electronic devices*", Journal of the American Chemical Society **106** (1984), pp. 7389–7396.

[Klauk, 2007] H. Klauk, U. Zschieschang, J. Pflaum, and M. Halik: "*Ultralow-power organic complementary circuits*", Nature **445** (15, 2007), pp. 745–748.

[Kodandaramaiah, 2012] S. B. Kodandaramaiah, G. T. Franzesi, B. Y. Chow, E. S. Boyden, and C. R. Forest: "*Automated whole-cell patch-clamp electrophysiology of neurons in vivo*", Nature Methods **9** (6, 2012), pp. 585–587.

[Kok, 2004] M. M. de Kok, M. Buechel, S. I. E. Vulto, P. van de Weijer, E. A. Meulenkamp, S. H. P. M. de Winter, A. J. G. Mank, H. J. M. Vorstenbosch, C. H. L. Weijtens, and V. van Elsbergen: "*Modification of PEDOT:PSS as hole injection layer in polymer LEDs*", physica status solidi (a) **201** (2004), pp. 1342–1359.

[Krebs, 2009] F. C. Krebs: "*Polymer solar cell modules prepared using roll-to-roll methods: Knife-over-edge coating, slot-die coating and screen printing*", Solar Energy Materials and Solar Cells **93** (2009), pp. 465–475.

[Kringelbach, 2007] M. L. Kringelbach, N. Jenkinson, S. L. Owen, and T. Z. Aziz: "*Translational principles of deep brain stimulation*", Nature Reviews Neuroscience **8** (2007), pp. 623–635.

[Le Comber, 1970] P. G. Le Comber and W. E. Spear: "*Electronic Transport in Amorphous Silicon Films*", Physical Review Letters **25** (24, 1970), pp. 509–511.

[Leleux, 2014] P. Leleux, J.-M. Badier, J. Rivnay, C. Bénar, T. Hervé, P. Chauvel, and G. G. Malliaras: "*Conducting Polymer Electrodes for Electroencephalography*", Advanced Healthcare Materials **3** (2014), pp. 490–493.

[Ludwig, 2006] K. A. Ludwig, J. D. Uram, J. Yang, D. C. Martin, and D. R. Kipke: "*Chronic neural recordings using silicon microelectrode arrays electrochemically deposited with a poly(3,4-*

ethylenedioxythiophene) (PEDOT) film", Journal of Neural Engineering **3** (1, 2006), pp. 59–70.

[Magliulo, 2013] M. Magliulo, A. Mallardi, M. Y. Mulla, S. Cotrone, B. R. Pistillo, P. Favia, I. Vikholm-Lundin, G. Palazzo, and L. Torsi: "*Electrolyte-Gated Organic Field-Effect Transistor Sensors Based on Supported Biotinylated Phospholipid Bilayer*", Advanced Materials **25** (11, 2013), pp. 2090–2094.

[Matteucci, 1838] C. Matteucci: "*Sur le courant électrique où propre de la grenouille. Second memoire sur l'électricité animale*", Annales de Chimie et de Physique **67** (1838), pp. 93–106.

[McConnell, 2009] G. C. McConnell, H. D. Rees, A. I. Levey, C.-A. Gutekunst, R. E. Gross, and R. V. Bellamkonda: "*Implanted neural electrodes cause chronic, local inflammation that is correlated with local neurodegeneration*", Journal of Neural Engineering **6** (1, 2009), p. 056003.

[McCullough, 1993] R. D. McCullough and S. P. Williams: "*Toward tuning electrical and optical properties in conjugated polymers using side-chains: highly conductive head-to-tail, heteroatom functionalized polythiophenes*", Journal of the American Chemical Society **115** (1993), pp. 11608–11609.

[Meng, 2015] Y. Meng, Z. B. Li, X. Chen, and J. P. Chen: "*A flexible dry micro-dome electrode for ECG monitoring*", Microsystem Technologies **21** (2015), pp. 1241–1248.

[Mori, 2013] M. Mori, Y. Hirose, M. Segawa, I. Miyamaga, R. Miyagawa, T. Ueda, H. Nara, H. Masuda, S. Kishimura, T. Sasaki, Y. kato, Y. Imada, H. Asamo, H. Inomata, H. Koguchi, M. Ihama, and Y. Mishima: "*Thin Organic Photoconductive Film Image Sensors with Extremely High Saturation of 8500 electrons per micrometer squared*", 2013 Symposium on VLSI Circuits, Kyoto, Japan*, (2013), T22–T23.

[Nielsen, 2016] C. B. Nielsen, A. Giovannitti, D.-T. Sbircea, E. Bandiello, M. R. Niazi, D. A. Hanifi, M. Sessolo, A. Amassian, G. G. Malliaras, J. Rivnay, and I. McCulloch: "*Molecular Design of Semiconducting Polymers for High-Performance Organic Electrochemical Transistors*", Journal of the American Chemical Society **138** (17, 2016), pp. 10252–10259.

[Northrup, 2007] J. E. Northrup: "*Atomic and electronic structure of polymer organic semiconductors: P3HT, PQT, and PBTTT*", Physical Review B **76** (13, 2007).

[Novoselov, 2005] K. S. Novoselov, A. K. Geim, S. V. Morozov, D. Jiang, M. I. Katsnelson, I. V. Grigorieva, S. V. Dubonos, and A. A.

Firsov: "*Two-dimensional gas of massless Dirac fermions in graphene*", Nature **438** (10, 2005), pp. 197–200.

[Ouyang, 2011] L. Ouyang, R. Green, K. E. Feldman, and D. C. Martin: "*Direct local polymerization of poly(3,4-ethylenedioxythiophene) in rat cortex*", *Progress in Brain Research*, **194**, Elsevier (2011), pp. 263–271, ISBN: 9780444538154.

[Pardridge, 2005] W. M. Pardridge: "*The blood-brain barrier: Bottleneck in brain drug development*", NeuroRX **2** (2005), pp. 3–14.

[Park, 2012] S. J. Park, O. S. Kwon, S. H. Lee, H. S. Song, T. H. Park, and J. Jang: "*Ultrasensitive Flexible Graphene Based Field-Effect Transistor (FET)-Type Bioelectronic Nose*", Nano Letters **12** (10, 2012), pp. 5082–5090.

[Pathak, 2015] C. Pathak, J. Singh, and R. Singh: "*Effect of dimethyl sulfoxide on the electrical properties of PEDOT:PSS/n-Si heterojunction diodes*", Current Applied Physics **15** (2015), pp. 528–534.

[Patil, 1988] A. O. Patil, A. J. Heeger, and F. Wudl: "*Optical properties of conducting polymers*", Chemical Reviews **88** (1988), pp. 183–200.

[Pavlovic, 2011] E. Pavlovic and E. J. Kramer: "*Curing Temperature Effects on Network Structure and Chemistry of Silane Coupling Agent Layers and Their Influence on Water-Assisted Crack Growth*", The Journal of Adhesion **87** (16, 2011), pp. 272–289.

[Piccolino, 1997] M. Piccolino: "*Luigi Galvani and animal electricity: two centuries after the foundation of electrophysiology*", Trends in Neurosciences **20** (1, 1997), pp. 443–448.

[Polikov, 2005] V. S. Polikov, P. A. Tresco, and W. M. Reichert: "*Response of brain tissue to chronically implanted neural electrodes*", Journal of Neuroscience Methods **148** (2005), pp. 1–18.

[Proctor, 2016] C. M. Proctor, J. Rivnay, and G. G. Malliaras: "*Understanding volumetric capacitance in conducting polymers*", Journal of Polymer Science Part B: Polymer Physics **54** (1, 2016), pp. 1433–1436.

[Riordan, 2004] M. Riordan: "*The lost history of the transistor*", IEEE Spectrum **41** (2004), pp. 44–49.

[Ritter, 2015] P. Ritter, G. Z. Duray, S. Zhang, C. Narasimhan, K. Soejima, R. Omar, V. Laager, K. Stromberg, E. Williams, D. Reynolds, and for the Micra Transcatheter Pacing Study Group: "*The rationale and design of the Micra Transcatheter Pacing Study: safety and efficacy of a novel miniaturized pacemaker*", Europace **17** (1, 2015), pp. 807–813.

[Rivnay, 2013] J. Rivnay, P. Leleux, M. Sessolo, D. Khodagholy, T. Hervé, M. Fiocchi, and G. G. Malliaras: "*Organic Electrochemical Transistors with Maximum Transconductance at Zero Gate Bias*", Advanced Materials **25** (2013), pp. 7010–7014.

[Rivnay, 2014] J. Rivnay, R. M. Owens, and G. G. Malliaras: "*The Rise of Organic Bioelectronics*", Chemistry of Materials **26** (14, 2014), pp. 679–685.

[Rivnay, 2015a] J. Rivnay, P. Leleux, M. Ferro, M. Sessolo, A. Williamson, D. A. Koutsouras, D. Khodagholy, M. Ramuz, X. Strakosas, R. M. Owens, C. Benar, J.-M. Badier, C. Bernard, and G. G. Malliaras: "*High-performance transistors for bioelectronics through tuning of channel thickness*", Science Advances **1** (22, 2015), e1400251–e1400251.

[Rivnay, 2015b] J. Rivnay, M. Ramuz, P. Leleux, A. Hama, M. Huerta, and R. M. Owens: "*Organic electrochemical transistors for cell-based impedance sensing*", Applied Physics Letters **106** (26, 2015), p. 043301.

[Rivnay, 2016] J. Rivnay, S. Inal, B. A. Collins, M. Sessolo, E. Stavrinidou, X. Strakosas, C. Tassone, D. M. Delongchamp, and G. G. Malliaras: "*Structural control of mixed ionic and electronic transport in conducting polymers*", Nature Communications **7** (19, 2016), p. 11287.

[Sakamoto, 2004] Y. Sakamoto, T. Suzuki, M. Kobayashi, Y. Gao, Y. Fukai, Y. Inoue, F. Sato, and S. Tokito: "*Perfluoropentacene: High-Performance p-n Junctions and Complementary Circuits with Pentacene*", Journal of the American Chemical Society **126** (2004), pp. 8138–8140.

[Salleo, 2004] A. Salleo, T. W. Chen, A. R. Völkel, Y. Wu, P. Liu, B. S. Ong, and R. A. Street: "*Intrinsic hole mobility and trapping in a regioregular poly(thiophene)*", Physical Review B **70** (17, 2004).

[Salzner, 1998] U. Salzner, J. Lagowski, P. Pickup, and R. Poirier: "*Comparison of geometries and electronic structures of polyacetylene, polyborole, polycyclopentadiene, polypyrrole, polyfuran, polysilole, polyphosphole, polythiophene, polyselenophene and polytellurophene*", Synthetic Metals **96** (1998), pp. 177–189.

[SaremAslani, 2011] A. Sarem-Aslani and K. Mullett: "*Industrial Perspective on Deep Brain Stimulation: History, Current State, and Future Developments*", Frontiers in Integrative Neuroscience **5** (2011).

[Scarpa, 2010a] G. Scarpa, A.-L. Idzko, S. Götz, and S. Thalhammer: "*Biocompatibility Studies of Functionalized Regioregular Poly(3-hexylthiophene) Layers for Sensing Applications*", Macromolecular Bioscience **10** (8, 2010), pp. 378–383.

[Scarpa, 2010b] G. Scarpa, A.-L. Idzko, A. Yadav, and S. Thalhammer: "*Organic ISFET Based on Poly (3-hexylthiophene)*", Sensors **10** (19, 2010), pp. 2262–2273.

[Sessolo, 2013] M. Sessolo, D. Khodagholy, J. Rivnay, F. Maddalena, M. Gleyzes, E. Steidl, B. Buisson, and G. G. Malliaras: "*Easy-to-Fabricate Conducting Polymer Microelectrode Arrays*", Advanced Materials **25** (18, 2013), pp. 2135–2139.

[Shin, 2013] Y. Shin, A. P. Perera, and M. K. Park: "*Label-free DNA sensor for detection of bladder cancer biomarkers in urine*", Sensors and Actuators B: Chemical **178** (2013), pp. 200–206.

[Silinsh, 1995] E. Silinsh, A. Klimkans, S. Larsson, and V. Capek: "*Molecular polaron states in polyacene crystals. Formation and transfer processes*", Chemical Physics **198** (1995), pp. 311–331.

[Singh, 2014] R. Singh: "*Organic Electronics Market by Applications (Display, ORFID, OLED Lighting, Photo Voltaic, System Components) - Global Opportunity Analysis and Industry Forecast, 2013 - 2020*", SE 14188, Allied Market Research, 2014.

[Sirringhaus, 2000] H. Sirringhaus, T. Kawase, R. H. Friend, T. Shimoda, M. Inbasekaran, W. Wu, and E. P. Woo: "*High-Resolution Inkjet Printing of All-Polymer Transistor Circuits*", Science **290** (15, 2000), pp. 2123–2126.

[Søndergaard, 2013] R. R. Søndergaard, M. Hösel, and F. C. Krebs: "*Roll-to-Roll fabrication of large area functional organic materials*", Journal of Polymer Science Part B: Polymer Physics **51** (1, 2013), pp. 16–34.

[Stavrinidou, 2013] E. Stavrinidou, P. Leleux, H. Rajaona, D. Khodagholy, J. Rivnay, M. Lindau, S. Sanaur, and G. G. Malliaras: "*Direct Measurement of Ion Mobility in a Conducting Polymer*", Advanced Materials **25** (27, 2013), pp. 4488–4493.

[Strakosas, 2017] X. Strakosas, M. Huerta, M. J. Donahue, A. Hama, A.-M. Pappa, M. Ferro, M. Ramuz, J. Rivnay, and R. M. Owens: "*Catalytically enhanced organic transistors for in vitro toxicology monitoring through hydrogel entrapment of enzymes*", Journal of Applied Polymer Science **134** (15, 2017).

[Svensson, 2008] P.-O. Svensson, D. Nilsson, R. Forchheimer, and M. Berggren: "*A sensor circuit using reference-based conductance*

switching in organic electrochemical transistors", Applied Physics Letters **93** (2008), p. 203301.

[Takamatsu, 2015] S. Takamatsu, T. Lonjaret, D. Crisp, J.-M. Badier, G. G. Malliaras, and E. Ismailova: "*Direct patterning of organic conductors on knitted textiles for long-term electrocardiography*", Scientific Reports **5** (8, 2015), p. 15003.

[Tan, 1989] E. M. Tan: "*Antinuclear Antibodies: Diagnostic Markers for Autoimmune Diseases and Probes for Cell Biology*", Advances in Immunology **44** (1989), pp. 93–151.

[Tan, 2009] H. S. Tan, N. Mathews, T. Cahyadi, F. R. Zhu, and S. G. Mhaisalkar: "*The effect of dielectric constant on device mobilities of high-performance, flexible organic field effect transistors*", Applied Physics Letters **94** (2009), p. 263303.

[Tanase, 2003] C. Tanase, E. J. Meijer, P. W. M. Blom, and D. M. de Leeuw: "*Unification of the Hole Transport in Polymeric Field-Effect Transistors and Light-Emitting Diodes*", Physical Review Letters **91** (19, 2003).

[Tanenbaum, 1956] M. Tanenbaum and D. E. Thomas: "*Diffused Emitter and Base Silicon Transistors*", Bell System Technical Journal **35** (1956), pp. 1–22.

[Taylor, 2009] P. G. Taylor, J.-K. Lee, A. A. Zakhidov, M. Chatzichristidi, H. H. Fong, J. A. DeFranco, G. G. Malliaras, and C. K. Ober: "*Orthogonal Patterning of PEDOT:PSS for Organic Electronics using Hydrofluoroether Solvents*", Advanced Materials **21** (12, 2009), pp. 2314–2317.

[Tsai, 2005] W. Tsai: "*Environmental risk assessment of hydrofluoroethers (HFEs)*", Journal of Hazardous Materials **119** (17, 2005), pp. 69–78.

[Venkatraman, 2011] S. Venkatraman, J. Hendricks, Z. A. King, A. J. Sereno, S. Richardson-Burns, D. Martin, and J. M. Carmena: "*In Vitro and In Vivo Evaluation of PEDOT Microelectrodes for Neural Stimulation and Recording*", IEEE Transactions on Neural Systems and Rehabilitation Engineering **19** (2011), pp. 307–316.

[Wang, 2011] T. J. Wang, M. G. Larson, R. S. Vasan, S. Cheng, E. P. Rhee, E. McCabe, G. D. Lewis, C. S. Fox, P. F. Jacques, C. Fernandez, C. J. O'Donnell, S. A. Carr, V. K. Mootha, J. C. Florez, A. Souza, O. Melander, C. B. Clish, and R. E. Gerszten: "*Metabolite profiles and the risk of developing diabetes*", Nature Medicine **17** (2011), pp. 448–453.

[Waser, 2012] R. Waser, ed.: "*Nanoelectronics and information technology: advanced electronic materials and novel devices*", 3., com-

pletely rev. and enl. ed, OCLC: 794211089, Weinheim 2012, 1040 pp., ISBN: 9783527409273.

[Wei, 2013] Q. Wei, M. Mukaida, Y. Naitoh, and T. Ishida: "*Morphological Change and Mobility Enhancement in PEDOT:PSS by Adding Co-solvents*", Advanced Materials **25** (28, 2013), pp. 2831–2836.

[Werkmeister, 2013] F. Werkmeister and B. Nickel: "*Towards flexible organic thin film transistors (OTFTs) for biosensing*", Journal of Materials Chemistry B **1** (2013), p. 3830.

[Wiel, 2014] B. v. der Wiel, H.-J. Egelhaaf, H. Issa, M. Roos, and N. Henze: "*Market Readiness of Organic Photovoltaics for Building Integration*", MRS Proceedings **1639** (2014).

[Williamson, 2015] A. Williamson, M. Ferro, P. Leleux, E. Ismailova, A. Kaszas, T. Doublet, P. Quilichini, J. Rivnay, B. Rózsa, G. Katona, C. Bernard, and G. G. Malliaras: "*Localized Neuron Stimulation with Organic Electrochemical Transistors on Delaminating Depth Probes*", Advanced Materials **27** (2015), pp. 4405–4410.

[Xue, 1987] G. Xue: "*Chemical Reactions of an Epoxy-Functional Silane in Aqueous Solution*", Die Angewandte Makromolekulare Chemie **151** (1987), pp. 85–93.

[Zhang, 2006] Y. Zhang, W. van Drongelen, and B. He: "*Estimation of in vivo brain-to-skull conductivity ratio in humans*", Applied Physics Letters **89** (27, 2006), p. 223903.

[Zhang, 2015] S. Zhang, P. Kumar, A. S. Nouas, L. Fontaine, H. Tang, and F. Cicoira: "*Solvent-induced changes in PEDOT:PSS films for organic electrochemical transistors*", APL Materials **3** (1, 2015), p. 014911.

[Zywietz, 2003] C. Zywietz: "*A brief history of electrocardiography-progress through technology*", Proc. Tutorial, Biosignal Institute for Biosignal Processing and Systems Research (2003).

Chapter 2

Organic Transistor Arrays Integrated with Finger-Powered Microfluidics for Multianalyte Saliva Testing

This chapter is based on the publication:

"Organic Transistor Arrays Integrated with Finger-Powered Microfluidics for Multianalyte Saliva Testing"

A-M. Pappa, V. F. Curto, M. Braendlein, X. Strakosas, M. J. Donahue, M. Fiocchi, G. G. Malliaras, R. M. Owens

Advanced Healthcare Materials, Volume 5, Issue 17, DOI:10.1002/adhm.201600494 (2016).

A compact multianalyte biosensing platform is reported, composed of an organic electrochemical transistor (OECT) microarray integrated with a pump-less "finger-powered" microfluidic, for quantitative screening of glucose, lactate, and cholesterol levels. A biofunctionalization method is designed, which provides selectivity towards specific metabolites as well as minimization of any background interference. In addition, a simple method is developed to facilitate multi-analyte sensing and avoid electrical crosstalk between the different transistors by electrically isolating the individual devices. The resulting biosensing platform, verified using human samples, offers the possibility to be used in easy-to-obtain biofluids with low abundance metabolites, such as saliva. Based on our proposed method, other types of enzymatic biosensors can be integrated into the array to achieve multiplexed, noninvasive, personalized point-of-care diagnostics.

2.1 Introduction

Point-of-care testing (POCT) is one of the fastest growing sectors of medical diagnostics. However, effective POCT methods pose stringent requirements and challenges for biosensor development [Liu, 2012; Kumar, 2013; Wan, 2013]. Multiplexed and compact devices for high throughput analysis in a cost-effective and time-saving manner are urgently required for next generation biosensors, to provide more holistic and accurate understanding of the system under investigation. Advances in electronics and microfabrication have allowed the miniaturization of various optical and electronic transducers allowing for faster and more sensitive devices for diagnostics [Willner, 2002; Turner, 2000]. Despite these developments, it remains challenging to develop portable, low-cost biosensing platforms that are able to detect multiple metabolites simultaneously with high sensitivity and selectivity.

Lactate, glucose, and cholesterol are metabolites of critical importance in healthcare. Although cellular metabolic pathways are somewhat complex, quantification of such key markers in normal and under different conditions, as well as assaying their relative abundance compared to other metabolites, can provide useful insights for the health status of an individual. For example, due to the close metabolic relationship between glucose and lactate, fluctuations of their absolute or relative concentrations, along with cholesterol quantification, can be correlated with certain medical conditions such as heart disease and diabetes [Wang, 2013; Arya, 2008]. Commercialized metabolite sensor chips rely mainly on finger-stick blood draws. However, the intrusiveness and inconvenience of such blood-sampling methods as well as the stringent requirements for continuous real-time sampling and screening (for example in areas as diverse as critical healthcare units to sports medicine) emphasize the importance of noninvasive biosensing technologies using alternative biofluids such as saliva [Lee, 2009].

Organic electrochemical transistors (OECTs) represent a very promising class of organic thin film transistors (OTFTs) that have recently fueled scientific interest as especially performant transducers in sensing applications. OECTs couple the advantages of OTFTs [Torsi, 2013] (i.e., simple electrical readout, inherent signal amplification, ease of fabrication and straightforward miniaturization), with electrochemically driven operation in aqueous solutions, thereby establishing a conduit between electronics and biology [Strakosas, 2015]. OECTs, unlike the vast majority of OTFTs, comprise an organic active layer, which is in direct contact with the biological milieu of interest. The working principle relies on the electrochemical doping/de-doping of the organic semiconductor upon application of a small gate bias [Khodagholy, 2013; Bernards, 2007]. As amplifying transducers of ionic-to-electronic signals, OECTs can also be integrated with microfluidic channels toward lab-on-a-chip applications [Mabeck, 2005; Yang, 2009].

Poly(3,4-ethylene-dioxythiophene):poly(styrene sulfonic acid) (PEDOT:PSS) has e-

merged as the benchmark material of organic bioelectronics [Lanzani, 2014; Simon, 2009; Sessolo, 2013] and is typically employed as the active layer of OECTs. Such devices have been used as ionselective sensors [Sessolo, 2014; Lin, 2010], cell-based sensors [Tria, 2014; Rivnay, 2015] and when coupled with redox enzymes, as biocatalytic sensors for the detection of metabolites (i.e., glucose, lactate, etc.) [Bernards, 2008; Khodagholy, 2012; Tang, 2011], the latter showing great potential for POCT applications. Kergoat et al. recently reported on the use of PEDOT:PSS-based OECTs for single-analyte detection of critical neurotransmitters such as glutamate and acetylcholine[Kergoat, 2014], while Liao et al. demonstrated sensitive and selective single-analyte detection of key metabolites such as glucose and urea in saliva samples, as a potential POCT system [Liao, 2015]. In those studies, as in most cases of amperometric biosensors using an oxidase type of enzyme, the sensing mechanism relies on the detection of hydrogen peroxide (H_2O_2), a by-product of the enzymatic reactions. In practical applications, such approaches suffer from several constraints related to the selectivity of the device mainly due to the existence of electro-active compounds in complex media. Specifically, the relatively high potential (0.6 V vs. Ag/AgCl reference) required for the oxidation of H_2O_2 increases significantly the level of interference from endogenous electroactive species (e.g., uric acid, dopamine, and ascorbic acid) that are present in bodily fluids, leading to misinterpretation of the recorded signals. One possible strategy to reduce or eliminate electrochemical interference of endogenous species is through the use of permselective membranes such as nafion and poly-lysine for size or charge-based exclusion of the interferents [Liao, 2015].

In the case of multianalyte detection from a single biological sample, diffusion of H_2O_2 between adjacent biosensors may also lead to signal misinterpretation. Notably, two kinds of "cross-talk" should be considered, electrical and chemical. The former results primarily from capacitive coupling and the latter from diffusion of H_2O_2 [Wilson, 2005]. Arguably, a more elegant alternative to the detection of H_2O_2 is the use of mediators as a strategy to improve selectivity and performance of such amperometric biosensors. Indeed, as we show in this study, by using a novel biofunctionalization scheme incorporating an electron mediator (ferrocene), molecular wiring of the enzyme active site to the electrode is achieved, thus lowering the working potential of the electrodes, and reducing background signal.

We report here, for the first time, the development of a compact biosensing platform consisting of multiplexed OECTs for the simultaneous detection of three critical biomarkers: glucose, lactate, and cholesterol. The real-time detection of a combination of analytes from human saliva samples is achieved in a noninvasive and label-free manner with high selectivity and sensitivity in the relevant physiological ranges. Additionally, this versatile platform is integrated with a simple pumpless poly(dimethylsiloxane) (PDMS)-based microfluidic towards the realization of POCT devices.

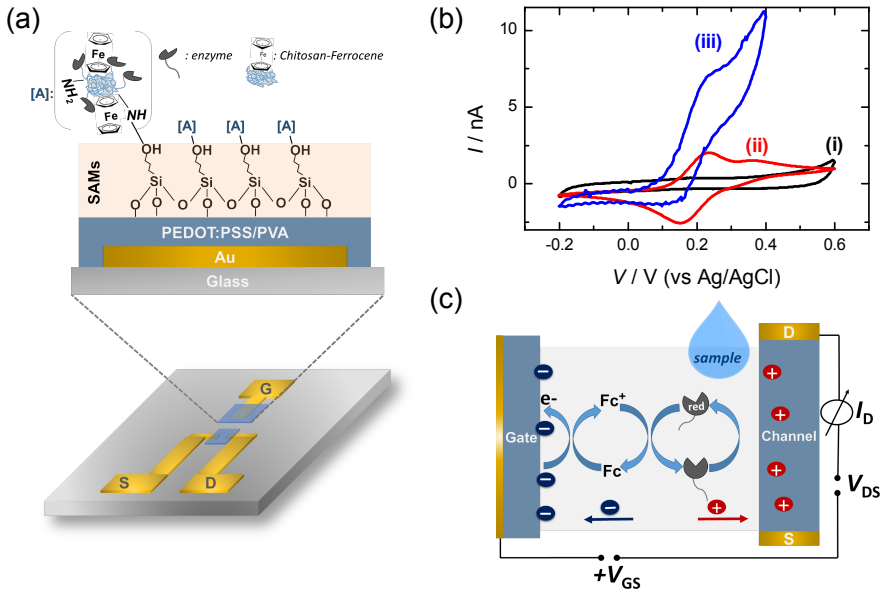

Figure 2.1: *OECT biofunctionalization and use for enzymatic sensing. (a) Schematic representation of the OECT device structure and an illustration of the generic biofunctionalization scheme at the gate electrode. (b) Cyclic voltammogram of the gate electrode in PBS (scan rate:* $20\,\mathrm{mV\,s^{-1}}$*) before gate functionalization (i), after gate functionalization with CS-Fc/GO x complex (ii) and in the presence of* $10\,\mathrm{mM}$ *glucose (iii). (c) Schematic illustration of the general sensing mechanism using an OECT-based sensing configuration.*

2.2 Results and Discussion

2.2.1 OECT Biofunctionalization and Use for Enzymatic Sensing

Figure 2.1 shows a schematic illustration of the device structure of a single OECT fabricated on a glass substrate, as well as the generic biofunctionalization scheme at the planar gate electrode of each transistor, based on the method of Strakosas et al. [Strakosas, 2014]. Briefly, by blending PEDOT:PSS with polyvinyl alcohol (PVA), we introduce free hydroxyl groups on the surface of the conducting polymer, a functionality subsequently used for covalent attachment of a heterobifunctional silane (3-glycidoxypropyltrimethoxysilane, GOPS) via a condensation reaction. A different protein was then immobilized on each gate electrode of the four transistors, namely glucose oxidase (GOx), lactate oxidase (LOx), and cholesterol oxidase (ChOx) for the respective detection of glucose, lactate, and cholesterol. Bovine serum albumin (BSA) was immobilized on the fourth electrode serving as the control.

The first generation of enzymatic biosensors, in which the co-substrate for the enzyme is oxygen, suffer from several disadvantages, principally oxygen dependence and inter-

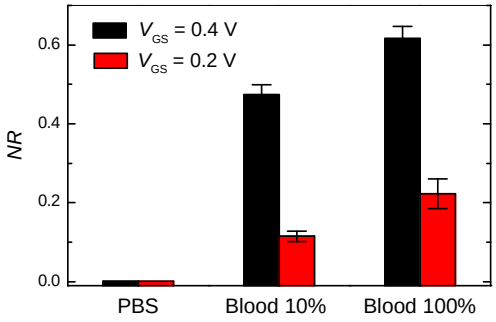

Figure 2.2: *Normalized response of the OECT under different gate bias in the presence of complex media (whole blood) in a diluted (10 %) and undiluted form.*

ference from electro-oxidizable compounds. Indeed, when we used a highly complex biological matrix, i.e., whole blood, we observed a significant decrease in the background signal when the same device was operated at a low potential of $V_{GS} = 0.2\,V$ compared to a higher potential of $V_{GS} = 0.4\,V$ (Figure 2.2). To circumvent this issue, other types of redox active molecules have been used as an alternative co-substrate for the enzyme (known as electrochemical mediators), to reduce the applied potential to near zero values [Scheiblin, 2015; Shim, 2009].

Among the electron mediators used in biosensing applications, ferrocene (Fc), a stable organometallic compound, is frequently used due to its favorable intrinsic properties (i.e., low molecular mass, good electrochemical stability, and reversibility at low potentials and formation of stable redox states) [Fernández, 2005]. However, Fc adsorbs weakly onto metal electrodes due to its small size and low affinity with such surfaces, leading to leaching of Fc, with subsequent concerns for toxicity. A solution to this issue is to provide a supporting matrix to improve the stability of the system.

In this work, Fc-branched chitosan (CS) derivatives were prepared [Yang, 2007] to act as redox active hybrid electrochemical shuttles for the biosensor. CS, a biopolymer with remarkable physico-chemical properties (i.e., film forming ability, high permeability towards water, good mechanical properties and non-toxicity) [Quignard, 2000], was chosen as an effective biocompatible support for both the mediator and the enzyme. We hypothesized that by creating a microenvironment where the enzyme and the mediator are confined to a small volume adjacent to the electrode, the efficiency of electron transfer would be substantially improved. The enzyme was attached to the CS-Fc hybrid, by amine coupling of the residual amine groups of CS-Fc through N-(3-dimethylaminopropyl)-N'-ethylcarbodiimide hydrochloride/sulfo-N-hydroxysuccinimide (EDC/NHS) chemistry, and immobilized onto the epoxy-modified gate electrode via covalent attachment of the amine groups present in the biocomplex (Figure 2.1a). Figure 2.1b shows cyclic voltammograms of the pristine gate electrode (i) and the CS-Fc/GOx composite modified electrode in phosphate buffer solution

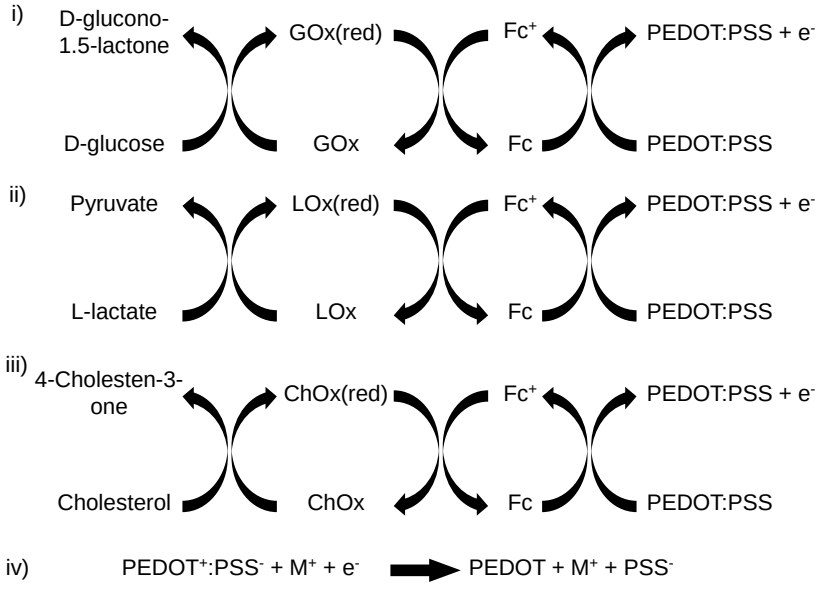

Figure 2.3: *Reaction mechanisms at the gate electrode for detection of glucose (i), lactate (ii) and cholesterol (iii) respectively as well as the subsequent reactions at the channel (iv).*

(PBS) (ii), as well as that of the modified electrode in the presence of glucose (iii). The well-defined and symmetric peaks at 0.25 V and 0.15 V of the modified electrode in PBS are characteristic of the immobilized Fc group, whereas the drastic increase of the current in the presence of glucose in the buffer solution indicates the effective immobilization of GOx and the expected enzymatic reaction.

The sensing mechanism of our platform, based on the enzyme/mediator complex functionalized gate electrode is illustrated in Figure 2.1c. Upon addition of a sample containing the substrate of interest, an enzymatic reaction occurs, the enzyme is reduced and cycles back via the ferrocene/ferricenium (Fc/Fc+) ion couple which mediates electron transfer between the redox enzyme and the PEDOT:PSS gate electrode, due to its low oxidation potential. The resulting change in the gating of the channel is proportional to the concentration of the analyte allowing its quantification. The reaction cycles at the gate electrode for each of the three analytes along with the subsequent reactions at the channel are shown in Figure 2.3.

2.2.2 Characterization of Biofunctionalized OECTs

OECTs have proven to exhibit the highest transconductance (g_{m}) among electrolyte-gated transistors of comparable geometry [Khodagholy, 2013], defined as $g_{\mathrm{m}} = \partial I_{\mathrm{D}}/\partial V_{\mathrm{GS}}$. Transconductance is the figure of merit for biosensing applications as

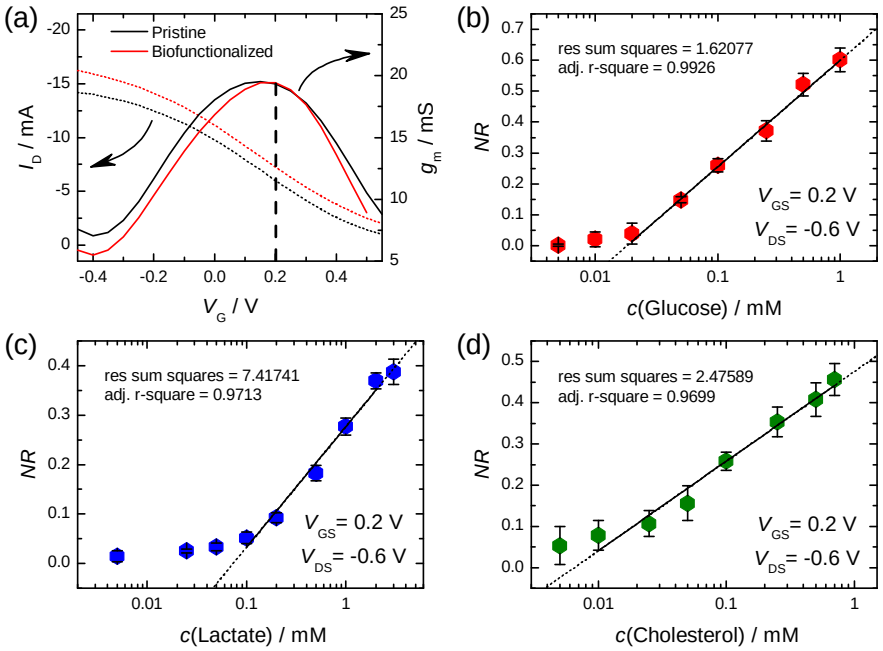

Figure 2.4: *Characterization of the biofunctionalized OECTs. (a) Steady state characteristics of a representative OECT: transfer curve and the corresponding transconductance (dashed line indicates the working point of the OECTs for signal acquisition), before and after biofunctionalization. (b-d) Normalized calibration curves derived from the chronoamperometric response of the OECTs after successive additions of increasing concentrations of the analytes glucose, lactate, and cholesterol. The solid lines show the corresponding linear parts of the calibration curves.*

it sensitively quantifies the current flowing in the channel (I_D, drain current), in response to a change (V_{GS}, gate voltage), and is thus a measure of the "efficiency" of transduction of a biological event. Rivnay et al. recently demonstrated that the transconductance of an OECT can be tuned by not only changing the channel geometry but also the conducting polymer film thickness [Rivnay, 2013]. We customized the channel geometry in order to obtain the highest transconductance value at the applied gate bias of 0.1 V to 0.2 V, which coincides with the working potential of our enzymatic sensors (0.2 V). Figure 2.4a shows the transfer characteristics of such an OECT before and after the gate biofunctionalization. These characteristics demonstrate typical low-voltage operation ($V_{GS}, V_{DS} < |1\,V|$) in the depletion mode. The corresponding g_m exhibits its maximum value of 16 mS at $V_{GS} = 0.15$ V and $V_{DS} = -0.6$ V. Notably, the biofunctionalization process does not lead to any significant alterations in the device performance.

For the calculation of sensitivity and linear range, two vital indicators of the sensing performance of any sensor, chronoamperometric (CA) measurements were performed on

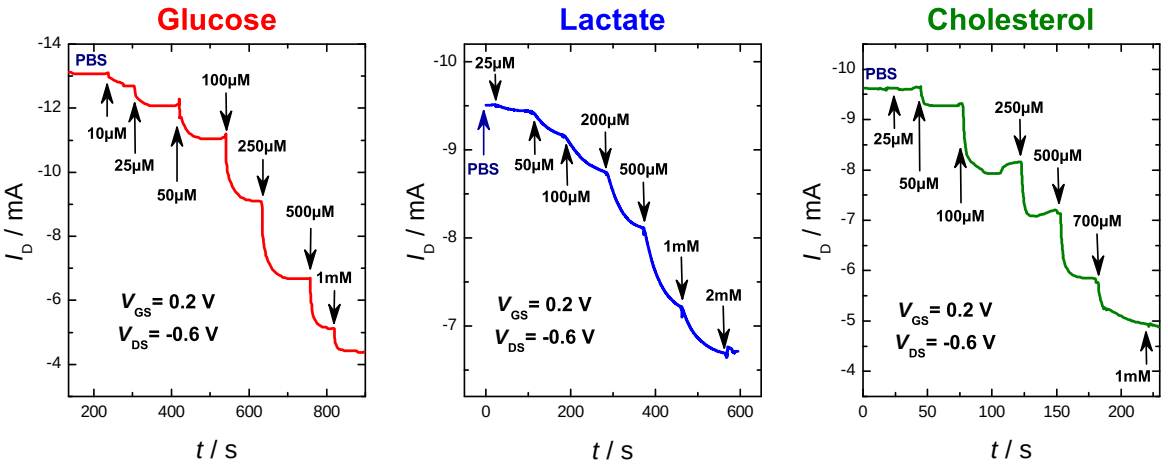

Figure 2.5: *Typical chronoamperometric responses of the three analyte-specific OECTs after successive additions of increasing concentrations of the corresponding analytes.*

the differently functionalized transistors after successive additions of increasing concentrations of corresponding analytes. Figure 2.4b-d show the calibration curves, deduced from the CA measurements after performing each experiment at least three times. In order to compare the responses of different devices, the current outputs were normalized as described in the Experimental Section. The raw data for representative devices are shown in Figure 2.5.

The logarithmic plot of current response vs. analyte concentration yields a linear behavior in the concentration range of 0.02 mM to 1 mM for glucose, 0.01 mM to 2 mM for lactate and 0.01 mM to 0.7 mM for cholesterol, while all coincide with the corresponding physiological levels in saliva, ranging typically from 0.1 mM to 0.5 mM, 0.1 mM to 2.5 mM and 0.1 mM to 0.45 mM of glucose, lactate, and cholesterol respectively [Malon, 2014]. The OECTs show excellent sensitivities in the µM range and lower limits of quantification (LOQ) of 10 µM for glucose, 50 µM for lactate, and 10 µM for cholesterol as determined from the calibration curves.

For the bio-sample tested here, we show detection in the relevant physiological range, however as might be expected, changes in the enzyme loading can be used as a method to alter the dynamic range [Dúrso, 1993]. Upon increasing the enzyme loading, we observed no noticeable change in the biosensors' analytical characteristics, probably due to limitations in the diffusion of the analytes. After a certain threshold of enzyme concentration, the response of the device became relatively independent of changes in enzyme activity, an observation that is in accordance with previous studies [Dúrso, 1993]. We determined the critical enzyme concentrations for the three different enzymes and used it throughout as described in the Experimental Section. Increasing the CS-Fc concentration in our biocomplex on the other hand resulted in a significant shift towards

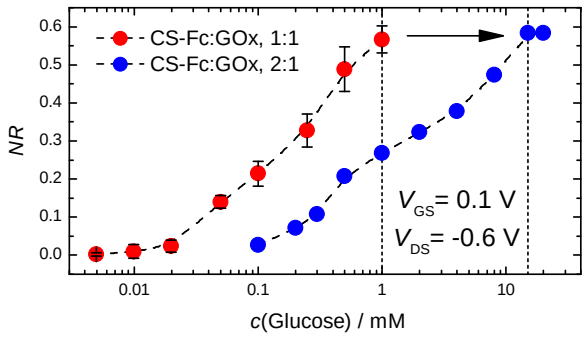

Figure 2.6: *Comparative calibration curves of glucose with different enzyme: mediator ratio.*

higher upper limits in the linear range (Figure 2.6). This is attributed to an increase in the CS film thickness, which acts as a diffusion limiting barrier for the analyte. However, the increase of the CS film thickness inevitably extends the response time of the device. Overall, by fine tuning the enzyme/mediator complex loading we can rather easily adjust our sensor's analytical characteristic to the needs of a specific analytical task.

2.2.3 Selective Multianalyte Detection in Complex Media Using the OECT Array

In this work an array of analyte specific OECTs, operated in a common electrolyte, i.e., the relevant biological sample, was fabricated, therefore electrical crosstalk between the different transistors was typically an issue to troubleshoot. In a common-source configuration and in the presence of a common electrolyte, the individual transistor gating will induce changes in each of the separate sensing circuits due to polarization. To circumvent this issue, we ensured a closed electrical loop for each of the sensors by isolating the individual grounds (in our case the source) as shown schematically in Figure 2.7a. The current output of two adjacent transistors in the same electrolyte after a DC sequential pulsing at the gate electrode of each OECT demonstrated no evidence of electrical cross-talk between individual OECTs (Figure 2.7b). Figure 2.7c shows the normalized current response of the three differently functionalized transistors operated simultaneously after successive additions of the corresponding analytes in known concentrations. Each device operates independently and specifically for the relevant analyte, without any biological crosstalk. When a mixture containing all analytes was added on the OECT array, the current-response times of each transistor differed. This can be related to the spatial position of each device with respect to the central addition of the metabolite mixture as well the different kinetic properties of each enzyme (Figure 2.7d).

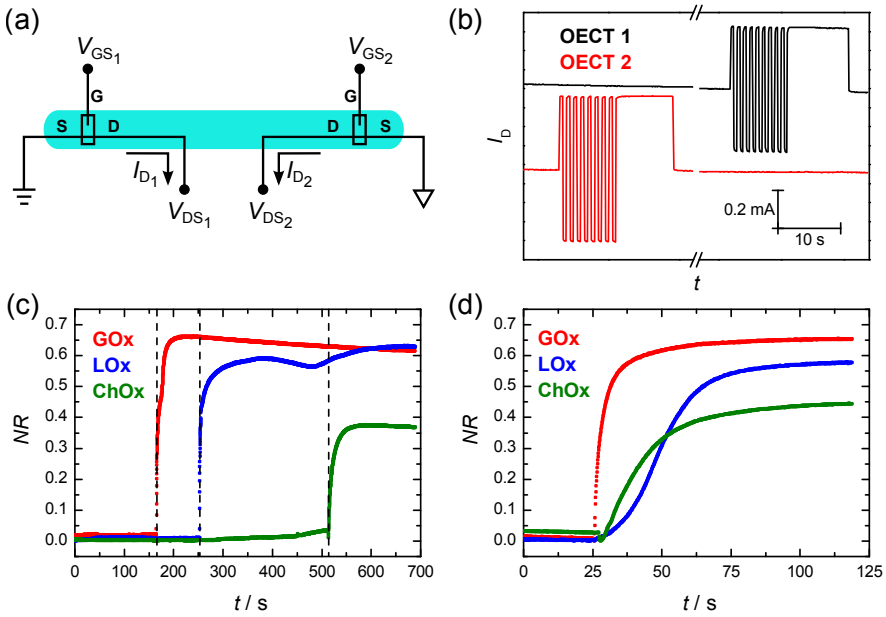

Figure 2.7: *Selective multianalyte detection in complex media using the OECT array. (a) A schematic circuit diagram of two OECTs on the array. (b) CA response of the channels of two OECTs after sequential pulsing of the gates showing the absence of electrical cross-talk. (c-d) CA response of three differently functionalized OECTs after successive additions of known concentrations of the three analytes (c) and addition of a mixture of the three analytes (d).*

2.2.4 On-Chip Multianalyte Detection in Saliva Using the OECT Array

The use of biological samples such as blood and saliva is known to increase background interference. One strategy used predominantly in in vivo biosensing applications to improve biosensor signal-to-noise ratio (SNR) with respect to electrochemical interference present in biological media, is the use of a "blank electrode." This identical electrode that lacks the selectivity toward a specific analyte is utilized in extracting any background signal related to unspecific reactions and thus to improve the sensitivity of the biosensor [Schabmueller, 2006; Weltin, 2014]. To this end, we incorporated an extra OECT into the microarrays, which was functionalized with a non-specific protein, BSA. Interference studies with respect to the detectable analytes were also performed with our reference transistor to further ensure specificity and sensitivity of our system. The device showed no response to the presence of these analytes in the medium, further confirming its non-specific nature (data not shown).

Furthermore, we integrated a versatile, portable, and easy-to-use "human-powered", PDMS-based microfluidic in the OECT array. Microfluidics allow for laminar flow, ultra-small sample volumes, faster analysis, portability, miniaturization, and automa-

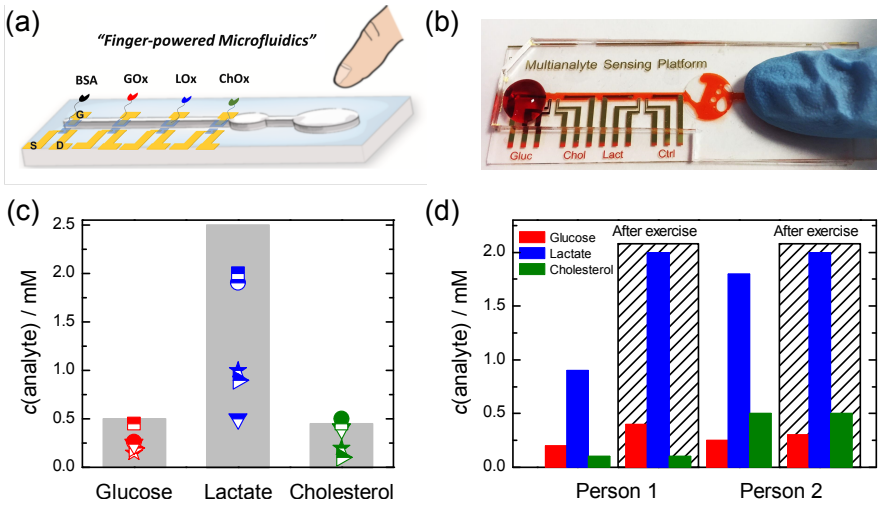

Figure 2.8: *Selective multianalyte detection in complex media using the OECT array. (a) Schematic illustration of the biosensing multiplatform with the embedded "finger-powered" PDMS microfluidic showing the activation "button" (1), the liquid reservoir (2), and the punched inlet (3). (b) Photograph of the actual device used for the measurements, showing a red-colored solution that was pressure-driven from the inlet through the sensing areas, as indicated by the arrow. (c) Salivary metabolite levels of five healthy volunteers as measured with our setup (the grey shaded areas represent the physiological ranges of concentrations for each analyte). (d) Relative salivary metabolite variations of two healthy volunteers before and after intense physical exercise.*

tion [Nahavandi, 2014]. In our approach, the human finger, serving as the pumping actuation force, provides the pressure to drive the liquid inside the microchannel [Iwai, 2011]. The microfluidic device consists of a straight channel and two large round areas (Figure 2.8a). Simply, the larger round area is used as the activation "button" for the microfluidics by depressing the PDMS layer. The applied pressure results in a decrease in the total volume of the microchannel. After pipetting the specimen on top of the punched inlet, the pressure is released and the liquid starts to flow inside the microchannel due to re-expansion. Since this process is reversible, the smaller round region is used as a liquid reservoir (dead volume) to avoid complete emptying of the microchannel, which can result in faulty operation of the transistors. In our experience as long as sufficient pressure is applied to achieve fluid transfer, the exact amount of pressure applied is not critical. It should be mentioned that physiological solution (PBS) was flowed in all the experiments prior to the detection media in order to obtain our baseline and thus avoid any possible signal misinterpretation due to contamination from the previous samples. A photograph of the resulting portable biosensing set up embedded within the microfluidic is provided in Figure 2.8b. Although the measurement set up utilized herein is a custom, lab-based multivalent measuring system

(described in the Experimental section), which is not portable, once specific requirements are outlined for electronic acquisition, portable embedded electronics can be tailored to the application at hand to be compatible with POCT.

It is believed that salivary metabolite levels can reflect the corresponding blood concentrations since saliva is an ultra-filtrate of plasma. In particular, most metabolites can be detected in saliva due to their passive diffusion from blood and subsequent secretion from salivary glands [Aguirre, 1993; Kim, 2014]. Figure 2.8c shows the salivary metabolite levels of five healthy volunteers as measured by our device. For the calculation of the analyte concentrations, the current normalized responses of the OECTs were correlated with the calibration curves for each metabolite, shown in Figure 2.4b-d. All metabolite levels were found to be within the physiological range (shaded areas in the graph), indicating the relevance of the measurements. In order to examine the relative variations of those metabolites under different physiological conditions, we collected samples from two healthy volunteers before and after intense physical exercise and the results are summarized in Figure 2.8d. Monitoring of metabolite levels in sports medicine has been extensively employed as a means of determining the athlete's health status during exercise. Lactate is a crucial intermediary in numerous cellular, localized and whole body metabolic processes and the balance of its production and removal is highly dependent on a multitude of parameters. Lactate is known to be formed by skeletal muscle when the rate of glycolysis exceeds the metabolic rate of the citric acid cycle and oxidative phosphorylation (i.e., during intense exercise). However, given the multivariate mechanisms of energy metabolism that are involved, the levels of other associated metabolites need to be concurrently measured in order to obtain a more holistic understanding of the rather complicated bioenergetic pathways. With our platform we anticipate meeting such requirements that can facilitate simultaneous identification of informative biomarkers in particular healthcare applications.

2.3 Conclusions

In this work, key challenges in continuous multi-analyte biosensing such as analyte specificity and elimination of electrical and biological cross-talk were successfully addressed. A multiplexed OECT platform integrated with a portable "finger-powered" microfluidic was developed, allowing for the detection of several critical biomarkers simultaneously. Measurements were performed with this prototype device in human saliva, to detect three clinically relevant biomarkers, glucose, lactate, and cholesterol. The biosensors achieved excellent analytical performance with detection ranges that covered the physiological ranges in saliva. This versatile and easy-to-handle platform enables the implementation of any type of enzymatic biosensors toward accurate, rapid, non-invasive, and portable next-generation healthcare monitoring. Finally, the solu-

tion processability of our main material (PEDOT:PSS) and the simple planar fully integrated design renders the process easily scalable for high throughput production of disposable sensors.

2.4 Experimental Section

Device Fabrication The devices are fabricated photolithographically using a parylene C lift-off process [Sessolo, 2013]. Patterned gold lines served as source, drain, and gate electrodes. PEDOT:PSS blended with PVA was employed as the active layer of the OECT and also deposited on the gate. The overall device architecture consists of four, µm-sized OECTs, each with a channel of width-to-length (W/L) of 100/10 (µm/µm) and a planar gate of 500 µm × 500 µm. The metal contacts and interconnects were patterned using Shipley 1813 photoresist, exposed to UV light with a SUSS MJB4 contact aligner, developed in MF-26 followed by thermal evaporation of chromium (10 nm) and gold (100 nm) and metal lift-off in acetone/isopropanol. Two, 2 µm thick parylen C layers (SCS Coating) separated by an anti-adhesive (industrial cleaner, Micro-90) were successively deposited using a SCS Labcoater 2. The first parylene layer was attached to the substrate using 3 (trimethoxysilyl)propyl methacrylate (A-174 Silane) as an adhesion promoter. For the patterning of the PEDOT:PSS channel, AZ9260 photoresist was spin casted, exposed, and developed in AZ developer (AZ Electronic Materials) followed by reactive ion etching by O_2 plasma (Oxford 80 Plasmalab plus) of the unprotected layers of parylene. For the deposition of the PEDOT:PSS/PVA films, a formulation of the commercial aqueous dispersion PH-1000 (Heraeus Clevios GmbH), consisting of 5 % v/v ethylene glycol, 0.4 % v/v dodecyl benzene sulfonic acid and 25 wt% of polyvinyl alcohol was sonicated before spin-casting (2500 rpm, 35 s, for a thickness of 90 nm). The resulting devices were subsequently baked at 110 °C for 1 h followed by 2 rinsing/soaking cycles in deionized water to remove any excess of low-molecular-weight compounds.

Device Functionalization For the gate electrode functionalization, 3 glycidoxy-propyltrimethoxysilane (GOPS) was deposited by vapor deposition at 90 °C for 1 h under vacuum and baked after washing with ethanol (15 s), for the formation of the epoxy-modified gate electrode surface. The three enzyme solutions were prepared in PBS (phosphate buffered saline) in their optimum concentrations, 2 mg mL^{-1} for glucose oxidase (from *Aspergillus Niger*, ≥ 100 U mg^{-1}, Sigma) 10 mg mL^{-1} lactate oxidaze (from *Aerococcus viridans*, ≥ 55 U mg^{-1}, Roche) and 5 mg mL^{-1} for cholesterol oxidase (from *Streptomyces sp.*, ≥ 20 U mg^{-1}, Sigma). Chitosan–Ferrocene (CS-Fc) 4 mg mL^{-1} was diluted in a 1 % v/v acetic acid aqueous solution. Prior to CS-Fc/enzyme complex formation, the enzyme solutions were mixed with EDC:NHS (1:1) 100 mM in 2-(N-

morpholino)ethanesulfonic acid (MES) buffering agent in a 4:1 enzyme:reaction mixture ratio and left for 30 min to react. Subsequently, the CS-Fc/enzyme complex was formed by mixing the activated enzyme solution with the CS-Fc solution in a 1:1 ratio and left for 30 min. Following that, the mixture was drop-casted selectively onto the epoxy-modified gate electrodes and left overnight in a humid environment to avoid evaporation.

Device Characterization All characterization was performed in PBS. The cyclic voltammograms of the biofunctionalized electrodes were recorded using a potentiostat-galvanostat (Autolab, PGSTAT128N) with a Ag/AgCl reference electrode and a platinum counter electrode. The electrical characterization of the OECT (IV curves and calibration curves) was performed using a Keithley 2612A dual SourceMeter with customized LabVIEW software. The chronoamperometric measurements were recorded using a National Instruments PXIe-1062Q system. For this, the channel and the gate of the OECT were biased using an isolated analog output model, NI PXIe-4322, with 300 V CAT II channel to channel isolation. The current output of each OECT was recorded with a separate digital multimeter card, PXI-4071, mounted in the same chassis. A customized LabVIEW software was used to address each hardware component.

Chronoamperometric Measurements for Calibration of Metabolites and Multi-analyte Testing Glucose and lactate were dissolved as stock solutions in PBS, while cholesterol was dissolved in a 1X PBS solution containing 2 % v/v Triton X-100, followed by gentle heating until a clear solution was obtained. The stock analyte solutions were subsequently diluted in PBS to perform calibration curves. Each measurement was conducted by subsequent additions of increasing concentrations of the analyte solutions after baseline (steady current) in PBS was reached on our devices. The readout signal at zero analyte concentration is determined by the steady current obtained in PBS solution. The device response for each metabolite concentration was subtracted after the current output reached steady state and was normalized according to the following equation:

$$NR = \left| \frac{I_{\text{conc}} - I_{\text{conc=0}}}{I_{\text{conc=0}}} \right| \quad , \tag{2.1}$$

where $I_{\text{conc=0}}$, I_{conc} are the current outputs in the absence of any analyte (baseline) and after the addition of a specific concentration of analyte, respectively. For multi-analyte measurements in PBS or saliva, the transistors were operated simultaneously and current outputs of each transistor were recorded individually with a separate digital multimeter card as described above. In the particular case of saliva samples, our background signal is given by the readout signal (current output) of the control device (BSA-functionalized device) in the presence of the saliva.

Microfluidic Fabrication The fabrication of the microfluidics master mold was carried out by pasting a 50 µm thick double-sided pressure sensitive adhesive film, PSA (AR8890, Adhesives Research, Ireland) onto a plastic petri dish. The desired microfluidic pattern was created by cutting the PSA with a cutting plotter (Large Flatbed plotter–FC2250 series). For the formation of the polydimethylsiloxane (PDMS) microfluidics, PDMS was prepared by mixing PDMS elastomer with the curing agent from Sylgard 184 kit at a weight ratio of 10:1. After mixing and centrifugation, the PDMS was poured onto the master mold, and cured in an oven at 60 °C overnight. Following curing, the PDMS layer was peeled from the master and the inlet was made using a metal punch (2 mm in diameter). Finally, the PDMS microfluidics was placed on top of the OECTs device that were previously fabricated and functionalized on conventional microscope glass slide. Using an optical microscope, successful alignment of the microchannel and the OECTs was performed.

Saliva Sampling Saliva samples were collected from 15 healthy volunteers and 5 of them were randomly chosen for the experiments. Saliva sampling was performed at fasting conditions (at least 3 h) using a direct expectoration method the so called "spitting method". Subjects were asked to collect saliva in their mouths and to spit it into a sterile plastic tube with a diameter of 6 cm for 5 min, based on existing protocol [Nagler, 2005]. Saliva sampling was done according to ethics principles set out by the biosafety committee at Ecole des Mines de St. Etienne and consent forms were signed by all donors.

References

[Aguirre, 1993] A. Aguirre, L. A. Testa-Weintraub, J. A. Banderas, G. G. Haraszthy, M. S. Reddy, and M. J. Levine: "*Sialochemistry: A Diagnostic Tool?*", Critical Reviews in Oral Biology & Medicine **4** (1993), p. 343.

[Arya, 2008] S. K. Arya, M. Datta, and B. D. Malhotra: "*Recent advances in cholesterol biosensor*", Biosensors and Bioelectronics **23** (2008), pp. 1083–1100.

[Bernards, 2007] D. A. Bernards and G. G. Malliaras: "*Steady-State and Transient Behavior of Organic Electrochemical Transistors*", Advanced Functional Materials **17** (23, 2007), pp. 3538–3544.

[Bernards, 2008] D. A. Bernards, D. J. Macaya, M. Nikolou, J. A. DeFranco, S. Takamatsu, and G. G. Malliaras: "*Enzymatic sensing with organic electrochemical transistors*", J. Mater. Chem. **18** (2008), pp. 116–120.

[Dúrso, 1993] E. Dúrso and P. Coulet: "*Effect of enzyme ratio and enzyme loading on the performance of a bienzymatic electrochemical phosphate biosensor*", Analytica Chimica Acta **281** (1993), pp. 535–542.

[Fernández, 2005] L. Fernández and H. Carrero: "*Electrochemical evaluation of ferrocene carboxylic acids confined on surfactant–clay modified glassy carbon electrodes: oxidation of ascorbic acid and uric acid*", Electrochimica Acta **50** (2005), pp. 1233–1240.

[Iwai, 2011] K. Iwai, R. D. Sochol, and L. Lin: "*Finger-powered, pressure-driven microfluidic pump*", (2011), pp. 1131–1134.

[Kergoat, 2014] L. Kergoat, B. Piro, D. T. Simon, M.-C. Pham, V. Noël, and M. Berggren: "*Detection of Glutamate and Acetylcholine with Organic Electrochemical Transistors Based on Conducting Polymer/Platinum Nanoparticle Composites*", Advanced Materials **26** (2014), pp. 5658–5664.

[Khodagholy, 2012] D. Khodagholy, V. F. Curto, K. J. Fraser, M. Gurfinkel, R. Byrne, D. Diamond, G. G. Malliaras, F. Benito-Lopez, and R. M. Owens: "*Organic electrochemical transistor incorporating an ionogel as a solid state electrolyte for lactate sensing*", Journal of Materials Chemistry **22** (2012), p. 4440.

[Khodagholy, 2013] D. Khodagholy, J. Rivnay, M. Sessolo, M. Gurfinkel, P. Leleux, L. H. Jimison, E. Stavrinidou, T. Herve, S. Sanaur, R. M. Owens, and G. G. Malliaras: "*High transconductance*

organic electrochemical transistors", Nature Communications **4** (12, 2013), p. 2133.

[Kim, 2014] J. Kim, G. Valdés-Ramírez, A. J. Bandodkar, W. Jia, A. G. Martinez, J. Ramírez, P. Mercier, and J. Wang: "*Non-invasive mouthguard biosensor for continuous salivary monitoring of metabolites*", The Analyst **139** (2014), p. 1632.

[Kumar, 2013] S. Kumar, S. Kumar, M. A. Ali, P. Anand, V. V. Agrawal, R. John, S. Maji, and B. D. Malhotra: "*Microfluidic-integrated biosensors: Prospects for point-of-care diagnostics*", Biotechnology Journal **8** (2013), pp. 1267–1279.

[Lanzani, 2014] G. Lanzani: "*Materials for bioelectronics: Organic electronics meets biology*", Nature Materials **13** (22, 2014), pp. 775–776.

[Lee, 2009] Y.-H. Lee and D. T. Wong: "*Saliva: an emerging biofluid for early detection of diseases*", American Journal of Dentistry **22** (2009), p. 241.

[Liao, 2015] C. Liao, C. Mak, M. Zhang, H. L. W. Chan, and F. Yan: "*Flexible Organic Electrochemical Transistors for Highly Selective Enzyme Biosensors and Used for Saliva Testing*", Advanced Materials **27** (2015), pp. 676–681.

[Lin, 2010] P. Lin, F. Yan, and H. L. W. Chan: "*Ion-Sensitive Properties of Organic Electrochemical Transistors*", ACS Applied Materials & Interfaces **2** (23, 2010), pp. 1637–1641.

[Liu, 2012] Y. Liu, Z. Matharu, M. C. Howland, A. Revzin, and A. L. Simonian: "*Affinity and enzyme-based biosensors: recent advances and emerging applications in cell analysis and point-of-care testing*", Analytical and Bioanalytical Chemistry **404** (2012), pp. 1181–1196.

[Mabeck, 2005] J. T. Mabeck, J. A. DeFranco, D. A. Bernards, G. G. Malliaras, S. Hocdé, and C. J. Chase: "*Microfluidic gating of an organic electrochemical transistor*", Applied Physics Letters **87** (2005), p. 013503.

[Malon, 2014] R. S. P. Malon, S. Sadir, M. Balakrishnan, and E. P. Córcoles: "*Saliva-Based Biosensors: Noninvasive Monitoring Tool for Clinical Diagnostics*", BioMed Research International **2014** (2014), pp. 1–20.

[Nagler, 2005] R. M. Nagler and O. Hershkovich: "*Relationships between age, drugs, oral sensorial complaints and salivary profile*", Archives of Oral Biology **50** (2005), pp. 7–16.

[Nahavandi, 2014] S. Nahavandi, S. Baratchi, R. Soffe, S.-Y. Tang, S. Nahavandi, A. Mitchell, and K. Khoshmanesh: "*Microfluidic plat-*

forms for biomarker analysis", Lab on a Chip **14** (2014), p. 1496.

[Quignard, 2000] F. Quignard, A. Choplin, and A. Domard: "*Chitosan: A Natural Polymeric Support of Catalysts for the Synthesis of Fine Chemicals*", Langmuir **16** (2000), pp. 9106–9108.

[Rivnay, 2013] J. Rivnay, P. Leleux, M. Sessolo, D. Khodagholy, T. Hervé, M. Fiocchi, and G. G. Malliaras: "*Organic Electrochemical Transistors with Maximum Transconductance at Zero Gate Bias*", Advanced Materials **25** (2013), pp. 7010–7014.

[Rivnay, 2015] J. Rivnay, M. Ramuz, P. Leleux, A. Hama, M. Huerta, and R. M. Owens: "*Organic electrochemical transistors for cell-based impedance sensing*", Applied Physics Letters **106** (26, 2015), p. 043301.

[Schabmueller, 2006] C. Schabmueller, D. Loppow, G. Piechotta, B. Schütze, J. Albers, and R. Hintsche: "*Micromachined sensor for lactate monitoring in saliva*", Biosensors and Bioelectronics **21** (2006), pp. 1770–1776.

[Scheiblin, 2015] G. Scheiblin, A. Aliane, X. Strakosas, V. F. Curto, R. Coppard, G. Marchand, R. M. Owens, P. Mailley, and G. G. Malliaras: "*Screen-printed organic electrochemical transistors for metabolite sensing*", MRS Communications **5** (2015), pp. 507–511.

[Sessolo, 2013] M. Sessolo, D. Khodagholy, J. Rivnay, F. Maddalena, M. Gleyzes, E. Steidl, B. Buisson, and G. G. Malliaras: "*Easy-to-Fabricate Conducting Polymer Microelectrode Arrays*", Advanced Materials **25** (18, 2013), pp. 2135–2139.

[Sessolo, 2014] M. Sessolo, J. Rivnay, E. Bandiello, G. G. Malliaras, and H. J. Bolink: "*Ion-Selective Organic Electrochemical Transistors*", Advanced Materials **26** (2014), pp. 4803–4807.

[Shim, 2009] N. Y. Shim, D. A. Bernards, D. J. Macaya, J. A. DeFranco, M. Nikolou, R. M. Owens, and G. G. Malliaras: "*All-Plastic Electrochemical Transistor for Glucose Sensing Using a Ferrocene Mediator*", Sensors **9** (4, 2009), pp. 9896–9902.

[Simon, 2009] D. T. Simon, S. Kurup, K. C. Larsson, R. Hori, K. Tybrandt, M. Goiny, E. W. H. Jager, M. Berggren, B. Canlon, and A. Richter-Dahlfors: "*Organic electronics for precise delivery of neurotransmitters to modulate mammalian sensory function*", Nature Materials **8** (2009), pp. 742–746.

[Strakosas, 2014] X. Strakosas, M. Sessolo, A. Hama, J. Rivnay, E. Stavrinidou, G. G. Malliaras, and R. M. Owens: "*A facile biofunctionalisation route for solution processable conducting polymer devices*", J. Mater. Chem. B **2** (2014), pp. 2537–2545.

[Strakosas, 2015] X. Strakosas, M. Bongo, and R. M. Owens: "*The organic electrochemical transistor for biological applications*", Journal of Applied Polymer Science **132** (15, 2015), p. 41735.

[Tang, 2011] H. Tang, F. Yan, P. Lin, J. Xu, and H. L. W. Chan: "*Highly Sensitive Glucose Biosensors Based on Organic Electrochemical Transistors Using Platinum Gate Electrodes Modified with Enzyme and Nanomaterials*", Advanced Functional Materials **21** (21, 2011), pp. 2264–2272.

[Torsi, 2013] L. Torsi, M. Magliulo, K. Manoli, and G. Palazzo: "*Organic field-effect transistor sensors: a tutorial review*", Chemical Society Reviews **42** (2013), p. 8612.

[Tria, 2014] S. A. Tria, M. Ramuz, L. H. Jimison, A. Hama, and R. M. Owens: "*Sensing of Barrier Tissue Disruption with an Organic Electrochemical Transistor*", Journal of Visualized Experiments (10, 2014).

[Turner, 2000] A. P. F. Turner: "*Biosensors-Sense and Sensitivity*", Science **290** (17, 2000), pp. 1315–1317.

[Wan, 2013] Y. Wan, Y. Su, X. Zhu, G. Liu, and C. Fan: "*Development of electrochemical immunosensors towards point of care diagnostics*", Biosensors and Bioelectronics **47** (2013), pp. 1–11.

[Wang, 2013] C. Wang: "*The Relationship between Type 2 Diabetes Mellitus and Related Thyroid Diseases*", Journal of Diabetes Research **2013** (2013), pp. 1–9.

[Weltin, 2014] A. Weltin, J. Kieninger, B. Enderle, A.-K. Gellner, B. Fritsch, and G. A. Urban: "*Polymer-based, flexible glutamate and lactate microsensors for in vivo applications*", Biosensors and Bioelectronics **61** (2014), pp. 192–199.

[Willner, 2002] I. Willner, B. Willner, and E. Katz: "*Functional biosensor systems via surface-nanoengineering of electronic elements*", Reviews in Molecular Biotechnology **82** (2002), pp. 325–355.

[Wilson, 2005] G. S. Wilson and R. Gifford: "*Biosensors for real-time in vivo measurements*", Biosensors and Bioelectronics **20** (2005), pp. 2388–2403.

[Yang, 2007] W. Yang, H. Zhou, and C. Sun: "*Synthesis of Ferrocene-Branched Chitosan Derivatives: Redox Polysaccharides and their Application to Reagentless Enzyme-Based Biosensors*", Macromolecular Rapid Communications **28** (2, 2007), pp. 265–270.

[Yang, 2009] S. Y. Yang, J. A. DeFranco, Y. A. Sylvester, T. J. Gobert, D. J. Macaya, R. M. Owens, and G. G. Malliaras: "*Integration of a surface-directed microfluidic system with an*

organic electrochemical transistor array for multi-analyte biosensors", Lab on a Chip **9** (2009), pp. 704–708.

Chapter 3

Voltage Amplifier Based on Organic Electrochemical Transistor

This chapter is based on the publication:

"Voltage Amplifier Based on Organic Electrochemical Transistor"
M. Braendlein, T. Lonjaret, P. Leleux, J-M. Badier, G. G. Malliaras
Advanced Science, Volume 4, Issue 1, DOI:10.1002/advs.201600247 (2016).

Organic electrochemical transistors (OECTs) are receiving a great deal of attention as amplifying transducers for electrophysiology. A key limitation of this type of transistors, however, lies in the fact that their output is a current, while most electrophysiology equipment requires a voltage input. We build and model a simple circuit that uses a drain resistor to produce a voltage output. We show that operating the OECT in the saturation regime provides increased sensitivity while maintaining a linear signal transduction. We demonstrate that this circuit provides high quality recordings of the human heart using readily available electrophysiology equipment, paving the way for the use of OECTs in the clinic.

3.1 Introduction

Historically, electrophysiological activity has been recorded with amplifiers using cutaneous or implanted electrodes to pick up the biological signal and dates back to the work of Einthoven in 1901 [RiveraRuiz, 2008]The displacement of ionic charge inside biological tissues during heart or neuronal activity builds up a voltage which can be read with low impedance electrodes [Buzsáki, 2012]. However, on the way to the amplifier, this biological information is disturbed by ambient noise such as the characteristic AC signal from the building's power supply [Webster, 1984]. This can become particularly challenging in environments such as an operating theater in a hospital where strong lights, space limitations and sophisticated medical tools provide high electrical noise. This is compounded by the fact that the amplitude of electrophysiological signals is typically very low. One way to bypass such problems is to use active transducing amplifiers that are in direct contact with the biological medium. This provides a first stage amplification at the recording site, making the signal less sensitive to further noise pickup.

A promising candidate for such a transducing amplifier is the electrolyte gated organic electrochemical transistor (OECT) [Kittlesen, 1984], a three terminal device with key properties such as low operation voltage [Nilsson, 2002a], high transconductance [Khodagholy, 2013b] and biocompatibility [Isaksson, 2007]. The use of the conducting polymer poly(3,4-ethylenedioxythiophene) doped with poly(styrene sulfonate) (PEDOT:PSS) as active material leads to an improved bioelectronic interface [Rivnay, 2014] and recent studies have attributed this fact to the mixed ionic and electronic conduction [Rivnay, 2015] where ions are able to penetrate into the bulk of the material [Stavrinidou, 2013]. Easy fabrication with low temperature processing techniques, such as photolithography [Sessolo, 2013], screen printing [Andersson, 2002] or inkjet printing [Basiricò, 2012] provide a future perspective for large scale manufacturing of flexible, disposable [Nilsson, 2002b] and reasonably priced sensor devices on a broad range of substrates [Stavrinidou, 2015]. As such, the OECT has proven worthy in various biosensing scenarios, e.g. *in vitro* detection of ions [Sessolo, 2014], specific metabolites [Tang, 2011] and nucleotides [Lin, 2011], real-time monitoring of barrier tissue integrity [Ramuz, 2014] and *in vivo* recordings of electrophysiological activity [Khodagholy, 2013a].

The OECT in its regular configuration, i.e. a constant source drain bias and a gate that is connected to the source and immersed in an electrolyte covering the active material, provides a drain current I_{D} that is modulated by the gate voltage V_{GS}. Cations injected in the active material upon applying a positive gate voltage compensate sulfonate anions on the PSS chain, thus reducing the number of holes in the film by electrochemically dedoping the conducting polymer [Yuen, 2007]. Campana et al. demonstrated a direct cutaneous implementation of an OECT on resorbable bioscaffold for tran-

sient applications in electrocardiographic (ECG) recordings [Campana, 2014]. This way, the amplifing transducer is brought directly to the site of interest, reducing the power-line interference and allowing for an increased signal-to-noise ratio comparable to regular electrode measurements. In order to maintain high quality recordings for long-term measurements, as needed for example in sports applications [Coyle, 2010] or telemedicine situations [Fensli, 2005; Pantelopoulos, 2010], hydrogels or ionic liquid gels [Yi, 2015] are used to establish a better contact of electrophysiology devices with the skin. This reduces motion artifacts and maintains or lowers the impedance [Takamatsu, 2015].

To make the OECT compatible with existing voltage recording equipment for electrophysiological measurements, we need to convert the current output into a voltage signal. In this article, we focus on the integration of the OECT into a simple voltage amplifier circuit to provide a voltage-to-voltage transduction, as first introduced by Rivnay et al. [Rivnay, 2013]. A detailed investigation of this system allows us to optimize the amplification parameters of the device. We find an increased performance when biasing the OECT in the saturation regime with a linear amplification of up to 30 V/V. To validate our system, we demonstrate recordings of electrocardiographic signals with a regular medical recording system. This work leads to a better understanding of OECT-based circuits and paves the way for their use as active organic electrodes with traditional electrophysiology instrumentation.

3.2 Results and Discussion

To convert the current provided by the OECT into a readable voltage signal V_{out} we use a load resistor R_{load} on the drain side of the OECT (see Figure 3.1a). This acts as a voltage divider for the supply voltage V_{supply} and lets the drain voltage V_{out} of the OECT float, i.e. there is no fixed source drain bias anymore. Instead, the bias depends on the drain current

$$V_{\mathrm{out}} = V_{\mathrm{supply}} - R_{\mathrm{load}} \cdot I_{\mathrm{D}}\left(V_{\mathrm{GS}}, V_{\mathrm{out}}\right) \quad , \tag{3.1}$$

which itself depends on both the gate voltage as well as the source drain bias. Therefore, a modulation on the gate can be related to a change in the output voltage and a voltage-to-voltage transduction is achieved. For each gate voltage there is one specific output voltage and this so called operation point (*OP*) depends on the drain load as well as the supply voltage. By solving Equation (3.1) for I_{D} and plotting this so called load line on top of the IV curve one obtains a load line diagram and can immediately extract the operation point at the intersection of the two curves (see Figure 3.1b). Since the effective source drain bias of the device varies linearly with the drain current, the resulting transconductance $g_{\mathrm{m}} = {}^{\partial I_{\mathrm{D}}}/_{\partial V_{\mathrm{GS}}}$ is also altered. We distinguish between

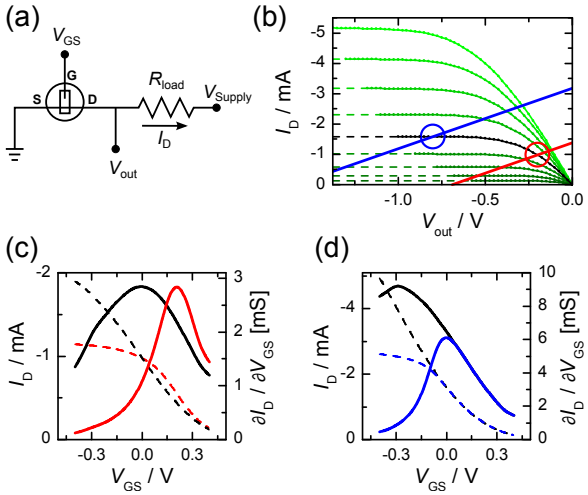

Figure 3.1: *(a) Schematic circuit layout of the voltage amplifier system with embedded OECT. (b) Load line diagram of an OECT with aspect ratio of $W/L = 2$ and thickness of $d = 70\,\text{nm}$ using a drain load resistor of $R_{load} = 500\,\Omega$ for saturation regime (blue) and linear regime (red). A 100 mM solution of sodium chloride is used as electrolyte. The gate voltage is varied from $V_{GS} = +0.4\,\text{V}$ (light green) to $-0.4\,\text{V}$ (dark green) in steps of $\Delta V_{GS} = 0.1\,\text{V}$. The black line indicates the output at $V_{GS} = 0\,\text{V}$ and the open circles denote the corresponding operation point. The dashed lines are a guide to the eye and extend the saturation regime to the inaccessible data points assuming that the drain currents fully saturates. (c-d) Transfer curve (dashed line) and transconductance (solid line) of the unloaded (black) versus the loaded OECT (colored) for linear regime (c) and saturation regime (d). The values of the drain current are extracted graphically via the intersection of the load line with the output curve at each value of V_{GS}.*

the linear and the saturation regime of the OECT, the chosen operation points at $V_{\text{GS}} = 0\,\text{V}$ are $OP_{\text{lin}} = -0.2\,\text{V}$ and $OP_{\text{sat}} = -0.8\,\text{V}$ respectively (see Figure 3.1c-d). It can be seen that in the linear regime, the peak transconductance compared to a device without drain load is shifted towards a higher positive gate voltage and consequently the transconductance at $V_{\text{GS}} = 0\,\text{V}$ drops by more than 50 %. On the other hand, in the saturation regime the transconductance is identical to an unloaded device for positive gate voltages and only deviates for negative gate voltages. This is due to the fact that at negative gate voltages, the drain current increases and in consequence the source drain bias decreases until the OECT operates back in the linear regime. Considering the amplitude of regular electrophysiological signals (in the order of µV to mV), we are mainly interested in small changes of the gate voltage around $V_{\text{GS}} = 0\,\text{V}$. Hence, operating the device in the saturation regime is favourable as it provides good transduction.

In analogy to the findings of Chou et al. [Chou, 1987], we can derive a relationship between the transconductance of the loaded and the unloaded device, using the differ-

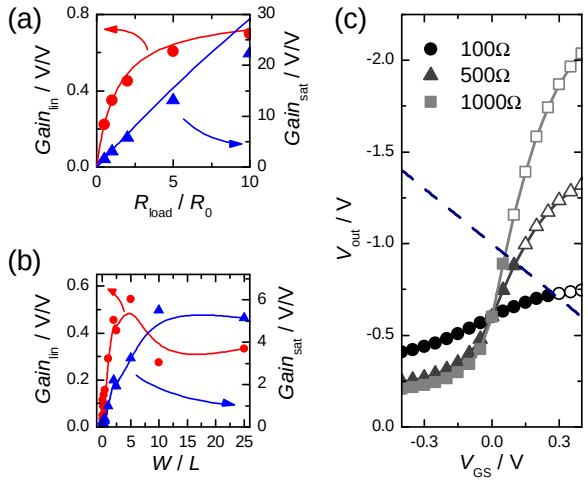

Figure 3.2: *(a) Voltage gain* $^{\Delta V_{out}}/_{\Delta V_{GS}}$ *for different drain load resistors for an input signal of* $\Delta V_{GS} = 1\,\mathrm{mV}$ *in both the linear regime (red,* $OP_{lin} = -0.2\,\mathrm{V}$*) and the saturation regime (blue,* $OP_{sat} = -0.8\,\mathrm{V}$*). The channel resistance is* $R_0 = 213\,\Omega$ *and* $R_0 = 513\,\Omega$ *for the linear regime and saturation regime respectively. The solid line shows an analytical model according to Equation (3.4). The same device is used as in Figure 3.1. (b) Voltage gain* $^{\Delta V_{out}}/_{\Delta V_{GS}}$ *for different aspect ratios for a drain load resistor of* $R_{load} = 500\,\Omega$ *in the linear regime (red) and the saturation regime (blue). The points are calculated according to Equation (3.4) using experimentally derived IV curves for each geometry. The thickness of the devices is* $d = 70\,\mathrm{nm}$*. The solid lines are a guide to the eye. (c) Output voltage versus gate voltage for different drain load resistors for the same device as in Figure 3.1. The operation point at* $V_{GS} = 0\,\mathrm{V}$ *is set to* $-0.6\,\mathrm{V}$*. The values are extracted graphically via the intersection of the load line with the output curve at each value of* V_{GS}*. Open symbols denote data outside the experimental limitation of* $|V_{GS} \breve{} V_{out}| < 1\,\mathrm{V}$ *, indicated by the dashed blue line, that allows for stable operation of the device.*

ential form of the drain current

$$\mathrm{d}I_\mathrm{D} = \left.\frac{\partial I_\mathrm{D}}{\partial V_\mathrm{GS}}\right|_{V_\mathrm{out}} \mathrm{d}V_\mathrm{GS} + \left.\frac{\partial I_\mathrm{D}}{\partial V_\mathrm{out}}\right|_{V_\mathrm{GS}} \mathrm{d}V_\mathrm{out} = g_\mathrm{m}^\mathrm{i} \cdot \mathrm{d}V_\mathrm{GS} + g_\mathrm{d}^\mathrm{i} \cdot \mathrm{d}V_\mathrm{out} \quad , \tag{3.2}$$

where g_m^i and g_d^i are the intrinsic transconduction and drain conductance respectively (i.e. with no drain load resistor). Using Equation (3.1) it follows that

$$\mathrm{d}I_\mathrm{D} = -\frac{1}{R_\mathrm{load}} \cdot \mathrm{d}V_\mathrm{out} \quad , \tag{3.3}$$

and Equation (3.2) can be solved for $^{\mathrm{d}V_\mathrm{out}}/_{\mathrm{d}V_\mathrm{GS}}$, i.e. the voltage gain *Gain* of the system

$$Gain_\mathrm{sat} = \left|\frac{\mathrm{d}V_\mathrm{out}}{\mathrm{d}V_\mathrm{GS}}\right| = \left|\frac{g_\mathrm{m}^\mathrm{i}}{1/R_\mathrm{load} + g_\mathrm{d}^\mathrm{i}}\right| \quad . \tag{3.4}$$

From this relation, it becomes clear that in the saturation regime, where the drain current is independent of the source drain bias (i.e. $g_{\mathrm{d}}^{\mathrm{i}} = 0$), the voltage gain is directly proportional to the transconductance times the drain load resistor, whereas in the linear regime the voltage gain saturates for higher drain load as $1/R_{\mathrm{load}}$ goes to zero (see Figure 3.2a). We compare this model to experimental data that have been retrieved by generating a sinusoidal signal with an amplitude $\Delta V_{\mathrm{GS}} = 1\,\mathrm{mV}$ and a frequency $f = 2\,\mathrm{Hz}$ at the gate and recording the output voltage over a few cycles. We again distinguish between the linear and the saturation regime, meaning that we adjust V_{out} to obtain the given operation points ($-0.2\,\mathrm{V}$ and $-0.8\,\mathrm{V}$) at $V_{\mathrm{GS}} = 0\,\mathrm{V}$ for each value of the drain load resistor. The model shows remarkable agreement with the experimental data. Only at high drain load the voltage gain is overestimated in the saturation regime. This can be explained with the fact that at such a high voltage gain ($> 20\,\mathrm{V/V}$), a small inevitable drift in the drain current that derives for example from evaporation of the electrolyte also gets amplified by the same amount and consequently the operation point at zero gate bias is shifted towards higher source drain bias.

Using Equation (3.4), we can also check the effect of device geometry for a given operation point and drain load resistor by using the intrinsic transconductance and drain conductance extracted from an IV curve of the plain OECT (see Figure 3.2b). It can be seen that again an overall higher gain can be achieved in the saturation regime. In the linear regime, the maximum gain can be obtained for aspect ratios of about $W/L = 5$ and in the saturation regime it seems to be at around $W/L = 15$. Rivnay et al. showed that the transconductance at $V_{\mathrm{GS}} = 0\,\mathrm{V}$ increases for increasing aspect ratio until a certain point (for a channel thickness of $d = 140\,\mathrm{nm}$ this is up to $W/L \approx 10$, for $d = 25\,\mathrm{nm}$ it is $W/L > 10$) [Rivnay, 2013]. This explains the findings in Figure 3.2b for the saturation regime as in this case the gain is directly proportional to the transconductance and the drain conductance can be neglected. In the linear regime, where the drain conductance is linear in W/L, the peak gain is shifted to lower aspect ratios as the drain conductance dominates in the denominator.

We emphasize the fact that this analytical derivation does not rely on any model for the OECT as it needs only the electrical characteristics (i.e. transconductance and drain conductance) of the plain transistor without any drain load. It is possible to arrive at an analytical expression and obtain similar findings using the Bernards model of the OECT [Bernards, 2007]. However, the agreement with the experimental data is not as good (see Section 3.5) which can be mainly attributed to the fact that the Bernards model considers a constant mobility not describing the real physics of the device. For more complex models, such as the one recently published by Friedlein et al., this system becomes impossible to solve analytically due to the power dependence of the source drain bias in the model [Friedlein, 2015].

One aspect that we neglected so far is the requirement of a high supply voltage at higher drain load to keep the same operation point at zero gate bias (see Equation (3.1)). As

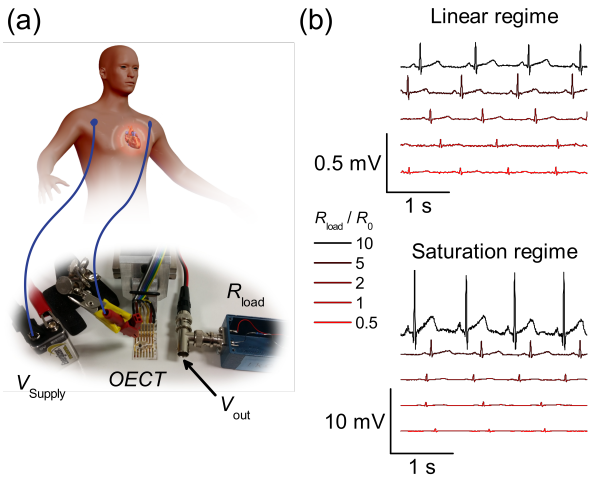

Figure 3.3: *(a) Schematic of the experimental setup for ECG recordings. The output voltage V_{out} can be directly picked up by a regular voltage recording system. The medical electrodes (blue) are placed below the clavicle to the left and to the right of the heart. The system is driven by a battery. (b) ECG recordings for different drain load in both linear and saturation regime. Each curve has been recorded consecutively with the same device. The channel dimensions of the OECT are $W/L = 2$ and $d = 70\,\mathrm{nm}$. The amplitude of the input signal recorded from the same electrodes was of the order of $\Delta V_{ECG} \approx 300\,\mu\mathrm{V}$. The recordings have been taken in a low noise environment.*

the PEDOT:PSS-based OECT is a normally-ON device and is shut down upon applying a positive gate voltage, the drain current is modulated from $I_{\max}$ to zero. In the same manner, the effective source drain bias on the OECT, i.e. V_{out}, will vary from the set operation point up to V_{supply}. This may lead to the unfortunate situation where the applied bias gets bigger than the electrochemical potential for water hydrolysis, inevitably destroying the device [Ferree, 2001; Zoulias, 2004]. In Figure 3.2c, the source drain bias is plotted against the gate voltage for different drain load resistors. The steeper this curve is, the better the amplification. But the device gets out of the stable operation window $|V_{\mathrm{out}} - V_{\mathrm{GS}}| < 1\,\mathrm{V}$ at far lower gate voltage. In order to avoid any instability issues it is best to limit the input signal to low amplitudes or use a negative polarity for the gate signal, bearing in mind that this way the OECT is pushed back into the linear regime upon gating.

However, as we are interested in recording biological signals such as electrocardiograms (ECG) or electroencephalograms (EEG), and the amplitude of those signals is generally in the order of a few hundreds of microvolt, we can safely assume that at $V_{\mathrm{GS}} = 0\,\mathrm{V}$ we stay within the stable operation window of the OECT [Zywietz, 1990]. As a proof of concept, we use the OECT based voltage amplifier system for measuring heart activity. For this, we place two medical electrodes below the clavicle on the left and the right side of the chest and connect them to the source and the gate of the OECT (see Figure 3.3a)

[Mason, 1966]. This way, the OECT is operated at $V_{GS} = (0\,V + ECG)$ and the heart activity is doping or dedoping the channel [Leleux, 2015]. The medical electrodes provide a good contact with the skin and allow for an effective gating. We note that in this configuration, the OECT is not in contact with the skin, thus acting solely as an external preamplifier. Using this kind of configuration, we are able to control the value of the drain load resistor, which would not be possible in an all integrated solution. Due to the inherent voltage conversion at the drain load resistor, we can directly connect the output signal to a regular acquisition system for electrophysiology. For comparison, we record the heart activity with the OECT operated in linear and saturation regime. Upon varying the drain load resistor, we can modify the amplification of the signal (see Figure 3.3b). It can be seen that operating the OECT in the linear regime does not give any substantial amplification of the input signal. At best there is a one to one transduction for high drain load. As already stated in Figure 3.2a, the amplification saturates for values of $R_{load} > 5 \cdot R_{chan}$. Nonetheless, a clear ECG signal can be seen with all relevant features of the PQRST complex (characteristic waves of the signal linked with propagation of muscle activity in the heart) for practically every value of the drain load resistor [Clifford, 2006]. The same holds when operating the device in the saturation regime with the difference being a much higher amplitude of the output signal and an amplification of as much as $Gain_{sat} = 30\,V/V$ for the highest recorded drain load resistor $R_{load} = 10 \cdot R_{chan}$. We note that the signal-to-noise ratio does not seem to change for the different recordings (see Section 3.5) which can be mainly attributed to the fact that the experiment has been conducted in a low-noise environment, inside a Faraday cage room.

3.3 Conclusion

We have successfully demonstrated the working principle of a voltage amplifier circuit based on a microfabricated organic electrochemical transistor with high transconductance using a simple resistor in series. This creates a floating voltage point that linearly depends on the drain current and can be used to transduce signals picked up by the OECT. As a proof of concept, we use the OECT-based voltage amplifier externally in combination with medical electrodes. Characterization measurements show that a much better performance can be achieved upon driving the transistor in the saturation regime. In this case, the drain current is independent of the source-drain bias of the OECT and thus the output voltage depends directly on the input voltage at the gate of the OECT. We were able to record electrocardiographic signals by using a voltage recording system utilized for standard tests in a hospital. To our knowledge, this is the first time voltage-to-voltage amplifying transduction of electrophysiological activity has been demonstrated with an OECT, rendering this device directly useful in a clinical setup. Future work is ongoing to implement a gel electrolyte allowing for long-term

measurements directly on the skin to provide an active organic electrode that can be compared to regular electrodes.

3.4 Experimental Section

Device Fabrication The devices were fabricated according to the parylene lift-off method reported previously [Sessolo, 2013]. Standard microscope glass slides were cleaned via sonication in an aceton & isopropyl alcohol solution and dried with nitrogen. Connection pads and interconnects were deposited through a lift-off process using photolithographic patterning of positive photoresist (S1813) with a SUSS MJB4 broad band UV light mask aligner and MF-26A developer. A subsequent metal deposition via evaporation of chromium (10 nm) and of gold (120 nm) and metal lift-off using acetone defines the gold lines. A first layer of parylene C (2 µm), deposited via a SCS Labcoater 2 together with a small amount of 3-(trimethoxysilyl)propyl-methacrylate (A-174 Silane) to enhance adhesion, acts as an insulator to prevent disturbing capacitive effects at the metal liquid interface. Subsequently, an anti-adhesive layer was spin coated using a dilution of industrial cleaner (2 %, Micro-90) and a second parylene C sacrificial layer (2 µm) is deposited. To define the contact pads and the channel of the OECT, a second photolithographic patterning step using a thick positive photoresist (5 µm, AZ9260) and AZ developer is used to protect the parylene C layers from a subsequent plasma reactive ion etching step via an Oxford 80 Plasmalab plus (400 W, $O_2 = 50$ sccm, $CHF_3 = 5$ sccm, 8 min), at the point where no PEDOT:PSS is supposed to stay. The PEDOT:PSS solution was prepared mixing an aqueous dispersion (19 mL, Clevios PH-1000 from Heraeus Holding GmbH) with ethylene glycol (1 mL) and dodecyl benzene sulfonic acid (50 µL), to improve conductivity and enhance film formation and sonicating for 40 min, then adding (3-glycidyloxypropyl) trimethoxysilane (1 wt%), to prevent delamination of the film and sonicating for another 5 min. This dispersion was spincoated for a target thickness of about 90 nm (3000 rpm, 90 s) and baked (90 °C, 90 s). The PEDOT:PSS thus covers the whole glass slide and fills the "wells" defined in the second photolithographic patterning step. Peeling of the sacrificial layer and hard-baking the device (125 °C, 1 h) thus defines the channel width, the distance between source and drain contact defines the channel length. Immersing the devices in deionized water over night removes excess low molecular weight compounds.

Device Characterization All experiments were done using a NaCl solution (100 mM) as electrolyte and a Ag/AgCl pellet (Warner Instruments) as gate electrode. The IV curves were recorded using a Keithley 2612A dual SourceMeter with customized LabVIEW software. For the pre-characterization experiments with the drain load a Voltcraft R-BOX 01 decade resistor box was connected to the OECT and a Keith-

ley 2612A dual SourceMeter was used for the supply voltage, the output voltage was recorded using a National Instruments USB-6251 BNC data acquisition system and customized LabVIEW software. The ECG recordings were done in a low noise room at the hospital La Timone in Marseille, France. Ambu sensor N medical Ag/AgCl electrodes with 0.95 cm diameter gel-assisted contact area were used as standard ECG electrodes to make contact with the skin. A battery was used for the supply voltage to reduce the noise coming from building ground and the output voltage was recorded using a Braintronics voltage recording system with Brainbox EEG-1166 amplifiers. The data were treated subsequently using a 49 Hz – 51 Hz band block fast Fourier transform (FFT) filter, a 100 Hz low pass FFT filter and a 0.05 Hz high pass FFT filter.

3.5 Supporting Information

Bernards model [Bernards, 2007]

Here we present a derivation of an analytical expression for the gain of the OECT based voltage amplifier.

Linear regime
In the linear regime ($V_{\mathrm{out}} > V_{\mathrm{GS}} - V_{\mathrm{P}}$), the drain current is given by

$$I_{\mathrm{D}} = G\left(1 - \frac{V_{\mathrm{GS}} - 0.5 \cdot V_{\mathrm{out}}}{V_{\mathrm{P}}}\right) \cdot V_{\mathrm{out}} \quad , \tag{3.5}$$

where $G = q\mu p_0 WT/L$ and $V_{\mathrm{P}} = qp_0 T/c_{\mathrm{d}}$. Using the load line equation

$$I_{\mathrm{D}} = \frac{V_{\mathrm{supply}}}{R_{\mathrm{load}}} - \frac{V_{\mathrm{out}}}{R_{\mathrm{load}}} \quad , \tag{3.6}$$

the drain current can be eliminated and a quadratic equation in V_{out} can be obtained (for ease of reading we denote the drain load resistor R_{load} simply with R from now on)

$$[0.5 \cdot GR] \cdot V_{\mathrm{out}}^2 + [GRV_{\mathrm{P}} - GRV_{\mathrm{GS}} + V_{\mathrm{P}}] \cdot V_{\mathrm{out}} + [-V_{\mathrm{P}}V_{\mathrm{GS}}] = 0 \quad . \tag{3.7}$$

This can be solved for V_{out}:

$$V_{\mathrm{out}} = \frac{-\left(GRV_{\mathrm{P}} - GRV_{\mathrm{GS}} + V_{\mathrm{P}}\right) \pm \sqrt{\left(GRV_{\mathrm{P}} - GRV_{\mathrm{GS}} + V_{\mathrm{P}}\right)^2 + 2GRV_{\mathrm{P}}V_{\mathrm{supply}}}}{GR} \quad . \tag{3.8}$$

Note that the negative square root in Equation (3.8) can be neglected as $|V_{\mathrm{out}}| \leq |V_{\mathrm{supply}}|$ which holds only for the positive square root. The gain is thus given by the derivative

$$Gain_{\mathrm{lin}} = \left|\frac{\partial V_{\mathrm{out}}}{\partial V_{\mathrm{GS}}}\right| = \left|1 - \frac{V_{\mathrm{P}} + GR\left(V_{\mathrm{P}} - V_{\mathrm{GS}}\right)}{\sqrt{\left(V_{\mathrm{P}} + GR\left(V_{\mathrm{P}} - V_{\mathrm{GS}}\right)\right)^2 + 2GRV_{\mathrm{P}}V_{\mathrm{supply}}}}\right| \quad . \tag{3.9}$$

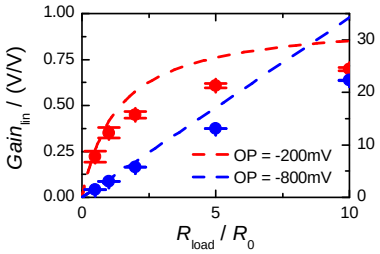

Figure 3.4: *Voltage gain* $^{\Delta V_{out}}/_{\Delta V_{GS}}$ *for different drain load resistors for an input signal of* $\Delta V_{GS} = 1\,\mathrm{mV}$ *in both the linear regime (red,* $OP_{lin} = -0.2\,\mathrm{V}$*) and the saturation regime (blue,* $OP_{sat} = -0.8\,\mathrm{V}$*). The channel resistance is* $R_0 = 213\,\Omega$ *and* $R_0 = 513\,\Omega$ *for the linear regime and saturation regime respectively. The dashed curve shows a fit using the Bernards model (see Equation* (3.10) *and Equation* (3.14)*). The fit parameters are* $G = 5.8\,\mathrm{mS}$ *and* $V_P = 0.53\,\mathrm{V}$*.*

Note that the gain is smaller than one, meaning that no amplification of the signal is possible in the linear regime. At $V_{\mathrm{GS}} = 0$ this simplifies to

$$Gain_{\mathrm{lin}} = \left| 1 - \frac{V_{\mathrm{P}} \cdot (GR+1)}{\sqrt{V_{\mathrm{P}}^2 \cdot (GR+1)^2 + 2GRV_{\mathrm{P}}V_{\mathrm{supply}}}} \right| \quad . \tag{3.10}$$

Saturation regime

In the saturation regime ($V_{\mathrm{out}} \leq V_{\mathrm{GS}} - V_{\mathrm{P}}$), the drain current is given by

$$I_{\mathrm{D}} = -\frac{G \cdot (V_{\mathrm{GS}} - V_{\mathrm{P}})^2}{2V_{\mathrm{p}}} \quad , \tag{3.11}$$

and the output voltage can be derived to

$$V_{\mathrm{out}} = \frac{GR}{2V_{\mathrm{P}}} \cdot V_{\mathrm{GS}}^2 - GR \cdot V_{\mathrm{GS}} + \frac{1}{2}GRV_{\mathrm{P}} + V_{\mathrm{supply}} \quad . \tag{3.12}$$

This leads to a gain of

$$Gain_{\mathrm{sat}} = \left| \frac{\partial V_{\mathrm{out}}}{\partial V_{\mathrm{GS}}} \right| = \left| GR \cdot \left(\frac{V_{\mathrm{GS}}}{V_{\mathrm{P}}} - 1 \right) \right| \quad , \tag{3.13}$$

which scales linearly with the drain load. At $V_{\mathrm{GS}} = 0$ the gain is directly proportional to the product of the conductance and the drain load

$$Gain_{\mathrm{sat}} = |-GR| \quad . \tag{3.14}$$

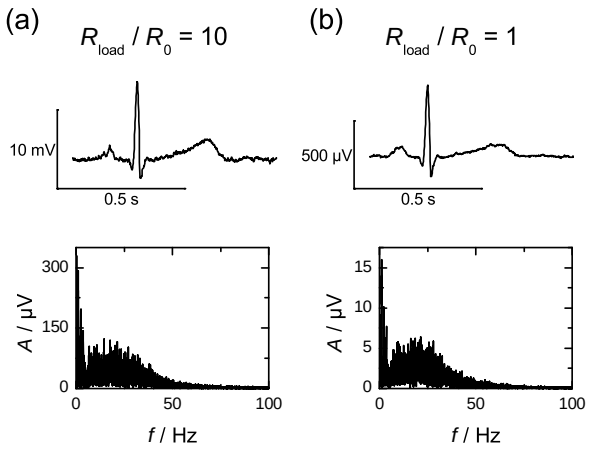

Figure 3.5: *Comparison of ECG signal recorded for two different values of the drain load resistor, (a) $R_{load} = 5.13\,\mathrm{k\Omega}$ and (b) $R_{load} = 513\,\Omega$. The OECT is operated in the saturation regime ($-0.8\,\mathrm{V}$). The Fourier transform shows the same frequency content and the signal-to-noise ratio does not differ between the two measurements. The presented data is unfiltered.*

Signal-to-noise analysis

As can be seen in Figure 3.5, the signal-to-noise ratio does not show any substantial dependency on the drain load resistor. The Fourier transform shows the same frequency content for a small drain load ($R_{\mathrm{load}}/R_0 = 1$) and a big drain load ($R_{\mathrm{load}}/R_0 = 10$). Apart from the overall increased amplitude of the signal at higher drain load due to the larger amplification, we can assume that changing the drain load does not increase the sensitivity of the device. This might be attributed to the fact that the drain load resistor is an external resistor box with long lead lines that might pick up all relevant noise content before entering the differential amplifier. A more sophisticated solution with an all integrated device layout, where the drain load resistor is in close proximity to the transistor, would be beneficial in that case. With such an all integrated "active organic electrode", one would not be able to modify the value of the drain load resistor on-the-fly and therefore could not study the different operation regimes, as is the purpose of this study.

References

[Andersson, 2002] P. Andersson, D. Nilsson, P.-O. Svensson, M. Chen, A. Malmström, T. Remonen, T. Kugler, and M. Berggren: "*Active Matrix Displays Based on All-Organic Electrochemical Smart Pixels Printed on Paper*", Advanced Materials **14** (2002), p. 1460.

[Basiricò, 2012] L. Basiricò, P. Cosseddu, A. Scidà, B. Fraboni, G. Malliaras, and A. Bonfiglio: "*Electrical characteristics of ink-jet printed, all-polymer electrochemical transistors*", Organic Electronics **13** (2012), pp. 244–248.

[Bernards, 2007] D. A. Bernards and G. G. Malliaras: "*Steady-State and Transient Behavior of Organic Electrochemical Transistors*", Advanced Functional Materials **17** (23, 2007), pp. 3538–3544.

[Buzsáki, 2012] G. Buzsáki, C. A. Anastassiou, and C. Koch: "*The origin of extracellular fields and currents — EEG, ECoG, LFP and spikes*", Nature Reviews Neuroscience **13** (18, 2012), pp. 407–420.

[Campana, 2014] A. Campana, T. Cramer, D. T. Simon, M. Berggren, and F. Biscarini: "*Electrocardiographic Recording with Conformable Organic Electrochemical Transistor Fabricated on Resorbable Bioscaffold*", Advanced Materials **26** (2014), pp. 3874–3878.

[Chou, 1987] S. Y. Chou and D. Antoniadis: "*Relationship between measured and intrinsic transconductances of FET's*", IEEE Transactions on Electron Devices **34** (1987), pp. 448–450.

[Clifford, 2006] G. D. Clifford, ed.: "*Advanced methods and tools for ECG data analysis*", Engineering in medicine & biology, Boston, Mass. 2006, 384 pp., ISBN: 9781580539661.

[Coyle, 2010] S. Coyle, King-Tong Lau, N. Moyna, D. O'Gorman, D. Diamond, F. Di Francesco, D. Costanzo, P. Salvo, M. Trivella, D. De Rossi, N. Taccini, R. Paradiso, J.-A. Porchet, A. Ridolfi, J. Luprano, C. Chuzel, T. Lanier, F. Revol-Cavalier, S. Schoumacker, V. Mourier, I. Chartier, R. Convert, H. De-Moncuit, and C. Bini: "*BIOTEX - Biosensing Textiles for Personalised Healthcare Management*", IEEE Transactions on Information Technology in Biomedicine **14** (2010), pp. 364–370.

[Fensli, 2005] R. Fensli, E. Gunnarson, and T. Gundersen: "*A wearable ECG-recording system for continuous arrhythmia monitor-*

ing in a wireless tele-home-care situation", Conference: 18th IEEE Symposium on Computer-Based Medical Systems (CBMS'05), (2005), pp. 407–412.

[Ferree, 2001] T. C. Ferree, P. Luu, G. S. Russell, and D. M. Tucker: "*Scalp electrode impedance, infection risk, and EEG data quality*", Clinical Neurophysiology **112** (2001), pp. 536–544.

[Friedlein, 2015] J. T. Friedlein, S. E. Shaheen, G. G. Malliaras, and R. R. McLeod: "*Optical Measurements Revealing Nonuniform Hole Mobility in Organic Electrochemical Transistors*", Advanced Electronic Materials **1** (2015), p. 1500189.

[Isaksson, 2007] J. Isaksson, P. Kjäll, D. Nilsson, N. Robinson, M. Berggren, and A. Richter-Dahlfors: "*Electronic control of Ca2+ signalling in neuronal cells using an organic electronic ion pump*", Nature Materials **6** (2007), pp. 673–679.

[Khodagholy, 2013a] D. Khodagholy, T. Doublet, P. Quilichini, M. Gurfinkel, P. Leleux, A. Ghestem, E. Ismailova, T. Hervé, S. Sanaur, C. Bernard, and G. G. Malliaras: "*In vivo recordings of brain activity using organic transistors*", Nature Communications **4** (2013), p. 1575.

[Khodagholy, 2013b] D. Khodagholy, J. Rivnay, M. Sessolo, M. Gurfinkel, P. Leleux, L. H. Jimison, E. Stavrinidou, T. Herve, S. Sanaur, R. M. Owens, and G. G. Malliaras: "*High transconductance organic electrochemical transistors*", Nature Communications **4** (12, 2013), p. 2133.

[Kittlesen, 1984] G. P. Kittlesen, H. S. White, and M. S. Wrighton: "*Chemical derivatization of microelectrode arrays by oxidation of pyrrole and N-methylpyrrole: fabrication of molecule-based electronic devices*", Journal of the American Chemical Society **106** (1984), pp. 7389–7396.

[Leleux, 2015] P. Leleux, J. Rivnay, T. Lonjaret, J.-M. Badier, C. Bénar, T. Hervé, P. Chauvel, and G. G. Malliaras: "*Organic Electrochemical Transistors for Clinical Applications*", Advanced Healthcare Materials **4** (2015), pp. 142–147.

[Lin, 2011] P. Lin, X. Luo, I.-M. Hsing, and F. Yan: "*Organic Electrochemical Transistors Integrated in Flexible Microfluidic Systems and Used for Label-Free DNA Sensing*", Advanced Materials **23** (15, 2011), pp. 4035–4040.

[Mason, 1966] R. E. Mason and I. Likar: "*A new system of multiple-lead exercise electrocardiography*", American Heart Journal **71** (1966), pp. 196–205.

[Nilsson, 2002a] D. Nilsson, M. Chen, T. Kugler, T. Remonen, M. Armgarth, and M. Berggren: "*Bi-stable and Dynamic Current Modu-*

lation in Electrochemical Organic Transistors", Advanced Materials **14** (2002), p. 51.

[Nilsson, 2002b] D. Nilsson, T. Kugler, P.-O. Svensson, and M. Berggren: "*An all-organic sensor–transistor based on a novel electrochemical transducer concept printed electrochemical sensors on paper*", Sensors and Actuators B: Chemical **86** (2002), pp. 193–197.

[Pantelopoulos, 2010] A. Pantelopoulos and N. Bourbakis: "*A Survey on Wearable Sensor-Based Systems for Health Monitoring and Prognosis*", IEEE Transactions on Systems, Man, and Cybernetics, Part C (Applications and Reviews) **40** (2010), pp. 1–12.

[Ramuz, 2014] M. Ramuz, A. Hama, M. Huerta, J. Rivnay, P. Leleux, and R. M. Owens: "*Combined Optical and Electronic Sensing of Epithelial Cells Using Planar Organic Transistors*", Advanced Materials **26** (2014), pp. 7083–7090.

[RiveraRuiz, 2008] M. Rivera-Ruiz, C. Cajavilca, and J. Varon: "*Einthoven's string galvanometer: the first electrocardiograph*", Texas Heart Institute Journal **35** (2008), p. 174.

[Rivnay, 2013] J. Rivnay, P. Leleux, M. Sessolo, D. Khodagholy, T. Hervé, M. Fiocchi, and G. G. Malliaras: "*Organic Electrochemical Transistors with Maximum Transconductance at Zero Gate Bias*", Advanced Materials **25** (2013), pp. 7010–7014.

[Rivnay, 2014] J. Rivnay, R. M. Owens, and G. G. Malliaras: "*The Rise of Organic Bioelectronics*", Chemistry of Materials **26** (14, 2014), pp. 679–685.

[Rivnay, 2015] J. Rivnay, P. Leleux, M. Ferro, M. Sessolo, A. Williamson, D. A. Koutsouras, D. Khodagholy, M. Ramuz, X. Strakosas, R. M. Owens, C. Benar, J.-M. Badier, C. Bernard, and G. G. Malliaras: "*High-performance transistors for bioelectronics through tuning of channel thickness*", Science Advances **1** (22, 2015), e1400251–e1400251.

[Sessolo, 2013] M. Sessolo, D. Khodagholy, J. Rivnay, F. Maddalena, M. Gleyzes, E. Steidl, B. Buisson, and G. G. Malliaras: "*Easy-to-Fabricate Conducting Polymer Microelectrode Arrays*", Advanced Materials **25** (18, 2013), pp. 2135–2139.

[Sessolo, 2014] M. Sessolo, J. Rivnay, E. Bandiello, G. G. Malliaras, and H. J. Bolink: "*Ion-Selective Organic Electrochemical Transistors*", Advanced Materials **26** (2014), pp. 4803–4807.

[Stavrinidou, 2013] E. Stavrinidou, P. Leleux, H. Rajaona, D. Khodagholy, J. Rivnay, M. Lindau, S. Sanaur, and G. G. Malliaras: "*Direct Measurement of Ion Mobility in a Conducting Polymer*", Advanced Materials **25** (27, 2013), pp. 4488–4493.

[Stavrinidou, 2015] E. Stavrinidou, R. Gabrielsson, E. Gomez, X. Crispin, O. Nilsson, D. T. Simon, and M. Berggren: "*Electronic plants*", Science Advances **1** (20, 2015), e1501136–e1501136.

[Takamatsu, 2015] S. Takamatsu, T. Lonjaret, D. Crisp, J.-M. Badier, G. G. Malliaras, and E. Ismailova: "*Direct patterning of organic conductors on knitted textiles for long-term electrocardiography*", Scientific Reports **5** (8, 2015), p. 15003.

[Tang, 2011] H. Tang, F. Yan, P. Lin, J. Xu, and H. L. W. Chan: "*Highly Sensitive Glucose Biosensors Based on Organic Electrochemical Transistors Using Platinum Gate Electrodes Modified with Enzyme and Nanomaterials*", Advanced Functional Materials **21** (21, 2011), pp. 2264–2272.

[Webster, 1984] J. G. Webster: "*Reducing Motion Artifacts and Interference in Biopotential Recording*", IEEE transactions on biomedical engineering **BME-31** (1984), pp. 823–826.

[Yi, 2015] Z. Yi, G. Natale, P. Kumar, E. D. Mauro, M.-C. Heuzey, F. Soavi, I. I. Perepichka, S. K. Varshney, C. Santato, and F. Cicoira: "*Ionic liquid–water mixtures and ion gels as electrolytes for organic electrochemical transistors*", J. Mater. Chem. C **3** (2015), pp. 6549–6553.

[Yuen, 2007] J. D. Yuen, A. S. Dhoot, E. B. Namdas, N. E. Coates, M. Heeney, I. McCulloch, D. Moses, and A. J. Heeger: "*Electrochemical Doping in Electrolyte-Gated Polymer Transistors*", Journal of the American Chemical Society **129** (2007), pp. 14367–14371.

[Zoulias, 2004] E. Zoulias, E. Varkaraki, N. Lymberopoulos, C. N. Christodoulou, and G. N. Karagiorgis: "*A review on water electrolysis*", TCJST **4** (2004), pp. 41–71.

[Zywietz, 1990] C. Zywietz, J. L. Willems, P. Arnaud, J. H. van Bemmel, R. Degani, and P. W. Macfarlane: "*Stability of Computer ECG Amplitude Measurements in the Presence of Noise*", Computers and Biomedical Research **23** (1990), pp. 10–31.

Chapter 4

Lactate Detection in Tumor Cell Cultures Using Organic Transistor Circuits

This chapter is based on the publication:

> **"Lactate Detection in Tumor Cell Cultures Using Organic Transistor Circuits"**
>
> *M. Braendlein, A-M. Pappa, M. Ferro, A. Lopresti, C. Acquaviva, E. Mamessier, G. G. Malliaras, R. M. Owens*
>
> Advanced Materials online, DOI:10.1002/adma.201605744 (2017).

Lactate has drawn increasing attention over the last years as a biomarker for cancer staging, due to enhanced metabolic activity associated with highly proliferative aggressive cell growth (Warburg effect). However, there are many issues related to sensing metabolites such as lactate under "real" conditions due to background signals arising from temperature drift, evaporation of the electrolyte and oxidizable compounds present in complex electrolytes such as blood. In the present work, we implement two organic electrochemical transistors into a Wheatstone bridge configuration, one acting as a reference sensor and the other functionalized to be specific to lactate. With this reference based sensor we show the ability to detect from as few as several 10s of cells, extremely important for cancer diagnostics where obtaining large numbers of cells can be problematic and invasive. This enabled us to sensitively detect lactate concentrations from patient derived samples. By comparing samples derived from cancer patients with healthy controls, we indeed find an elevated lactate concentration as predicted by the Warburg effect. This non-invasive highly specific and sensitive diagnostic has enormous potential for prediction of metastatic potential.

4.1 Introduction

Rapid and early diagnosis of disease is known to be a significant factor in treatment and improved prognosis, notably in cancer. From the first commercialized device based on the "enzyme electrode", introduced by Clark and Lyons, able to measure accurately glucose concentrations in whole blood samples [Clark, 1962; Updike, 1967], to research prototypes of miniaturized epidermal sensor chips able to measure real-time multiple analytes [Gao, 2016], biosensors have evolved significantly and become invaluable tools for diagnosis of many pathologies from infections to heart disease. Remarkably, little of the progress in the field of biosensing has translated to improved diagnosis of cancer [Liu, 2012].

Use of biosensors in diagnostic applications requires identification of a biomarker (to confer specificity) while the sensitivity is mostly related to the intimate coupling of a reaction involving the biomarker, with a transducer. In cancer diagnostics, clinicians are highly dependent on the identification of biomarkers that will reliably predict occurrence and recurrence of cancerous cell populations, however such reliable biomarkers are few and far between, perhaps explaining the dearth of cancer biosensing devices [Henry, 2012; Kalia, 2015]. One marked feature of cancer however, is the increased glycolytic activity associated with highly proliferative aggressive cell growth [Walenta, 2000]. In recent years, increased metabolic activity has been suggested as a biomarker for cancer. This idea is not new, having been introduced over 60 years ago by Warburg, who predicted enhanced uptake and usage of glucose and thus production of lactate [Warburg, 1956]. Lactate has proven to be a prognostic indicator of the degree of malignancy in primary tumors as well as of the probability of metastasis [Walenta, 2002].

Electrical, label-free biosensing of metabolites such as glucose and lactate is known to be advantageous with regards to speed and sensitivity, and indeed the integration of biosensors with microelectronic devices has brought about multiplexed capabilities as well as enabling miniaturization and automation [Pappa, 2016; Lafleur, 2016; Luka, 2015]. However, some key issues still impede their practical implementation in a clinical setting. These issues include signal drift due to environmental changes (e.g. electrolyte evaporation, temperature changes, instability of transducer), as well as signal misinterpretation due to interference (e.g. charged species or oxidizable compounds in complex media) [Deng, 2014]. Sensor circuits represent an elegant alternative solution, departing from a single sensor and focusing on a more complete system that can be readily intercepted with simple acquisition tools, as demonstrated by Svensson et al. [Svensson, 2008].

Recently, the organic electrochemical transistor (OECT) has drawn considerable attention as sensing element [Rivnay, 2014; Liao, 2015; Sessolo, 2014]. In a three terminal configuration, the active material, being comprised of an organic semiconductor, can

be electrochemically doped or dedoped through an ionic current from the electrolyte into the polymer, thereby changing its conductivity [Kittlesen, 1984]. The possibility for low voltage gating provides devices sensitive to biological signals that may consist of minute ionic currents [Kergoat, 2012]. OECTs have proven to outperform state-of-the-art devices such as electrodes [Khodagholy, 2013b], and have been used in a wide variety of biological applications, including metabolite sensing [Khodagholy, 2013a; Shim, 2009; Strakosas, 2014].

4.2 Results and Discussion

Bearing in mind the complex issues related to sensitive and specific detection of metabolites of interest in pathologies such as cancer, in this article, we present an *in vitro* electronic platform for sensitive and accurate metabolite sensing in highly interfering samples, such as cell culture media. In particular, we developed a reference-based sensor circuit, by integrating two differently functionalized OECTs, comprised of the well-known organic p-type semiconductor poly(3,4-ethylenedioxythiophene):poly(styrene sulfonate) (PEDOT:PSS) [Rivnay, 2015], into a Wheatstone bridge layout. The planar all-PEDOT:PSS configuration of the channel and the gate (Figure 4.1a) facilitates the device biofunctionalization [Strakosas, 2014] and also allows for future integration with microfluidics. For the device fabrication, a new lithographic approach based on a fluorinated photoresist, that allows for direct patterning of spun-cast PEDOT:PSS, was employed in this work. Starting from a homogeneously coated PEDOT:PSS film and ablatively patterning the active areas [Taylor, 2009; Zhang, 2016], a greater device homogeneity can be achieved (Figure 4.1b and Figure 4.2c) contrary to the conventional Parylene-C peel-off technique [Sessolo, 2013]. According to the output and transfer characteristics of the OECTs (Figure 4.2a-b), the maximum transconductance [Rivnay, 2013] $g_\mathrm{m} = {}^{\Delta I_\mathrm{D}}/_{\Delta V_\mathrm{GS}}$ of 6.4 mS is obtained at $V_\mathrm{GS} = 200\,\mathrm{mV}$, which coincides with the sensor's working potential, to ensure maximum sensitivity. By adding a drain load resistor in series with the OECT, a floating voltage point V_float is created which depends on the drain current I_D and is set by the supply voltage V_supply,

$$V_\mathrm{float} = V_\mathrm{supply} - R_\mathrm{load} \cdot I_\mathrm{D}\left(V_\mathrm{GS}, V_\mathrm{float}\right) \quad . \tag{4.1}$$

To a first order, V_float depends linearly on the applied gate bias and can thus be used as a reference to the signal of interest. By connecting two such branches in parallel, a full Wheatstone bridge is provided (Figure 4.1c), where one OECT is used as a reference and the other can be functionalized, to respond specifically to a given target analyte. The difference between the two floating voltage points, the output voltage V_out, gives an intrinsically background subtracted response to any change in the gating of the sensing OECT. In addition, the response starts at low amplitudes and increases with the gate

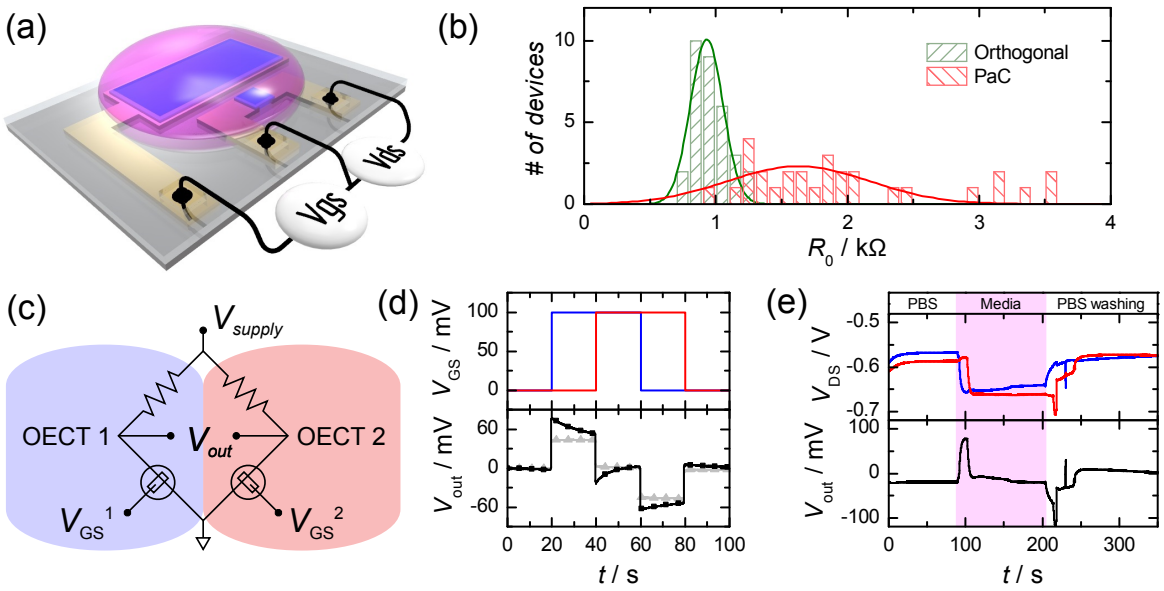

Figure 4.1: *(a) Depiction of a planar OECT (blue: PEDOT:PSS, pink: electrolyte). The voltage supplies for the gate (V_{GS}) and the source-drain bias (V_{DS}) are depicted as white spheroids connected to the gold leads. (b) Comparison of channel resistance at $V_{GS} = 0\,\mathrm{V}$ and $V_{DS} = -0.1\,\mathrm{V}$ of 32 devices fabricated with orthogonal resist (green) against 32 devices with Parylene-C peel-off method (red). The bin size is $0.1\,\mathrm{k\Omega}$. The bold lines show a Gaussian fit. The distribution is much narrower for the orthogonal method, indicating a much better device to device homogeneity. The device geometry is $W/L = 0.6$ and $d = 100\,\mathrm{nm}$. (c) Schematic circuit layout of the Wheatstone bridge sensor circuit. The load resistors are on the drain side of the OECT. The electrolyte of the two OECTs is physically separated, ensuring a disjoined gating. The two branches of the bridge are highlighted in blue and red. (d) Chronopotentiometric recording upon pulsing the gate of each OECT for different values of the drain load resistor (gray triangles: $R_{load} = 70\,\Omega$ and $V_{supply} = -1.5\,\mathrm{V}$; black squares: $R_{load} = 190\,\Omega$ and $V_{supply} = -2.7\,\mathrm{V}$). The pulse pattern is shown in the upper graph for the left (blue) and the right (red) branch of the Wheatstone bridge. The results have been offset corrected, $V_{out} - V_{out}\,(t = 0)$. (e) Chronopotentiometric recording upon changing the electrolyte. The upper graph shows the floating voltage point of each branch of the Wheatstone bridge circuit. The lower graph shows the output voltage, i.e. the voltage difference between the two floating points. The electrolyte is changed from 1X PBS (white) to DMEM cell culture media supplemented with FBS (pink) and then consecutively washed again with 1X PBS (three times). The spikes in the curves are due to pipetting effects. The supply voltage is $V_{supply} = -2.5\,\mathrm{V}$ for load resistors of $R_{load} = 190\,\Omega$. The gate voltage is kept constant at $V_{GS} = 200\,\mathrm{mV}$.*

voltage. This so called signal-ON response is generally easier to detect with simple data acquisition tools. The magnitude of the drain load resistor sets the inherent gain of the device $^{\Delta V_{\mathrm{out}}}/_{\Delta V_{\mathrm{GS}}}$ and shifts the transconductance depending on the operation regime

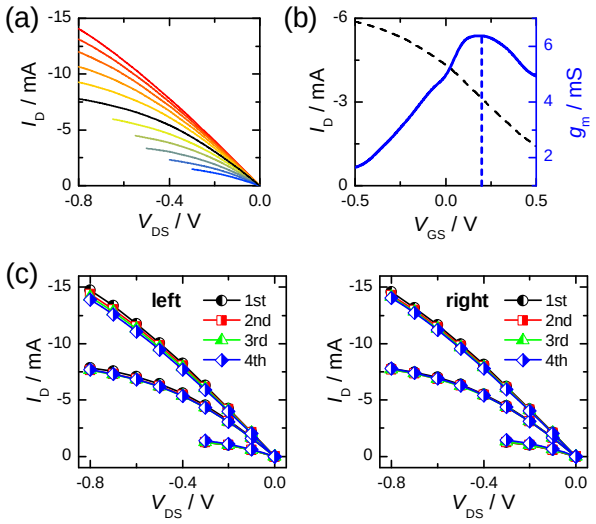

Figure 4.2: *(a) Output characteristics of the OECTs used in the Wheatstone bridge sensor. The aspect ratio of the channel is* $W/L = 10$ *and thickness is* $d = 100\,\mathrm{nm}$*. The gate voltage* V_{GS} *is varied from* $-0.5\,\mathrm{V}$ *(red curve) to* $0.5\,\mathrm{V}$ *(blue curve) in steps of* $100\,\mathrm{mV}$*. The drain voltage is ramped from* $0\,\mathrm{V}$ *to a maximum voltage difference between source to drain and gate to drain of no more than* $-0.8\,\mathrm{V}$ *to avoid water electrolysis. The output curve at* $V_{GS} = 0\,\mathrm{V}$ *is highlighted (black). (b) Transfer characteristics of the same OECT at* $V_{DS} = 0.3\,\mathrm{V}$*. The maximum transconductance is at* $V_{GS} = 0.2\,\mathrm{V}$ *(dashed blue line). (c) Consecutive IV curves for the OECTs of the left and the right branch in the Wheatstone bridge configuration for one selected device. The gate voltages from top to bottom are* $V_{GS} = [-0.5\,\mathrm{V}, 0\,\mathrm{V}, 0.5\,\mathrm{V}]$*. The OECTs have been measured as is after finishing the fabrication process. It can be seen that the output characteristics are fairly stable with consecutive cycling, indicating good device stability. Also, the drain current is almost identical for both OECTs over the whole voltage ramp, showing a good device homogeneity. (d) Comparison of channel resistance at* $V_{GS} = 0\,\mathrm{V}$ *and* $V_{DS} = -0.1\,\mathrm{V}$ *of 32 devices fabricated with orthogonal resist (green) against 32 devices with Parylene-C peel-off method (red). The bin size is* $0.1\,\mathrm{k\Omega}$*. The bold lines show a Gaussian fit. The distribution is much narrower for the orthogonal method, indicating a much better device to device homogeneity.*

[Braendlein, 2016]. Specifically, the gain scales linearly when operating the device in the saturation regime. We thus herein set the operation point of both OECTs to $OP = -0.6\,\mathrm{V}$. This voltage value is not sufficient to reach full saturation in our device, but gives a good compromise between linearity in the gain and a sufficient dynamic range for the sensing mechanism to avoid electrolysis in the water based electrolyte [Zoulias, 2004].

We demonstrate the working principle of our Wheatstone bridge platform upon the application of a voltage pulse at both gates (Figure 4.1d). The electrolyte of the reference OECT is physically separated from the sensing OECT. As expected, V_{out}

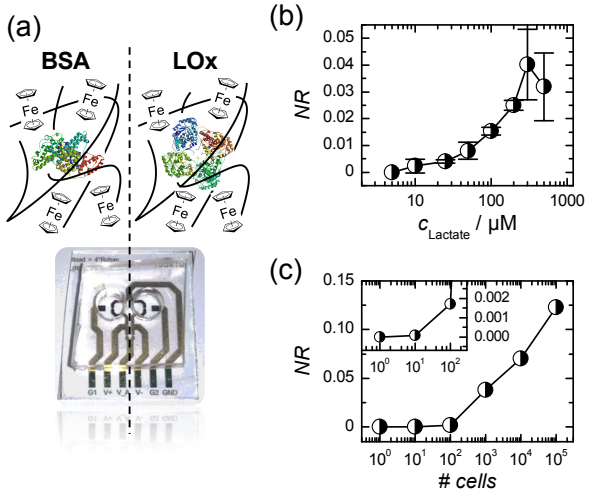

Figure 4.3: *(a) Schematic depiction of the biofunctionalization approach using lactate oxidase. Ferrocene is attached to a polymeric supporting matrix, chitosan. The chitosan-ferrocene/lactate oxidase complex is immobilized on the sensing OECT using epoxy terminated self-assembled monolayers. On the reference OECT the same complex is used, where the specific enzyme is substituted by a non-specific protein BSA to ensure equality in the two devices. (b) Calibration curve of the Wheatstone bridge lactate sensor for three different devices. The data points are extracted upon consecutive addition of 1X PBS containing increasing lactate concentrations. The normalized response is* $NR = {}^{\Delta V_{out}}/_{\Delta V_{out,max}}$. *The supply voltage is* $V_{supply} = -2.3\,\mathrm{V}$ *for load resistors of* $R_{load} = 180\,\Omega$. *The gate voltage is kept constant at* $V_{GS} = 200\,\mathrm{mV}$. *(c) Titration curve of one selected Wheatstone bridge lactate sensor after successive addition of media collected from cells cultured at different concentrations for 24 hours (from* 10^1 *to* 10^5 *PBMC, the point at corresponds to fresh culture media). The inset shows the a zoom in of the same data to highlight the onset of lactate detection.*

remains zero when equal voltages are applied to both gates, after a certain stabilization time. The observed difference in the response time for the different drain load values is related to their respective aspect ratio (${}^{W}/_{L} = 5$ for $R_{\mathrm{load}} = 70\,\Omega$ vs. ${}^{W}/_{L} = 1.7$ for $R_{\mathrm{load}} = 190\,\Omega$). The changing voltage drop across the resistor and the resulting change in the current needs to equilibrate accordingly. The gain can be extracted as ${}^{\Delta V_{\mathrm{out}}}/_{\Delta V_{\mathrm{GS}}} = 0.4$ for $R_{\mathrm{load}} = 70\,\Omega$ and ${}^{\Delta V_{\mathrm{out}}}/_{\Delta V_{\mathrm{GS}}} = 0.5$ for $R_{\mathrm{load}} = 190\,\Omega$. For our enzymatic sensing approach, higher sensitivity (i.e. higher gain) is more important than high speed, thus we chose the higher drain load for the remainder of this study.

One key advantage of the Wheatstone bridge sensor circuit is the inherent background subtraction. When working with low volume samples, evaporation of the liquid results in a drift in I_{D}. Additionally, electro-oxidizable compounds present in the sample, as in the case of cell culture media, can induce changes in I_{D} due to direct electron transfer at the gate thus leading to an effective dedoping of the PEDOT:PSS material [Strakosas, 2016]. When changing the sample from a phosphate-buffered saline solution

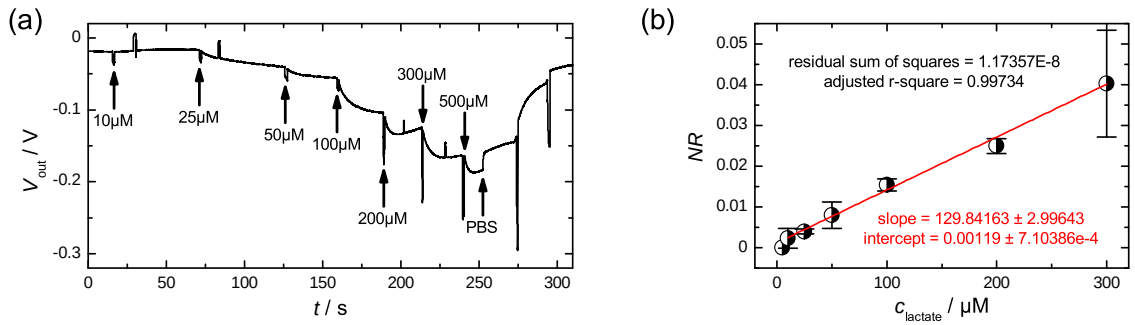

Figure 4.4: *(a) Raw data for one selected calibration curve. The addition of the different lactate concentrations is indicated with arrows. After washing with PBS, the initial value of the output voltage is almost retrieved. (b) Linear interpolation of the calibration curve. The adjusted R-squared value indicates a clear linear regression. This is used to calculate the lactate concentration from the normalized response of the Wheatstone bridge sensor.*

(PBS) to cell culture media, the response of the single OECTs in our device is in the range of 100 mV (corresponding to a change of $\Delta I_D \approx 0.5$ mA), whereas the baseline of the bridge remains fairly constant (Figure 4.1e). The observed spikes are due to electrolyte perturbation as a result of consecutive pipetting of the two wells. After rinsing with PBS, the original operation point of each individual OECT is retrieved. Note also the stability in V_{out}, while the single OECTs have not reached steady state operation yet (0 s to 50 s).

Figure 4.3a shows a depiction of our Wheatstone bridge lactate sensor. The dashed line indicates the reference (left) and the sensing (right) branch of the bridge. To render our sensor specific to lactate, we employed a biofunctionalization scheme at the gate of the sensing OECT based on our previous work [Pappa, 2016], by using an oxidase type enzyme (lactate oxidase) along with an electrochemical mediator. The enzyme/mediator complex is immobilized at the gate electrode of the OECT. An identical biofunctionalization scheme is applied to the gate electrode of the reference OECT by replacing the specific oxidase with a non-specific protein (bovine serum albumin), thus ensuring a similar surface environment and response time.

A calibration curve of lactate in buffer (1X PBS) is derived from the chronopotentiometric response of the Wheatstone bridge sensor after successive additions of increasing concentrations into the wells of both OECTs (Figure 4.3b). For ease of comparison between different devices, we normalize our response as the change in V_{out} divided by the maximum possible change, i.e., when I_D drops to zero and all potential would drop on the OECT. Since our V_{supply} is generally much higher than the operation point of the OECT, the normalized response tends to have small values. The calibration curve shows a linear behavior in the range of 30 µM to 300 µM and a detection limit of down to 10 µM can be extracted. The raw data for one representative calibration measurement

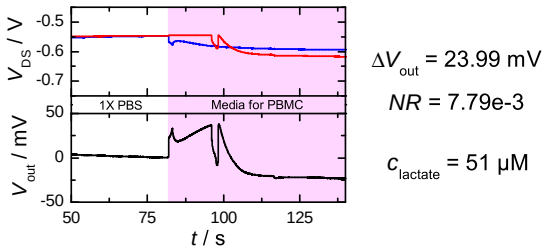

Figure 4.5: *Estimation of the lactate concentration present in media for peripheral blood mononuclear cells. The lactate concentration is extracted from the normalized response via a linear interpolation of the calibration curve (see Figure 4.5).*

is shown in Figure 4.4.

To demonstrate the sensitivity of our device, we performed a titration curve (Figure 4.3c), assessing the response of the device to an accumulation of lactate in cell media, collected after incubation with increasing numbers of peripheral blood mononuclear cells (PBMC) for 24 h. As baseline, fresh cell culture media is used. In one chronopotentiometric measurement, we successively add samples harvested from a different number of cells, starting from the lowest concentration. The titration curve shows an onset of response from medium incubated with between 10 to 100 cells. From this, we can estimate a detection limit of lactate produced by a few 10^s of cells (estimated to be $\approx 10\,\mu M$ from the calibration curve). The background concentration of lactate in fresh media is estimated to be about $50\,\mu M$ (Figure 4.5) but this is not perceptible in the measurements due to the reference based sensing mechanism of our circuit.

Figure 4.6a represents a typical chronopotentiometric recording in cell-derived samples. On the top is shown the individual response of each branch of the bridge and on the bottom the subtraction of those signals. Due to the two separate wells, a short delay between the exchanges of the sample electrolyte in both wells is observed, which leads to a temporary rise in V_{out}. This does not reflect any biological activity. As each cell line requires specific culture media that contains different nutrients (including lactate) in various concentrations, for each measurement we use the corresponding culture media as a baseline. The difference in the baseline of the media vs. the sample gives a direct measure of the lactate produced by the cells. Note that V_{out} returns to its initial value, once the device is rinsed with PBS, indicating that the device operation is not affected by the addition of complex media and the sensor can be reused for several measurements.

As already mentioned, a common feature of cancer cells is the enhanced rate of glycolysis, where glucose gets converted into pyruvate, and is aerobically fermented into lactic acid even under normoxia [Doherty, 2013; Liberti, 2016]. Indeed, Brand et al. recently showed that human melanoma metastases were found to exhibit a “Warburg

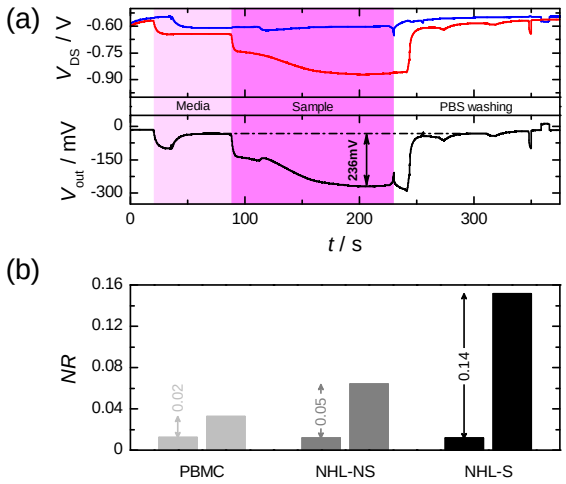

Figure 4.6: *(a) Typical chronopotentiometric recording for lactate analysis with the Wheatstone bridge sensor. The addition of media before incubation (light pink) and after incubation with cells of interest (dark pink) and the washing with 1X PBS solution is indicated in the center of the graph. The difference between the baseline of bare media and the response due to the sample reflects the lactate amount produced by the cells. The red (blue) line shows the operation point of the sensing (reference) OECT. (b) Comparison of lactate production from peripheral blood mononuclear cells versus unstimulated and stimulated primary non-Hodgkin's lymphoma cells (left to right). The left bar corresponds to media before incubation with cells and the right bar to media in which cells grew for 24 hours. The supply voltage* $V_{supply} = -2.3\,\mathrm{V}$ *for load resistors of* $R_{load} = 180\,\Omega$.

phenotype" with high lactate measured both intracellularly and extracellularly [Brand, 2016]. This reinforces our hypothesis that electronic detection methods may be used in the future for cancer diagnostics, for example for predicting metastatic potential. The advantage of our reference based sensor circuit is in providing higher sensitivity for such kind of *in vitro* applications, while allowing for a more accurate lactate production analysis, even in the harsh sensing milieu that is provided by complex cell media. We thus used our platform to investigate the lactate produced by cancer cells and normal cells grown under similar conditions. Figure 4.6b shows the measured lactate, produced from malignant samples, specifically samples from a non-Hodgkin's lymphoma (NHL) patient. These are composed of lymphocytes, notably malignant B lymphocytes known to secrete a high amount of lactate in comparison to normal PBMCs [Jurišić, 2004]. For the analysis, we use culture media incubated with a population of 10^4 cells for 24 hours. We compare both the unstimulated as well as the stimulated samples, where the stimulus promotes lymphocyte proliferation. The reference is a non-cancerous PBMC culture, mainly composed of lymphocytes, under similar conditions (10^4 cells, 24 h). The normalized response for the PBMC is $NR = 0.02$, which from a linear interpolation of the calibration curve in Figure 4.3b (Figure 4.4) can be

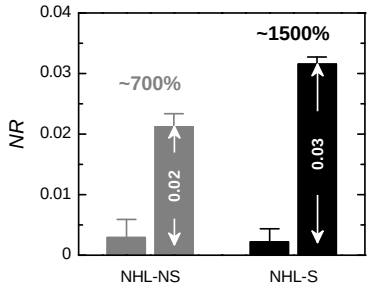

OP	NHL-NS	NHL-S
-0.35 V	739 %	1467 %
-0.60 V	535 %	1315 %

Figure 4.7: *Normalized response for medium from unstimulated (NS) and stimulated (S) non Hodgkin's lymphoma samples recorded at a lower operation point ($OP = -0.35\,\mathrm{V}$). The left column shows the lactate concentration of fresh medium and the right column the lactate concentration of the sample. The overall response is much lower due to the decreased amplification at the lower operation point. However, the percentage-wise increased lactate production of sample versus reference media are comparable to the data recorded at higher operation point (extracted from 4.6b).*

estimated to a lactate concentration of $c_{\mathrm{lactate}} \approx 140\,\mu\mathrm{M}$. The unstimulated lymphoma cells show a normalized response of $NR = 0.05$, hence more than twice the lactate concentration $c_{\mathrm{lactate}} \approx 370\,\mu\mathrm{M}$. Finally, the stimulated lymphoma cells show $NR = 0.14$, which correlates with a lactate concentration of $c_{\mathrm{lactate}} \approx 1\,\mathrm{mM}$ (the raw data of this measurement is shown in Figure 4.6a). We note, however, that this lies beyond the measured range of the calibration curve and saturation of our enzyme based sensor device is to be expected. Nonetheless, this value lies significantly above the unstimulated lymphoma cells, which can be explained by the fact that the stimulation process significantly enhanced cell proliferation and thus metabolic activity. We also measured more samples with the Wheatstone bridge sensor set at a lower operation point and we could see a similar trend for the unstimulated and stimulated samples, even though the absolute values of the device recordings are much lower (Figure 4.7). This emphasizes the fact that an optimized operation point of the device can result in the enhanced amplification.

4.3 Conclusion

In conclusion, the sensitivity of the device presented in this paper allows for *ex vivo* detection of a broad range of lactate concentrations, from as lithe as 10^{s} of non-malignant cells in "resting" conditions, i.e. cells with basal metabolic activity, to cells with strong metabolic activity, here stimulated tumor cells. The OECT has proven to provide highly sensitive metabolite detection due to its high current modulation in response to a change in the gate bias while the Wheatstone bridge sensor circuit provides an inherent background subtraction, thus ensuring elimination of any interference arising

from other factors (i.e., electro-oxidizable compounds, electrolyte evaporation etc). As a proof-of-concept, the lactate produced from cultures of healthy PBMC and malignant non-Hodgkin's lymphomas was compared. An elevated lactate production was indeed monitored in the cancer cells, confirming their intrinsic enhanced glycolytic metabolic activity, even in unstimulated conditions. To our knowledge, this is the first time that such a miniaturized sensor circuit has been applied to clinically relevant testing protocols that are important to follow tumor evolution or treatment efficiency in cancer patients [Lee, 2013].

4.4 Experimental Section

Device Fabrication (a) The Parylene-C devices in Figure 1b are fabricated according to reference [Sessolo, 2013]. (b) For the Wheatstone bridge sensor, a lift-off process using photolithographic patterning (plastic mask, Selba S.A.) of negative photoresist (S1813, 3500 rpm, 35 s; softbake 110 °C, 60 s; SUSS MJB4 i-line 65 mJ cm^{-2}; MF-26 developer, 30 s) and metal evaporation of chromium (10 nm) and gold (160 nm) defines the connection pads and interconnects. PEDOT:PSS solution (19 mL Clevios PH-1000, Heraeus Holding GmbH; 1 mL ethylene glycol, Sigma Aldrich; 50 µL dodecyl benzene sulfonic acid, Acros Organics; 1 wt% (3-glycidyloxypropyl) trimethoxysilane, Sigma Aldrich) is spuncast (1500 rpm, 30 s) and hardbaked (125 °C, 60 min) to generate a homogeneous film (100 nm). PEDOT:PSS was patterned using a fluorinated negative photoresist (OSCoR 5001, Orthogonal Inc.) that does not degrade the polymer during fabrication. We spuncast the photoresist (1 mL per glass slide, 1200 rpm, 35 s), softbaked (65 °C, 60 s), exposed (i-line 63 mJ cm^{-2}), post-exposure baked (90 °C, 60 s) and developed (Developer 100, Orthogonal Inc., double puddle 2 s × 25 s). Dry etching (150 W, O_2 50 sccm, CHF_3 5 sccm, 90 s) and stripping (Stripper 903, Orthogonal Inc., double puddle 2 s × 60 s) defines channel and drain load resistors. An insulator (DE1 Orthogonal Inc.) is patterned via spincasting (2000 rpm, 60 s), softbaking (90 °C, 60 s), exposing (i-line 149 mJ cm^{-2}), post-exposure bake (90 °C, 60 s) and develop (developer 100, Orthogonal Inc., double puddle 2 s × 45 s). The different fabrication steps are schematically represented in Figure 4.8.

Device characterization IV curves were recorded using a Keithley 2612A dual SourceMeter. All other recordings were done with a National Instruments PXIe-1062Q system at 50 Hz sampling rate (isolated analog output NI PXIe-4322 for supply and gate voltage, digital multimeter NI PXI-4071 for measuring output voltage).

Biofunctionalization We used a protocol of enzyme/mediator (lactate oxidase/chitosan-ferrocene) immobilization on the PEDOT:PSS gate as shown in an earlier publica-

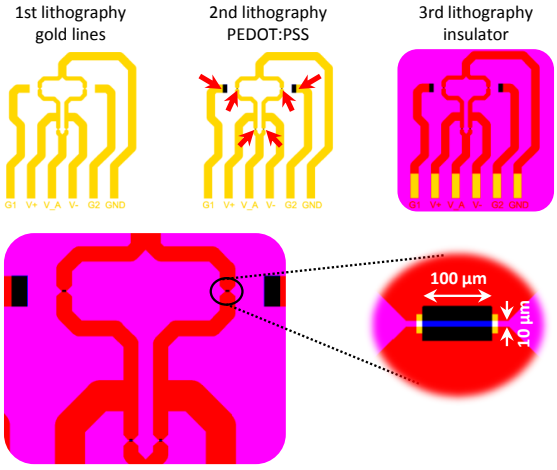

Figure 4.8: *Fabrication layout for photolithography of the Wheatstone bridge sensor. The different colors indicate UV exposure for the different lithography steps. The first lithography step defines the lead lines with a lift-off process of a positive photoresist (Shipley S1813). The second lithography step defines the PEDOT:PSS active area via dry etching while protecting the gate, the channel and the drain load resistor with a negative fluorinated photoresist (Orthogonal OSCOR 5001). The red arrows indicate the two OECT channels (top) and drain load resistors (bottom). The third lithography step patterns the insulator to open the gate, the channel, the drain load resistor and contact pads (Orthogonal Neg1). The zoomed images depict the planar configuration of the OECT as well as the geometry of the active area. The channel of the OECT is defined as* $W/L = 100\,\mu m/10\,\mu m$ *with an overlap of* $20\,\mu m$ *between gold and PEDOT:PSS. The insulator window, that defines the area of the PEDOT:PSS in contact with electrolyte, has a dimension of* $120\,\mu m^2 \times 30\,\mu m^2$ *to allow for good alignment during fabrication. The whole device is covered with a* $5\,mm$ *layer of polydimethylsiloxane (PDMS), within which we introduced two wells for the two OECTs. This allows for separate gating of both OECTs, and encapsulation of the drain load resistors.*

tion [Pappa, 2016]. The enzyme-mediator complex is covalently attached to the gate via epoxy terminated self-assembled monolayers ((3-glycidyloxypropyl)trimethoxysilane) on top of the oxygen plasma treated PEDOT:PSS surface. In the presence of the analyte (lactate), catalysis at the enzyme (lactate oxidase) results in the generation of an electron and a further dedoping of the PEDOT:PSS channel (Figure 4.9).

Lactate measurements We apply $V_{GS} = 200\,mV$ on both OECT gates and a constant supply voltage for a target operation point of $OP = -600\,mV$. $30\,\mu L$ 1X PBS solution is added into each well and when the output signal is stable, PBS is substituted by an equal amount of cell culture media (this sets the baseline of the measurement). After signal stabilization (≈ 1 minute), the solution is substituted with the sample of interest. Finally, the device is rinsed by consecutively exchanging the liquid in each well with $30\,\mu L$ of fresh 1X PBS until the device reaches the initial operation point.

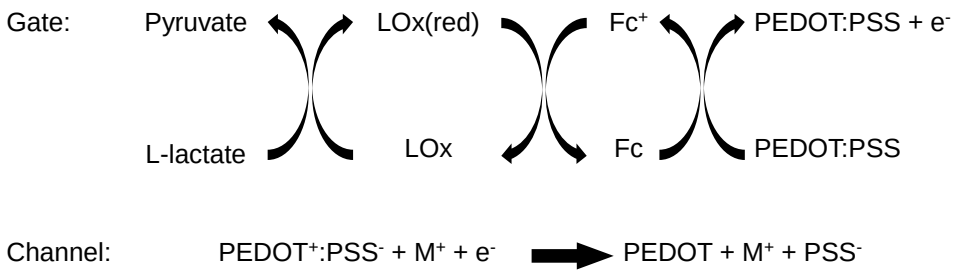

Figure 4.9: *Reaction cycles at the enzyme/mediator functionalized gate electrode, in the presence of the analyte (lactate) and the subsequent reaction at the channel.*

Sample preparation PBMCs were obtained from volunteers and anonymous donors of *Etablissement Français du Sang*. Peripheral leukocytes were isolated by Ficoll density gradient centrifugation (Axis-Shield PoC AS, Norway). The mononuclear cells were washed twice, counted and conserved in RPMI 1640 (GIBCO, InvitroGen) supplemented with 10 % heat-inactivated fetal calf serum (Lonza, Belgium) at a concentration of 1.1×10^6 cells mL^{-1}. Lymph node biopsies, from B-NHL patients, were mechanically disrupted and passed through a 100 µm nylon filter (BD Bioscience) to obtain a suspension of mononuclear cells. Cells were washed twice, counted and conserved in RPMI1640 supplemented with 10 % heat-inactivated fetal calf serum at a concentration of 1.1×10^6 cells mL^{-1}. Cells suspension (PBMC or B-NHL cells) were used in culture experiments in RPMI 10 % FCS with or without PolyIg mix (2 µg mL^{-1}) and CpG (1.25 µg mL^{-1}) stimuli. The supernatants were harvested after incubation of 24 h at 37 °C in 5 % CO_2. Supernatants were briefly spun (>20 000 G) then filtered through a 0.2 µm mesh. All samples have been diluted 1:1 in 1X PBS. The study was approved by the ethical board of the Paoli-Calmettes institute (Comité d'Orientation Stratégique, Marseille, France). Patients provided informed consent in accordance with the Declaration of Helsinki.

References

[Braendlein, 2016] M. Braendlein, T. Lonjaret, P. Leleux, J.-M. Badier, and G. G. Malliaras: "*Voltage Amplifier Based on Organic Electrochemical Transistor*", Advanced Science (2016), p. 1600247.

[Brand, 2016] A. Brand, K. Singer, G. E. Koehl, M. Kolitzus, G. Schoenhammer, A. Thiel, C. Matos, C. Bruss, S. Klobuch, K. Peter, M. Kastenberger, C. Bogdan, U. Schleicher, A. Mackensen, E. Ullrich, S. Fichtner-Feigl, R. Kesselring, M. Mack, U. Ritter, M. Schmid, C. Blank, K. Dettmer, P. J. Oefner, P. Hoffmann, S. Walenta, E. K. Geissler, J. Pouyssegur, A. Villunger, A. Steven, B. Seliger, S. Schreml, S. Haferkamp, E. Kohl, S. Karrer, M. Berneburg, W. Herr, W. Mueller-Klieser, K. Renner, and M. Kreutz: "*LDHA-Associated Lactic Acid Production Blunts Tumor Immunosurveillance by T and NK Cells*", Cell Metabolism (2016).

[Clark, 1962] L. C. Clark and C. Lyons: "*Electrode systems for continuous monitoring in cardiovascular surgery*", Annals of the New York Academy of sciences **102** (1962), pp. 29–45.

[Deng, 2014] H. Deng, A. K. L. Teo, and Z. Gao: "*An interference-free glucose biosensor based on a novel low potential redox polymer mediator*", Sensors and Actuators B: Chemical **191** (2014), pp. 522–528.

[Doherty, 2013] J. R. Doherty and J. L. Cleveland: "*Targeting lactate metabol-ism for cancer therapeutics*", Journal of Clinical Investigation **123** (3, 2013), pp. 3685–3692.

[Gao, 2016] W. Gao, S. Emaminejad, H. Y. Y. Nyein, S. Challa, K. Chen, A. Peck, H. M. Fahad, H. Ota, H. Shiraki, D. Kiriya, D.-H. Lien, G. A. Brooks, R. W. Davis, and A. Javey: "*Fully integrated wearable sensor arrays for multiplexed in situ perspiration analysis*", Nature **529** (27, 2016), pp. 509–514.

[Henry, 2012] N. L. Henry and D. F. Hayes: "*Cancer biomarkers*", Molecular Oncology **6** (2012), pp. 140–146.

[Jurišić, 2004] V. Jurišić, G. Konjević, R. Jančić-Nedeljkov, M. Sretenović, B. Banićević, M. Colović, and I. Spužić: "*The comparison of spontaneous LDH release activity from cultured PBMC with sera LDH activity in non-Hodgkin's lymphoma patients*", Medical Oncology **21** (2004), pp. 179–185.

[Kalia, 2015] M. Kalia: "*Biomarkers for personalized oncology: recent advances and future challenges*", Metabolism **64** (2015), S16–S21.

[Kergoat, 2012] L. Kergoat, B. Piro, M. Berggren, G. Horowitz, and M.-C. Pham: "*Advances in organic transistor-based biosensors: from organic electrochemical transistors to electrolyte-gated organic field-effect transistors*", Analytical and Bioanalytical Chemistry **402** (2012), pp. 1813–1826.

[Khodagholy, 2013a] D. Khodagholy, T. Doublet, P. Quilichini, M. Gurfinkel, P. Leleux, A. Ghestem, E. Ismailova, T. Hervé, S. Sanaur, C. Bernard, and G. G. Malliaras: "*In vivo recordings of brain activity using organic transistors*", Nature Communications **4** (2013), p. 1575.

[Khodagholy, 2013b] D. Khodagholy, J. Rivnay, M. Sessolo, M. Gurfinkel, P. Leleux, L. H. Jimison, E. Stavrinidou, T. Herve, S. Sanaur, R. M. Owens, and G. G. Malliaras: "*High transconductance organic electrochemical transistors*", Nature Communications **4** (12, 2013), p. 2133.

[Kittlesen, 1984] G. P. Kittlesen, H. S. White, and M. S. Wrighton: "*Chemical derivatization of microelectrode arrays by oxidation of pyrrole and N-methylpyrrole: fabrication of molecule-based electronic devices*", Journal of the American Chemical Society **106** (1984), pp. 7389–7396.

[Lafleur, 2016] J. P. Lafleur, A. Jönsson, S. Senkbeil, and J. P. Kutter: "*Recent advances in lab-on-a-chip for biosensing applications*", Biosensors and Bioelectronics **76** (2016), pp. 213–233.

[Lee, 2013] S.-C. Lee, M. Marzec, X. Liu, S. Wehrli, K. Kantekure, P. N. Ragunath, D. S. Nelson, E. J. Delikatny, J. D. Glickson, and M. A. Wasik: "*Decreased lactate concentration and glycolytic enzyme expression reflect inhibition of mTOR signal transduction pathway in B-cell lymphoma: LACTATE MRS DETECTS mTOR INHIBITION*", NMR in Biomedicine **26** (2013), pp. 106–114.

[Liao, 2015] C. Liao, C. Mak, M. Zhang, H. L. W. Chan, and F. Yan: "*Flexible Organic Electrochemical Transistors for Highly Selective Enzyme Biosensors and Used for Saliva Testing*", Advanced Materials **27** (2015), pp. 676–681.

[Liberti, 2016] M. V. Liberti and J. W. Locasale: "*The Warburg Effect: How Does it Benefit Cancer Cells?*", Trends in Biochemical Sciences **41** (2016), pp. 211–218.

[Liu, 2012] Y. Liu, Z. Matharu, M. C. Howland, A. Revzin, and A. L. Simonian: "*Affinity and enzyme-based biosensors: recent*

advances and emerging applications in cell analysis and point-of-care testing", Analytical and Bioanalytical Chemistry **404** (2012), pp. 1181–1196.

[Luka, 2015] G. Luka, A. Ahmadi, H. Najjaran, E. Alocilja, M. DeRosa, K. Wolthers, A. Malki, H. Aziz, A. Althani, and M. Hoorfar: "*Microfluidics Integrated Biosensors: A Leading Technology towards Lab-on-a-Chip and Sensing Applications*", Sensors **15** (1, 2015), pp. 30011–30031.

[Pappa, 2016] A.-M. Pappa, V. F. Curto, M. Braendlein, X. Strakosas, M. J. Donahue, M. Fiocchi, G. G. Malliaras, and R. M. Owens: "*Organic Transistor Arrays Integrated with Finger-Powered Microfluidics for Multianalyte Saliva Testing*", Advanced Healthcare Materials (2016).

[Rivnay, 2013] J. Rivnay, P. Leleux, M. Sessolo, D. Khodagholy, T. Hervé, M. Fiocchi, and G. G. Malliaras: "*Organic Electrochemical Transistors with Maximum Transconductance at Zero Gate Bias*", Advanced Materials **25** (2013), pp. 7010–7014.

[Rivnay, 2014] J. Rivnay, R. M. Owens, and G. G. Malliaras: "*The Rise of Organic Bioelectronics*", Chemistry of Materials **26** (14, 2014), pp. 679–685.

[Rivnay, 2015] J. Rivnay, P. Leleux, M. Ferro, M. Sessolo, A. Williamson, D. A. Koutsouras, D. Khodagholy, M. Ramuz, X. Strakosas, R. M. Owens, C. Benar, J.-M. Badier, C. Bernard, and G. G. Malliaras: "*High-performance transistors for bioelectronics through tuning of channel thickness*", Science Advances **1** (22, 2015), e1400251–e1400251.

[Sessolo, 2013] M. Sessolo, D. Khodagholy, J. Rivnay, F. Maddalena, M. Gleyzes, E. Steidl, B. Buisson, and G. G. Malliaras: "*Easy-to-Fabricate Conducting Polymer Microelectrode Arrays*", Advanced Materials **25** (18, 2013), pp. 2135–2139.

[Sessolo, 2014] M. Sessolo, J. Rivnay, E. Bandiello, G. G. Malliaras, and H. J. Bolink: "*Ion-Selective Organic Electrochemical Transistors*", Advanced Materials **26** (2014), pp. 4803–4807.

[Shim, 2009] N. Y. Shim, D. A. Bernards, D. J. Macaya, J. A. DeFranco, M. Nikolou, R. M. Owens, and G. G. Malliaras: "*All-Plastic Electrochemical Transistor for Glucose Sensing Using a Ferrocene Mediator*", Sensors **9** (4, 2009), pp. 9896–9902.

[Strakosas, 2014] X. Strakosas, M. Sessolo, A. Hama, J. Rivnay, E. Stavrinidou, G. G. Malliaras, and R. M. Owens: "*A facile biofunctionalisation route for solution processable conducting polymer devices*", J. Mater. Chem. B **2** (2014), pp. 2537–2545.

[Strakosas, 2016] X. Strakosas, M. Huerta, M. J. Donahue, A. Hama, A.-M. Pappa, M. Ferro, M. Ramuz, J. Rivnay, and R. M. Owens: "*Catalytically enhanced organic transistors for in vitro toxicology monitoring through hydrogel entrapment of enzymes*", Journal of Applied Polymer Science (2016).

[Svensson, 2008] P.-O. Svensson, D. Nilsson, R. Forchheimer, and M. Berggren: "*A sensor circuit using reference-based conductance switching in organic electrochemical transistors*", Applied Physics Letters **93** (2008), p. 203301.

[Taylor, 2009] P. G. Taylor, J.-K. Lee, A. A. Zakhidov, M. Chatzichristidi, H. H. Fong, J. A. DeFranco, G. G. Malliaras, and C. K. Ober: "*Orthogonal Patterning of PEDOT:PSS for Organic Electronics using Hydrofluoroether Solvents*", Advanced Materials **21** (12, 2009), pp. 2314–2317.

[Updike, 1967] S. J. Updike and G. P. Hicks: "*The Enzyme Electrode*", Nature **214** (3, 1967), pp. 986–988.

[Walenta, 2000] S. Walenta, M. Wetterling, M. Lehrke, G. Schwickert, K. Sundfør, E. K. Rofstad, and W. Mueller-Klieser: "*High lactate levels predict likelihood of metastases, tumor recurrence, and restricted patient survival in human cervical cancers*", Cancer Research **60** (15, 2000), pp. 916–921.

[Walenta, 2002] S. Walenta, T. Schroeder, and W. Mueller-Klieser: "*Metabolic mapping with bioluminescence: basic and clinical relevance*", Biomolecular Engineering **18** (2002), pp. 249–262.

[Warburg, 1956] O. Warburg: "*On the origin of cancer cells*", Science **123** (1956), pp. 309–314.

[Zhang, 2016] S. Zhang, E. Hubis, C. Girard, P. Kumar, J. DeFranco, and F. Cicoira: "*Water stability and orthogonal patterning of flexible micro-electrochemical transistors on plastic*", J. Mater. Chem. C **4** (2016), pp. 1382–1385.

[Zoulias, 2004] E. Zoulias, E. Varkaraki, N. Lymberopoulos, C. N. Christodoulou, and G. N. Karagiorgis: "*A review on water electrolysis*", TCJST **4** (2004), pp. 41–71.

Chapter 5

Conclusion and Outlook

The present work has demonstrated the capabilities of organic electronic materials to improve the biotic-abiotic interface and enhance the sensitivity of *in vitro* and *in vivo* bioelectronic devices. In particular, the conducting polymer poly(3,4-ethylenedioxythiophene) doped with polystyrene sulfonate has been implemented in a transistor architecture to provide an electrolyte gated organic electrochemical transistor (OECT) that gives an electrical readout signal to biological changes expressed in ionic currents. Moreover, the OECT has been implemented into simple sensor circuit layouts to improve the sensitivity and selectivity even further. A general introduction to the field of bioelectronics and the impact of organic materials has been presented in Chapter 1, along with a detailed explanation of the operation principle and the fabrication methods of the OECT. In particular, a novel approach for direct lithographic patterning of organic materials with hydrofluorether based chemicals has been opposed to the traditional peel-off method using parylene C. Furthermore, the essential sensor circuits used in this manuscript have been introduced in this chapter. The remaining chapters of the manuscript have been based on published journal articles that present the contribution to the scientific community. At this point, the author would like to summarize these chapters and give a short outlook as to what could be improved.

Chapter 2 reported on a novel *in vitro* platform capable of accurately detecting the concentration of multiple metabolites simultaneously in one single sample. This so called *multianalyte platform* comprised one OECT for each metabolite to be detected. The OECTs have been functionalized with an enzyme that catalyses the oxidation of the metabolite and a mediator that shuttles the generated electron to the gate circuit of the transistor. Due to this functionalization approach, each OECT has to be controlled with a local gate. To avoid electrical cross talk in between the different OECTs in the same electrolyte and prevent so called *ground loops* that would result in a loss of selectivity of each OECT, an inductively decoupled voltage supply unit had to be used to provide

the source drain and source gate voltage of the transistors. This inductive decoupling of each channel ensures that the electrons generated due to the enzyme reaction with the metabolite are only circulating in the gate circuit of the corresponding OECT. In a first part, the sensitivity of each funtionalized OECT towards the corresponding metabolite has been presented. The metabolites of interest were glucose, lactate and cholesterol chosen for their significance in sports but also as indicators for diseases such as diabetes. As a proof of concept, a finger-powered microfluidic has been used to run the sample across the transistor array and glucose, lactate and cholesterol levels have been measured in saliva samples under different physiological conditions. This chapter served as an introduction to enzyme based metabolite detection with OECTs that will also be used in Chapter 4. As the enzyme based mechanism is reversible, i.e. the drain current of the OECT will reach its initial level when washing out the metabolite, an integration of the platform with a microfluidic system to provide a constant flow of the sample, could allow for realtime online analysis of metabolite levels during sport events. The capabilities of flexible device fabrication are given and have been demonstrated for other applications. Therefore, the multianalyte platform could be integrated in a form factor that makes it easy to use.

In Chapter 3, the use of the OECT for electrophysiological recordings has been demonstrated. The particularity was that by integrating the OECT with a simple resistor in series (drain load), a voltage readout signal could be achieved as opposed to the current readout signal provided by the transistor itself. This simple circuit leads to a voltage amplifier, where the voltage signal picked up at the gate electrode of the OECT results in a change in the drain current that gets converted to a voltage signal at the drain load. Therefore, the device can be easily used in an already existing clinical setup and allows for a comparison with regular medical electrodes. The advantage of the OECT lies in the active amplification at the site of origin of the biological activity. In a first part, the voltage amplifier has been characterized thoroughly in a sodium chloride solution. The effect of the drain load on the device performance has been analysed in the two operation regimes of the transistor (linear regime and saturation regime). An analytical derivation based on transconductance and the drain conductance of the plain OECT without any drain load could relate the gain of the voltage amplifier system with the magnitude of the drain load. Depending on the operation regime of the OECT, a more or less performing amplification could be achieved. In particular, it has been found that the gain scales linearly with the drain load when operating the OECT in the saturation regime. With this detailed understanding of the system, in a second part electrocardiographic recordings could be achieved with an amplification of up to $30\,\mathrm{V\,V^{-1}}$. One drawback of this system is that the supply voltage also scales linearly with the magnitude of the drain load and voltages of up to 8.8 V had to be used to achieve such an amplification factor. Another point to mention is that the device presented in Chapter 3 has been used in an external setup, meaning that the voltage amplifier was not in direct contact with the skin, but rather

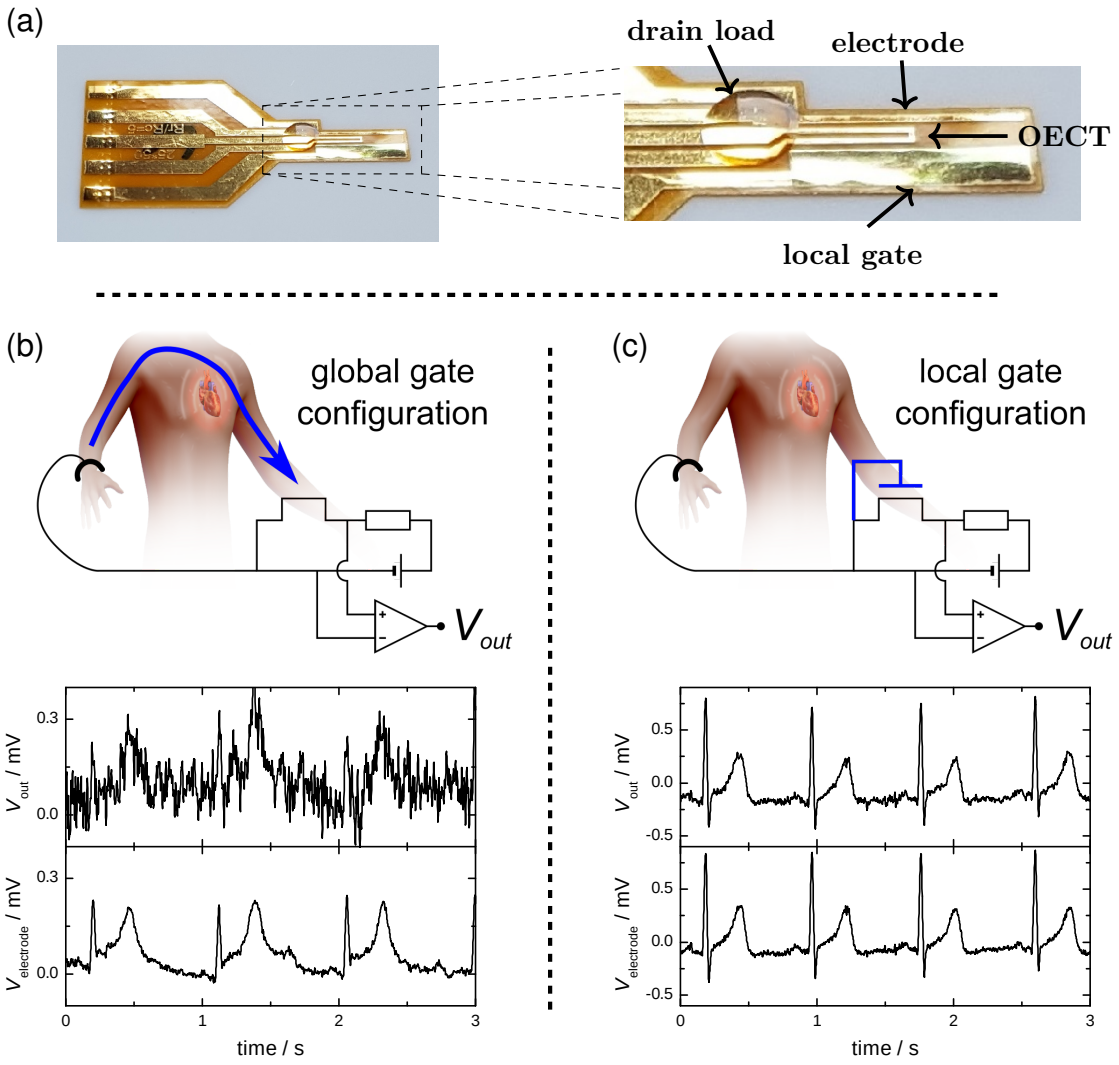

Figure 5.1: *(a) Images of a flexible active electrode with OECT and drain load resistor. A passive electrode of equal size to the OECT channel is also patterned on the device for comparison. The drain load is encapsulated with PDMS. The magnitude of the drain load is two times the channel resistance. The supply voltage is around* $-1\,\mathrm{V}$*. (b) Global gate configuration for electrophysiological recordings. The gate current is passing through the body to modulate the OECT. The reference electrode and the floating point of the organic voltage amplifier are connected to an external amplifier. The recordings of the active electrode show a very noisy signal compared to the passive electrode (possibly* $50\,\mathrm{Hz}$ *noise). (c) Local gate configuration. A local gate sets the operation point of the OECT and the local field potential modulates the channel. The recordings of the active electrode are almost identical to the passive electrode. All signals are filtered with a hardware highpass filter to cut the DC offset of the signal.*

the gate electrode of the OECT was connected to a medical electrode attached to the skin. Furthermore, the drain load resistor was not integrated onto the device but rather connected externally to allow for a quick change of the magnitude of the drain load. Therefore, a direct comparison to medical electrodes was not possible. As a continuation of the work presented in Chapter 3, effort has been made to provide a true so called *active organic electrode* based on the same principle. With the parylene C peel-off method, a flexible device comprising OECT and drain load fully integrated on a 25 µm thin Kapton substrate, as well as a passive PEDOT:PSS electrode of same size as the OECT channel has been fabricated (see Figure 5.1a). This allows for a direct comparison of the voltage amplifier system to a passive electrode. The preliminary results are presented in Figure 5.1b-c for two different configurations. The global gate configuration refers to the intuitive mounting for simple bipolar electrocardiographic recordings, i.e. one reference electrode (medical electrode on the right wrist) and one sensing electrode (OECT channel on the left wrist). In this configuration, the human body acts as the electrolyte and the physiological activity is modulating the voltage between gate electrode and OECT channel. However, when connecting the device in this configuration to the medical voltage recording equipment, a huge noise was introduced on the signal of the OECT voltage amplifier whereas the passive PEDOT:PSS electrode shows very nice recordings. It can be seen that the signal of the voltage amplifier reflects the PQRST complex associated with a healthy heart beat in the same way as the electrode, but it is almost hidden in the 50 Hz noise. The origin of this is unclear and further experiments are needed to figure out what is causing that noise. Maybe the resistive path of the gate circuit through the human body is picking up environmental noise that then gets amplified by the OECT. But since the recordings with the passive electrodes where good, this seems unlikely. Maybe the OECT is working at a very unfavourable operation point due to a potential different between the left and right wrist. At this point, no clear explanation can be given. Only a wrong connection setup can be excluded as this behaviour persisted for different devices recorded at different times. On the other hand, when using a so called local gate configuration, where the OECT is controlled via a PEDOT:PSS gate next to the OECT channel (Figure 5.1c), very nice recordings could be achieved. In fact, the recordings are almost identical to the nearby passive electrode with a slightly better signal-to-noise ratio for the passive electrode. This configuration corresponds to *in vivo* measurements done in rat brains, where a big metallic screw is mounted to the skull acting as reference and the OECT with a local gate is implanted inside the tissue. In such a configuration, the local gate is forcing the OECT to be at a fixed potential and voltage signals arising from neurons or in our case the human heart are transiently altering the ion distribution inside the OECT channel. However, when using a drain load, we assume that the drain contact of the OECT, that is in contact with the skin and that is a floating voltage point in the voltage amplifier circuit, acts also as a passive electrode picking up the physiological signal. This in turn alters the drain current of the OECT as the effective source drain bias is changed. And the change in the drain current gets converted to a voltage signal

at the drain load. Looking at the almost identical signal-to-noise ratio between the voltage amplifier and the passive electrode, we assume that in this configuration, the OECT is not used as a voltage amplifier but merely as a passive electrode, where the voltage gets converted to a current and back to a voltage. Therefore, a true active organic electrode with an enhanced signal-to-noise ratio that can outperform regular medical electrodes proves to be more difficult and further effort is needed to solve the presented issues. Nevertheless, the findings of this chapter can be directly applied to the Wheatstone bridge sensor circuit presented in Chapter 4 and for *in vitro* sensing applications the mentioned problems do not occur.

Chapter 4 is a combination of the enzyme based metabolite detection scheme presented in Chapter 2 and the voltage amplifier circuit presented in Chapter 3. In this chapter, two OECTs are implemented into a Wheatstone bridge circuit, which in essence is a parallel connection of two OECT voltage amplifiers. By differently functionalizing the two OECTs, one OECT can act as a reference (non specific protein functionalization) and the other can act as a sensor (in this case lactate oxidase functionalization). By differentially measuring both voltage amplifier systems (i.e. with a parallel connection), the output signal gives a background subtracted highly specific and accurate measure of the metabolite concentration in the electrolyte. Due to the reference branch of the bridge, any effect due to temperature, electrolyte evaporation, oxidizable compounds in the electrolyte, is filtered from the output signal and only the change due to the analyte of interest is reflected. This is presented in detail in the first part of the chapter. One key element was the use of hydrofluoroether based chemicals for the lithographic patterning of the organic materials. This way, a higher device homogeneity could be achieved which is essential for this differential device. If one OECT would perform differently than the other, a subtracting method has no meaning. In a second part of the chapter, the functionalization scheme was presented and the sensitivity of the sensor circuit towards lactate content in cell culture media was analyzed. Cell culture media generally has a lot of oxidizable compounds that lead to big interference in the OECT device performance. It could be shown that using the Wheatstone bridge sensor circuit, physiologically relevant concentrations of lactate produced from as few as 10s of cells can be detected. In order to demonstrate the utility of the device as label-free and cost-effective clinically relevant *in vitro* diagnostic tool, the lactate content in cell culture medium derived from cancer cells has been compared to healthy cells and an elevated lactate concentration could be found for the cancer cell sample. This is in accordance with recent findings that cancer cells show an enhanced rate of glycolysis due to highly proliferative cell growth. One drawback of this system is the use of two separate electrolyte reservoirs for the two branches of the Wheatstone bridge sensor circuit. This induces spikes in the output signal when adding the sample consecutively in the two wells. In order to circumvent this issue, new materials would have to be used for the conducting channel of the OECTs. PEDOT:PSS is a p-type depletion mode semiconductor. This means that the transistor is normally on and a positive gate volt-

age results in a dedoping of the organic semiconductor and therefore an attenuation of the drain current. This also means that the enzyme functionalization has to happen at the gate of the transistor, since the enzymatic oxidation leads to the generation of an electron that can only enter the electronic circuit at the positively charged gate. In a simplified picture, the voltage applied at the gate electrode has two potential drops, one at the gate-electrolyte interface and one at the electrolyte-source interface (see Figure 5.2). Assuming that both interfaces are identical, the effective gate voltage, i.e. the voltage that drives ions in and out of the conducting polymer, is exactly half of the applied gate voltage. When the enzymatic reaction with the metabolite is happening, an electron is provided to the system and the enzyme is left with a positive charge, therefore compensating for a negative ion at the gate-electrolyte interface. This means that the potential drop across the gate-electrolyte interface is smaller and therefore the effective gate voltage increases as more potential will drop across the electrolyte-source interface. If one were to use an accumulation mode material, such as recently synthesised by Nielsen et al. (DOI: 10.1021/jacs.6b05280), the opposite behaviour could be achieved. Here, the transistor is normally off and a negative gate voltage has to be applied to dope the material and allow for charge transport in the conducting channel. As the gate voltage is negative the enzymatic reaction will happen at the source contact. In a similar picture, the effective gate voltage will decrease upon enzyme oxidation. The overall effect will be the same as for the depletion mode transistor, meaning that the transistor will switch from a high conductive state to a lower conductive state (drain current will decrease) upon enzyme oxidation. However, due to the possibility to functionalize the transistor channel instead of the gate, two differently functionalized OECTs can now be controlled through the same gate. This means that implementing such a material into a Wheatstone bridge sensor circuit layout, a single electrolyte reservoir can be used along with a single gate. Experiments would be needed to confirm that reasoning and could provide an improvement in applicability. With a single electrolyte reservoir, cutaneous applications become feasible and for example multiple branches of the bridge (not only two) can be functionalized for different metabolites to provide a reference based multianalyte platform.

In conclusion, the OECT has been implemented into simple circuit layouts to provide more sensitive and more selective bioelectronic devices. This implementation provides a challenge to the device fabrication and a promising route has been demonstrated using hydrofluroether solvents. The application of such sensor circuits to real-life biomedical challenges, such as *in vitro* detection of multiple metabolites, *in vivo* detection of electrocardiographic signals or *in vitro* detection of lactate in cancer cell cultures, has shown the capability of organic electronic devices to extend the range of biomedical sensors and bring healthcare monitoring to the next level. Due to their cheap production costs and their miniaturized form factor, bioelectronic devices based on conducting polymers can allow for easy self-examination at home and a powerful integration with information technology devices can assess if medical aid should be consulted. This

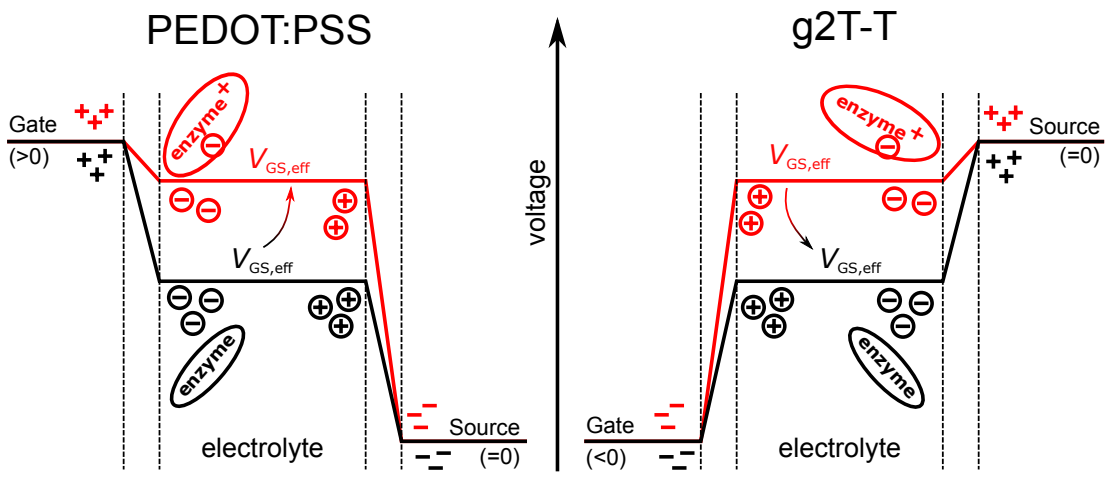

Figure 5.2: *Simplified potential profile for enzyme based sensing. As PEDOT:PSS is a p-type depletion mode material, a positive potential has to be applied at the gate to dedope the material and attenuate the charge transport. The effective gate voltage is defined as the potential difference between electrolyte and source contact. This determines the doping state of the transistor. For a neutral enzyme (black), the potential drop at the gate-electrolyte interface is equal to the electrolyte-source interface. Upon oxidation of the enzyme (red), the ion distribution is modified, as the enzyme compensates for one anion. This leads to a higher effective gate voltage. For g2T-T, a p-type accumulation mode material, a negative gate voltage has to be applied to dope the material and allow for charge transport. Upon enzyme oxidation, the magnitude of the effective gate voltage gets smaller.*

home based medical assessment can improve the life quality of our society.

Scientific Contributions

"Characterization and Simulation of Electrolyte-Gated Organic Field-Effect Transistors" *Katharina Melzer,* ***Marcel Braendlein****, Bogdan Popescu, Dan Popescu, Paolo Lugli, Giuseppe Scarpa*
DOI:10.1039/C4FD00095A, journal article in Faraday Discussions 174 (2014)

"Modeling of Electrolyte-Gated Organic Thin-Film Transistors for Sensing Applications" *Dan Popescu, Bogan Popescu,* ***Marcel Braendlein****, Katharina Melzer, Paolo Lugli*
DOI:10.1109/TED.2015.2485160, journal article in IEEE Transactions on Electron Devices 62 (2015)

"Organic Transistor Arrays Integrated with Finger-Powered Microfluidics for Multianalyte Saliva Testing" *Anna-Maria Pappa, Vincenzo Fabio Curto,* ***Marcel Braendlein****, Xenofon Strakosas, Mary Jocelyn Donahue, Michel Fiocchi, George Gregory Malliaras, Róisín Meabh Owens*
DOI:10.1002/adhm.201600494, journal article in Advanced Healthcare Materials 5 (2016)

"Voltage Amplifier Based on Organic Electrochemical Transistor" ***Marcel Braendlein****, Thomas Lonjaret, Pierre Leleux, Jean-Michel Badier, George Gregory Malliaras*
DOI:10.1002/advs.201600247, journal article in Advanced Science 4 (2016)

"Lactate Detection in Tumor Cell Cultures Using Organic Transistor Circuits" ***Marcel Braendlein****, Anna-Maria Pappa, Marc Ferro, Alexia Lopresti, Claire Acquaviva, Emilie Mamessier, George Gregory Malliaras, Róisín Meabh Owens*
DOI:10.1002/adma.201605744, journal article in Advanced Materials online (2017)

"Precise Patterning of Biocompatible Transistor Arrays Using Fluorinated Photoresist" *Marc Ferro, Pierre Leleux,* ***Marcel Braendlein****, Adel Hama, Olivier Lucas, Mary Jocelyn Donahue, Eric Di Pasquale, George Gregory Malliaras*
journal article in preparation

"A Multi-Parametric Organic Transistor Toolbox with Integrated Microfluidics for In-Line *in vitro* Cell Monitoring" *Vincenzo Fabio Curto, Bastien Marchiori, Adel Hama, Anna-Maria Pappa,* ***Marcel Braendlein****, Jonathan Rivnay, Michel Fiocchi, Marc Ramuz, Róisín Meabh Owens*
journal article in preparation

"Correlating Metabolic Levels to Epileptiform Activitiy with Implantable OECT Based *in vivo* Sensors" *Mary Jocelyn Donahue, Adam Williamson, Xenofon Strakosas,* ***Marcel Braendlein****, Marc Ferro, Christophe Bernard, Róisín Meabh Owens, George Gregory Malliaras*
journal article in preparation

"Active Organic Electrode for Electroencephalographic Recordings - A Comparison of PEDOT:PSS Based Electrodes and Electrochemical Transistors" *Thomas Lonjaret,* ***Marcel Braendlein****, Isabel del Agua Lopez, Jean-Michel Badier, George Gregory Malliaras, Esma Ismailova*
journal article in preparation

"Voltage Amplifier Based on Conducting Polymer Transistor", ***Marcel Braendlein****, Jonathan Rivnay, Pierre Leleux, Marc Ramuz, George Gregory Malliaras*
poster at the MRS Spring Meeting 2015, San Francisco, United States of America

"Voltage Amplifier Based on OECT for Electrophysiological Application" ***Marcel Braendlein****, Thomas Lonjaret, Pierre Leleux, Jean-Michel Badier, George Gregory Malliaras*
oral presentation at the International Winterschool on Bioelectronics 2016, Kirchberg, Austria

"Sensor Circuits for *in vitro* Bioelectronics" ***Marcel Braendlein****, Anna-Maria Pappa, Claire Acquaviva, Emilie Mamessier, George Gregory Malliaras, Róisín Meabh Owens*
oral presentation at the MRS Spring Meeting 2016, Phoenix, United States of America

Acknowledgements

Three years seems like a long time. But in the company of so many great scientists that not only helped me throughout my professional life but also became close friends, the time has passed by so quickly that I now look back and wonder. My achievements would be worth nothing without mentioning the people that made this possible and I would like thank each single one of them. If by any means, I unrightfully forget to mention your name in the following list, please be assured that it was not on purpose.

At this point, I am looking forward to new endeavours, away from a pure academic environment. But I am happy to have lived the experience of a PhD and without hesitation I would make the same choice, had the clock been turned back. The person that made this experience possible and to whom I owe the greatest thanks is my supervisor, Professor George Gregory Malliaras at the "Department of Bioelectronics" (BEL) at Gardanne, France. His guidance and instinct for fascinating science has helped me throughout my PhD and the academic freedom that he bestowed allowed me to mature scientifically in a way that came naturally. Thank you George.

In an equal manner, I would like to thank my co-supervisor, Professor Róisín Meabh Owens for her guidance during the second part of my PhD. Her invaluable experience with biology has broadened my horizon and helped finding a suitable application for the more engineering based work that I have performed during the first half of my PhD. I am happy to have seen her group grow steadily over the years and I hope I could help in this proliferative process. Thank you Róisín.

I am also deeply grateful for each and every member at BEL that accepted me as part of the family. Everyone knows that it is important to have an enjoyable working environment and that this tremendously impacts the productivity and creativity. And within BEL, I have always felt welcome and quickly made new friends. While some of those people have already left and pursued their own adventures, I hope that we will always keep in touch. Thank you Xeno, Eloïse, Margareth, Patrick, Yingxin, Dimitrios, Marc et Marc, Manu, Miriam, Timothee, Robin, Maria, Nathan, John, Liza, Charalampos, Yi, Julie, Gaëtan, Sahika, Amale, Esma, Michel, Adel, Adam, Jake, Sébastien, Seiichi, Mary, Rod, Susan, Mahmoudy, Jessamyn, Shahab, Loïg, Chris, Paschalis, Bastien, Jolien, Gerwin, Magali, David, Frederica, Husein, Clemens, Simon,

Carol, Kirsty, Isabel, Alexandra, Donata, Viviana, and Vincenzo.

In particular, I would like to emphasize the invaluable help of two colleagues at BEL, Anna-Maria Pappa and Thomas Lonjaret, who have helped me in finding suitable applications to be able to publish my work. While each of them offered different input that led to two individual projects, they have been the driving force and without their effort, the present manuscript would not have been possible. In fact, I put their scientific contribution to the publications above my own and I hope they know how deeply grateful I am. Thank you Anna-Maria, thank you Thomas.

I would also like to thank the Panaxium team, a promising start-up company working on bioelectronic devices, that were helping me a lot with the orthogonal patterning process. It was a pleasure to discuss those issues over countless lunch breaks. Thank you Pierre, Aimie and Brad.

Within the Marie Curie Actions program OrgBIO (grant number 607896), that not only funded my PhD but also provided a network of highly renowned scientist to be able to collaborate with, I have had the possibility to spend a few months at one of the industrial partners, Nanion Technologies in Munich. I would like to thank the whole group for their warm welcome and for their willingness to share their knowledge. I have learned so much during a short amount of time and I wouldn't want to miss that experience. Even though, the work there did not contribute to the present manuscript, the knowledge that I gained will help me in my future career. At this point, I would like to thank Krisztina, Leo, Matze and Sonja for their supervision and the rest of the Nanion group. Thank you.

The hospital "La Timone" in Marseille has always been a focal point where I could just go and test devices without any problem. Two laboratories have been especially helpful for my work and therefore, I would like to acknowledge the MEG group run by Jean-Michel Badier and the Physiology & Physiopathology of Brain Networks group run by Christophe Bernard. Thank you.

I would also like to thank the technical staff running the clean room at the "Centre Microélectronique de Provence" (CMP), in particular Gaëlle Rondeau, Thierry Camilloni, Sylvain Nolot, Cyril Calmes and Jessica Mazuir, for keeping things steady and trying to fix issues before they even occur. Without their work, none of the scientific output at BEL would be possible. Many thanks also go to the technical and administrative staff at CMP, to all the people that work in the background and that are essential for the functioning of the centre. Thank you all.

At long last, I thank my soon-to-be wife, Alexandra Besson, for her unconditional support and love that has carried me all the way throughout my PhD. You have been the rock, the irrevocable force, the everlasting constant that allowed me to concentrate fully on my work, knowing that when I come home you will be there. Thank you so much, mein Schatz.

École Nationale Supérieure des Mines
de Saint-Étienne

NNTº: 2017LYSEM007

Marcel Braendlein

Lithographic Fabrication, Electrical Characterization and Proof-of-Concept Demonstration of Sensor Circuits Comprising Organic Electrochemical Transistors for In Vitro and In Vivo Diagnostics

Speciality: Microelectronics

Keywords: Bioelectronics, Organic Electrochemical Transistor, PEDOT:PSS

Abstract:

Due to their outstanding mechanical, electrical and chemical properties, organic electronic devices based on conducting polymers can bridge the gap between the rigid silicon based read-out electronics and the soft biological environment and will have a huge impact on the medical healthcare sector. The recent advances in the field of organic semiconductors and microelectronics gave rise to a new discipline termed bioelectronics. This discipline deals with sensors for diagnostic purposes, ranging from metabolite detection and DNA recognition all the way to single neuronal firing events, and actuators for therapeutic purposes, through for example active local drug delivery inside the body or deep brain stimulation to cure neurological disorder. The use of organic materials such as the conducting polymer poly(3,4-ethylenedioxythiophene) polystyrene sulfonate (PEDOT:PSS) in the field of bioelectronics has brought about a variety of outstanding electronic biomedical devices, such as the organic electrochemical transistor (OECT), that have been implemented for both *in vitro* and *in vivo* applications. The present manuscript gives a detailed explanation of the fabrication, functionalization and characterization of OECTs based on PEDOT:PSS. To be able to intercept this sensor element with traditional biomedical recording systems, the OECT is implemented into simple circuit layouts such as a voltage amplifier or a Wheatstone bridge. These sensor circuits are then applied to real-life biomedical challenges, such as electrocardiographic recordings or metabolite detection in tumor cell cultures, to demonstrate their applicability as well as their limitations.

École Nationale Supérieure des Mines de Saint-Étienne

NNTº: 2017LYSEM007

Marcel Braendlein

Fabrication Lithographique, Caractérisation Électrique et Preuve de Concept des Circuits de Capteurs Comprenant des Transistors Organiques Électrochimiques, à des Fins Diagnostiques In Vitro et In Vivo

Speciality: Microélectronique

Keywords: Bioélectronique, Transistor Organique Électrochimique, PEDOT:PSS

Résumé:

Grâce à leurs excellentes propriétés mécaniques, électriques et chimiques, les dispositifs organiques électroniques à base de polymères conducteurs peuvent résoudre l'incompatibilité entre les modules électroniques rigides en silicone et les exigences des tissus mous qui constituent l'environnement biologique. Les avancées en matière de semiconducteurs organiques et en microélectronique ont donné naissance à la bioélectronique. Cette discipline emploie des capteurs à des fins diagnostiques, telles que la détection des métabolites ou la mesure d'un potentiel d'action neuronal, et des actionneurs à des fins thérapeutiques, comme l'application locale d'un traitement à l'intérieur même du corps, ou la stimulation cérébrale profonde afin de guérir un trouble neurologique. En bioélectronique, l'utilisation de matériaux organiques, tels que le polymère conducteur poly(3,4-éthylènedioxythiophène) polystyrène sulfonate de sodium (PEDOT:PSS) a permis de développer des composants électroniques biomédicaux de qualité exceptionnelle, comme par exemple le transistor organique électrochimique (OECT), qui ont été testés *in vitro* et *in vivo*. Ce manuscrit explique en détail la fabrication, la fonctionnalisation et la caractérisation du OECT à base de PEDOT:PSS. Afin de pouvoir intégrer ce capteur à des systèmes de mesure biomédicaux déjà établis, l'OECT est intégré à des circuits simples, tels qu'un amplificateur de tension ou un pont de Wheatstone. Ces circuits sont mis à l'épreuve de la pratique clinique, dans le cas de mesures électrocardiographiques, ou de détection de métabolites dans des cellules cancéreuses. Cela permet d'apprécier à la fois leur applicabilité, et leurs limites.